Active tool vibration control and tool condition monitoring using a self-sensing actuator

by

Burkhard Heinrich Freyer

Submitted in partial fulfilment of the requirements for the degree

PhD (Mechanical Engineering)

in the

Faculty of Engineering, Built Environment

and Information Technology

UNIVERSITY OF PRETORIA

March 2016

Active Tool Vibration Control and Tool Condition Monitoring using a Self-Sensing Actuator

Supervisor: Prof N.J. Theron
Co-supervisor: Prof. P.S. Heyns

Abstract

The studies consist of two simulations of active tool vibration control and tool condition monitoring respectively and a hardware-in-the-loop laboratory demonstration of active tool vibration control typical to turning.

Besides reducing the restricting effects of tool vibrations on productivity, work-piece surface finish and tool life, it is desirable to handle lack of space at the tool tip and the cost of control systems in turning processes in an effective way. These two aspects are here considered by means of the concept of a self-sensing actuator (SSA) in the simulation of tool vibration control. In the simulation an IIR-filter represents the structure of the passive tool holder. A known pre-filtering technique was applied to the error in a feedback filtered-x LMS algorithm to maintain the stability of the control system. The self-sensing path is modelled and illustrated. The IIR-filters and their inverses were used for modelling this path, with equations resulting from the nodal displacements associated with nodes that have forces acting on them. For the cantilever type structure a considerable reduction of 93% of the displacement r.m.s. values of the tool tip, was obtained when using this control system.

Signal processing using orthogonal cutting force components for tool condition monitoring (TCM) has established itself in literature. Single axis strain sensors however limit TCM to linear combination of cutting force components. This situation may arise when a single axis piezoelectric actuator is simultaneously used as an actuator and a sensor, e.g. its vibration control feedback signal exploited for monitoring purposes. Processing of a linear combination of cutting force components to the reference case of processing orthogonal components is compared. The same time-delay neural network structure has been applied in each case. Reconstruction of the dynamic force acting at the tool tip in a turning process is described. By simulation this dynamic force signal was applied to a model of the tool holder equipped with a SSA. Using a wavelet packet analysis, wear-sensitive features were extracted. The probability of a difference less than 5 percentage points between the flank wear estimation errors of abovementioned two processing strategies is at least 95 %.

This study proves the basic concept of adaptive feedback active vibration control in combination with a self-sensing actuator to control tool vibrations. The structure involved is representative of a tool post clamped tool holder. The advantages that adaptive control hold when applied to non-stationary vibrations motivate this investigation. Secondly the dual functionality of a piezoelectric element is utilized for system simplification. Actuator linearization measures are considered and a model for the system's forward path identified. The tool vibrations signal for this work is of 100 Hz bandwidth around the representative tool holder bending mode. A downscaled force based on real cutting force characteristics was artificially applied to the representative tool holder. Limited form locking contact with the tool holder restricted the actuator's reaction to compressive forces only. Results of up to 70% attenuation of vibration induced strain on the SSA were achieved. This method clearly shows concept viability.

Keywords

Tool vibration, active control, self-sensing actuator, turning process, tool wear-monitoring, structure dynamic modelling, neural network, wavelet packet analysis, adaptive feedback active noise control, linearization.

Für meine Eltern,

Eckhart Freyer

und in Gedenken an Susanna Waldtraut Freyer (geb. Kirchner)

Acknowledgements

The major financial support for these studies I received from my father whom I wish to thank especially for his continued trust.

Especially also I thank my godchildren, Christian Kirschstein and Emilé Kirchner-Stübel, for bearing with me during these studies.

The encounter with Veronicah Mosweu was short. However her thoughtful gestures of loyalty strengthened my hope for a long stretch.

I also want to acknowledge the caring and encouraging support I received from Dr. Janine Franklin, Sister Rykie Venter, Dr. Anton Celliers from Student Health and Dr. Beatrix du Toit and Mrs Ria Paul from Student Affairs. Also from Student Affairs were Chantelle von Mollendorf, Evelyn Nagel and Hanlé Kirkcaldy who often helped me look along workable perspectives.

The birthday wishes from the Vice Chancellor of UP, Prof Cheryl de la Rey, in 2015, I experienced as encouraging and thank her for the thought and also thank the former Dean of the Faculty of Engineering, Built Environment and IT, Prof. Roelf Sandenbergh for his interest in this work.

I wish to thank my supervisor, Prof. Nico Theron, for valuable insights shared and co-supervisor, Prof. Stephan Heyns, for helpful suggestions, the allocation of research funds and for the time both of them dedicated to this project.

I like to express my gratitude towards the National Research Foundation for the financial support under GUN 2053282.

In the laboratory I received assistance from Herman Booysen, George Breitenbach, Phuti Matsaola, Jacob Madileng and Jimmy Mokhafela, which I want to gratefully acknowledge as I do the hints of Danie Drent in Solid Edge. Here I also want to mention Dr. Jan Eksteen for having made his Internet payment facility available.

At the administration I would like to thank Mrs Marietjie Calder, Ms Stefanie Steenberg, Mrs Tersia Evans, Ms Ntsindy Mnyamana and Mrs Elsabe Pieterse for their assistance.

Dr. Lutz Pickelmann from Piezomechanik GmbH, Dipl.-Ing Karl-Heinz Bayerle, Prof. Tshilitsi Marwala, Prof Sukhomay Pal, I like to thank for having given important advice on piezo actuators, piezo drive amplifiers, neural networks and use of wavelets respectively. Dr Philip Loveday , Mr Heinrich Penzhorn and Dr. Rudolf Bester I thank for sharing from their experience and also Ed Kuzemchak and Tom Hendrick both from Texas Instruments for DSP specific advice. Furthermore I thank Mr Terry Nichols from Multitrade Distributors for sharing from his knowledge on tool inserts.

I wish to mention Lucy de Souza from Nedbank Campus representation for her firm words of encouragement and thank her for these.

With respect to MSC Nastran/Patran I am grateful for help I received from Mr Flip de Wet, Dr. Craig Long, Mr Alewyn Grové, Paul van Niekerk and Dr. Abrie Oberholster, who assisted me also with the eDAQ instrumentation.

The former fellow students Soon Hwang, Francois van Tonder, Patrick Sambayi and Peter Schön I thank for their inputs towards the use of some of the instrumentation and Daniel Hugo for signal integration code.

From the workshop I'd like to thank Mr Jan Brand, Neels Smit (senior), Neels Smit (junior) for assistance given.

The Departments Electrical, Electronic and Computer Engineering, Mineral and Material Sciences, Chemical Engineering, Civil Engineering and Microscopy helped me with equipment which I am grateful for.

I am equally grateful towards Mr Trevor Leong from World Test Systems S.A. and Mr Rodney Farrow from Texas Instruments S.A. and the Texas Instruments University Programme respectively for borrowing and donating equipment and software to this project.

Sometimes repeated and short but helpful encounters I had with the following persons from the Department Electrical, Electronic and Computer Engineering: Hans Grobler, Gerhard Ebersohn, Prof. Michael Gitau, Helmut Schütte, Jacques van Wyk, David Buys, Henry O'Kennedy, Victor Fisha, Marie Pretorius and Louis Wabeke. I thank the above-mentioned and also their department for their assistance.

From the Academic Information Centre it was Mrs Annemarie Bezuidenhout, Mrs Elna Randall, Mrs Sunette Steynberg, Mrs Marie Theron, Mrs Rachel Mashlangu, Mrs Hannetjie Boshoff, Mrs Josephine Modiba, Cora Bezuidenhout, Zani Swart, Fana Mgidi and Francina Laka all of whom I wish to thank for their valuable assistance.

From IT-help I appreciated the assistance of Stefan and Nadia Stolz, Juan Roos, Johan Kotze, Sonny Matsitse, Linda Lötter and Hildegard Jacobs.

I wish to thank members in the Lynnwood and Central Baptist Churches, for fellowship and encouragement. I furthermore like to thank the late Mr Friedrich Hoberg, the late André Vlok, my sister Almut Kirschstein, Arden Meyer and Pastor Martin and Heike Stobwasser from Stadtmission Pretoria for their prayers. I thank the Gonçalves family for thinking of me with their e-mailed letters, which they sent regularly from Lubango.

I gladly like to thank my siblings and in-law siblings for their support often without me knowing amongst others with financial transfers, passport renewals and car license discs.

I also wish to thank the late Mrs Anny Köck (former landlady) the late Alfred Newman and Ruth Newman, the late Andreas and Hanna Herrmann, the late Lienhard Rüsch and Gisela Rüsch, Mrs Rina Lombard (former landlady), the von La Chevallerie family, the Johannsmeier family and the Winsauer family (former landlords) for their hospitality.

From my last neighbourhood during the studies, the interest in them and encouragement by Dipl.-Ing Eberhard and Resi Grammel, Astrid Sieburg and Dr. Xian Ming Ye is appreciated such as the edifying talks with Michelle are.

CONTENTS

CHAPTER 1

INTRODUCTION

Firstly a background provides an understanding of the technology utilized in this work and also the problem of tool vibrations that it is used for. The following section gives an outline of the fields in which the applications of the piezoelectric transducer can be found, one of them being the control of tool vibration. How tool vibrations are caused is briefly explained in a description of their causal mechanisms. It becomes clear that tool vibrations cannot be avoided however controlled or utilized in tool condition monitoring (TCM). This in turn leads to a brief description of the application field of tool vibration control and tool vibration monitoring.

In support of the motivation of this work the benefits to the particular machining process under consideration are mentioned. In pursuit of aims critical to this work contributions were made to research in the manufacturing field which are then contained in a separate section.

1.1. BACKGROUND

1.1.1 The piezo effect

Piezoelectric transducers have the property of either polarizing in the same direction as the applied force or perpendicular to it. In the same way but reciprocal they provide strain and thus stroke either in the same direction of the polarization due to an applied voltage or perpendicular to it (Heimann , Gerth & Popp, 2001:52; Roddeck, 2003:11). This is the piezo effect, which is called the longitudinal effect when force or strain is in the same direction and the transversal effect when directions are perpendicular respectively.

Both functions are investigated in this work to determine its viability in active tool vibration control and tool condition monitoring. Both, control and monitoring in that case happen via a self-sensing actuator (SSA), as a transducer, made of piezoceramic material. Firstly however, some general

applications of piezoelectric transducers as well as particular examples of indirect and direct measuring techniques utilizing piezoelectric material are given (Uchino, 1997:1-12;157-172).

1.1.2 Applications of piezoelectric transducers

The fields of optics and astronomy employ piezoelectric transducers for positioning purposes and vibration control respectively. In the case of optical systems the use is to make the latter adaptive to the application, while in the case of astronomy the underlying reason for use is to cut out or limit the effect of disturbances that come from the shuttle that carries them. Another application field is in fluid control, e.g. to produce ink drops, change valve positions or for adjustable flow guiding vanes. In the millimetre size range piezoelectric material lends itself to piezoelectric ultrasonic motors with sufficient energy efficiency. Electromagnetic motors in contrast become less efficient with decreasing size.

Some examples of indirect measuring techniques of piezoelectric transducers include electrical, optical, x-ray and ultrasonic techniques. Often this indirect function comes down to positioning or utilizing the piezo-effect.

In electrical techniques such as strain gauge measurement resistance change is due not only to size change of the wires but also to the piezo resistive effect (Uchino, 1997:157; Roddeck, 2003:169). This effect is less notable in metal gauges however pronounced and therefore utilized in gauges of semiconductor material. Another application is in a high accuracy capacitance bridge of a dilatometer where a piezo actuator has the function to cancel changes to the capacitor gap caused by low-frequency drift.

An X-ray method can measure lattice parameter changes in crystalline material due to piezoelectric strain (Uchino, 1997:164). This method proved to be unpractical for displacement sensors, however has scientific value.

Small special (inter-digital) electrodes on the face of a piezo ceramic cylinder which is mounted on a shaft produce a standing ultrasonic wave around the cylinder (Uchino, 1997:164). The resulting periodic stress concentration at the nodal points on the piezo electric material induces corresponding piezoelectric charges. These are measurable with charge probes and provide an indication of the angle of rotation.

An example of a direct measuring technique is the use of piezoelectric material in accelerometers. These contain a seismic mass attached to one face of a piezoelectric stack element. A voltage is

induced due to the pressure during acceleration. This effect of voltage as a result of pressure and resulting strain of the piezo electric body is also exploited in force transducers described in Heimann et al. (2001:87). Piezoelectric material can therefore also be used for strain sensing and have a signal-to-noise ratio superior to that of strain gauges (Moheimani, 2006:22).

Besides abovementioned general applications and measuring techniques piezoelectric transducers also find their use in active structures. This is the case when lack of stiffness is addressed by means of piezoelectric actuators in order to obtain protection against excessive vibrations (Roddeck, 2003:18; Isermann, 1996).

Precision machining utilize piezoelectric actuators e.g. for vibration control (Pan & Su, 2001; Andrén, Håkansson, & Claesson, 2003; Xu & Han, 1999; Fawcett, 1990). The piezoelectric transducer also has a micro-displacement sensitivity and can therefore be used for position sensing (Uchino, 1997:157). Both these functions are exploited in this study. With application to the field of turning it investigates how the actuator function can be used for vibration control. Simultaneously it exploits the sensor function for two purposes. The first is to let the sensed strain serve as a feedback signal in closed loop control and secondly to utilize for acquisition of strain data, e.g. to monitor tool wear.

1.1.3 Tool vibrations

Due to the application field of piezoelectric transducers in this study a brief background pertaining to the nature of tool vibrations and causal mechanisms is given.

An investigation into the nature of tool vibrations, i.e. regarding their properties, was performed by Sturesson, Håkansson, & Claesson (1997) and Andrén, Håkansson, Brandt & Claesson (2004a,b) respectively for external and internal turning, i.e. boring, processes. They found that tool vibrations are non-stationary in each case. To be more specific findings of Sturesson et al. (1997) were that external turning is a weakly stationary process which is known to be a special case of non-stationarity (Meirovitch, 2001:688). For external turning spectral densities of vibrations tangential to the work piece and also the coherence function between these and vibrations in the feed direction are given (Sturesson et al., 1997). From resulting graphs and modal participation factors in both directions it is concluded that vibration power depends not only on the cutting data, the structural properties of the machine tool system and also the work piece material. Along with Marui, Ema & Kato (1983) the deflection considered to be the main one in this work for tool holder with classic shank is in the tangential force direction. Similarly, the finding made for internal turning (Andrén et al., 2004b), was that the main vibration energy is in the cutting speed direction. Andrén et al. (2004a) and Sturesson et

al. (1997) both showed by measurement that tangential or cutting speed directed and feed tool vibrations are not always Gaussian distributed. For this finding they gave as possible reason the physical limitation of motion in feed and tangential or cutting speed direction.

About two decades ago two main causes for machine tool vibrations have been pointed out. These were mode coupling shown by Bukkapatnam & Fofana (2001) and regenerative effects, which Lee, Nian, & Tarng (2001) reported on. Mode coupling happens when the tool motion is in directions associated to different degrees of freedom at the same time. Tlusty & Ismail (1981) demonstrated mode coupling self-excitation in their analysis of the non-linearity in turning. In mode coupling vibration each direction has amplitude and phase differing from that of the other direction. This is also shown by Gasparetto (1998), who did a short system theory analysis on the mode coupling phenomenon. It illustrates the variation of work done by cutting tool between two extreme position points of its motion indicating an exchange of energy across system boundaries. In addition variations in uncut chip thickness cause cutting force variations resulting in tool vibration leaving an uneven surface and allowing cause and effect to repeat itself from cut to cut. This kind of vibration is therefore described as regenerative.

Chen, Ulsoy & Koren (1993) and Rahman & Ito (1985) in earlier publications show how delayed feedback of the cut surface affects the cutting process and regenerate cutting force variations by means of block diagrams. Both have in common that they make use of linear time invariant (LTI) modelling to perform a stability analysis with focus on simplicity and lathe specific aspects respectively.

As seen from above literature LTI modelling is thus suited to describe mode coupling and regenerative chatter but Bukkapatnam et al. (2001) and Deshpande & Fofana (2001) extend their description of these phenomena and move closer to reality by performing a non-linear modelling assisted by chaos theory of the dynamics of the process and the structure involved to also other effects besides the abovementioned two, such as ploughing and tool wear to be included.

Likewise the research of Jemielniak & Widota (1989) and Lai (1987) can be placed into the category of a non-linear approach to chatter vibration modelling via algorithm programming.

In the studies of Doi & Kato (1956) and Marui et al. (1983) the mechanism underlying to regenerative chatter was investigated and explained and clearly show the lag between the horizontal work piece displacement and the vertical cutting force. The work of Kaneko, Sato, Tani & O-hori (1984) confirm this mechanism.

Authors such as Fabris & D'Souza (1974) also point to the fact that a lag exists between cutting force variations and chip thickness variations. These authors refer to this phenomenon and bring up the term,

hysteresis. The conclusion of this is that the relationship cannot be described with a linear but rather a non-linear hysteresis model. Non-linear modelling is therefore more appropriate to describe the variety of effects and relationships present in a cutting process, as Bukkapatnam et al. (2001) pointed out in their work.

1.1.4 Tool vibration control and tool wear monitoring

Tool vibrations in turn affect tool wear adversely and detail on this consequence can be found in Chiou & Liang (1999), Murata & Kokubo (1994). Therefore some background is given on approaches described in the literature to deal with tool vibrations, either to control them or to use them for tool wear monitoring purposes.

Pan et al. (2001) make use of a robust adaptive controller and models the process as being uncertain and linear. They do address chatter as a result of the aforementioned hysteresis relationship between the cutting force and chip thickness.

Pratt & Nayfeh (1999) adopts structural as well as cutting force non-linearities in their initially linear model. They then present a second order linear feedback compensator to address the chatter phenomenon directly through active control.

From a non-linear model based on chaos theory Bukkapatnam, Lakhtakia & Kumara (1995) develop Mandelbrot sets to train a neural network with a closed control loop. These are sets that describe the state trajectories for different vectors of control parameters such as feed rate and depth of cut. According to the monitored states of the dynamic system, the control parameters are then selected by a neural network which is trained for optimal control. The objectives are to achieve a minimum reduction in material removal rate and a minimum transition time from the undesired to a desired stable state.

Tool vibration control with the focus on non-linear modelling is mentioned above to point to real rather than simplified characteristics of machine tool dynamics. Such non-linear approaches to machine tool dynamics can be followed if the research emphasis is on understanding its characteristics and relationship to cutting parameters. Lai (1987) grouped researchers into those that investigate physical phenomena of chatter and those interested in simply the active control of it.

An active control approach is taken by Andrén et al. (2003) who have implemented a feedback version of the filtered-x LMS adaptive control for its simplicity.

For the same reason this research employs the filtered-x LMS adaptive control however in such a way as to accommodate a self-sensing actuator and investigate its viability in tool condition monitoring (TCM). This study is therefore placed in the category of active control inclusive of a TCM function. This was done with a long term objective of simultaneous active tool vibration control and tool condition monitoring.

Tool vibration is to be reduced by means of active control to avoid increased work piece surface roughness and tool wear but can provide information on tool condition too. Bonifacio & Diniz (1994) and Abouletta & Mádl (2001) reported on the correlation of tool vibration and surface finish which can also indicate the end of tool life according to Bonifacio et al. (1994).

Tool condition monitoring (TCM) can be sophisticated such as with the use of neural networks which is the interest of Liu & Altintas (1998), Sick (2002) and Choudhury & Bartarya (2003) and allows to indicating tool condition during the cutting process. More than a decade ago Sick (2002) gave deeper insight on the situation regarding the research into the use of neural networks for tool wear monitoring while Cho, Lee & Chu (1999) gave a general view on the state of machining process monitoring with respect to sensors and decision-making algorithms in Korea. Both these researchers indicate a gap between academic research and practicality in the years up to their publication. Neural networks in the research here provide the same signal processing method while making a quantified comparison between two sensing methods one of which being the case of using an SSA as sensor.

Non-neural network indication of tool wear is also possible as Bahre, Rosenberger & Warnecke (1992), Bonifacio et al. (1994) and Li, Wong, & Nee (1997) have shown, by respectively monitoring signal features, simply the root-mean-square value or from the horizontal/vertical acceleration based coherence function from an accelerometer instrumented tool holder.

The choice of a simple control algorithm which leaves aside causes of vibration but deals with it simply as a disturbance allows firstly a broad treatment of the problem and secondly to explore the particular application of the SSA.

1.2. THESIS MOTIVATION

i. The need for the use of an SSA originates from the existence of the dual need to control tool vibrations and the need to monitor tool condition. This need can be met with a device of dual functionality. This means that actuator and sensor, both necessary elements of feedback control, are combined in a single transducer. The particular way which is looked at in this

study is by means of a single transducer, viz. a piezoelectric stack actuator. By limiting TCM and tool vibration control to a single device two important tasks can be accomplished. Information regarding such a self-sensing actuator is readily available from research done by Dosch & Inman (1992) and Anderson & Hagood (1994) in a laboratory environment. An investigation is therefore conducted into necessary aspects of active tool vibration control and TCM using a SSA.

ii. Regarding the part of the control of tool vibrations it is argued with Pratt et al. (1999) to adopt a direct approach to handle the stability problem of the cutting process. Modification of the structural properties by means of passive control or adding structural reinforcement would be cumbersome to adjust if cutting or tool parameters are changed. Active controllers, used in this work, can be coded and embedded on a digital signal processor and allow for convenient adjustments in contrast to analogue controller. An adaptive control scheme was selected for its ability to limit non-stationary vibrations. Literature supports adaptive control in turning processes (Pan et al., 2001; Andrén et al., 2003). An improved surface finish is a direct benefit flowing directly out of vibration control as it is clear from Abouletta et al. (2001), Bonifacio et al. (1994) that surface roughness correlates with severity of tool vibrations.

iii. The benefits regarding the part of TCM result in improved productivity and extended utilization of tool inserts if this concept is implemented in real turning processes. Further advantages are improved work piece surface finish, also thoroughly referenced to by Landers & Ulsoy (1996), as well as reduced waste of tool inserts with more reliable online knowledge of the end of tool life, also referred to in Dimla Snr. (2000) and Silva, Reuben, Baker & Wilcox (1998). Improved utilization of tool inserts will thus result in less premature cutting process interruptions and therefore fewer interruptions in total.

iv. With a collocated actuator-sensor-system such as the SSA type it is known Preumont (2002:75) that stability between input and output is guaranteed, if the actuator dynamics are neglected.

v. The emphasis of the thesis is to pave the way toward further research of detail aspects of the SSA concept in so far that a basic set-up was developed. Structural investigations into favourable positioning of the piezoelectric elements into the real tool holder fall outside the scope of this research. In a similar way specialized attention to circuit layout to meet specific requirements with respect to noise levels is excluded from the scope of this work.

vi. Since this work was towards a complete system the result is towards a prototype which could be taken to market with little additional research and development effort.

1.3. AIMS AND CONTRIBUTIONS

As a basis for the long term objective of simultaneous active tool vibration control and TCM more laboratory work had to be done and aims set to determine the viability of the SSA concept for such an objective. Therefore this section presents the following aims and contributions made in this study.

i. The selection of a functional adaptive control algorithm was seen as one of the aims.

   a. The use of a filtered-u adaptive infinite impulse response (IIR) filter (Elliott, 2001:163) as a potential configuration for vibration control in simulation was considered, due to fewer filter coefficients required. This consideration was also made since these filters can have self-stabilizing properties in spite of their poles being prone to migrate outside the discrete z-domain unit-circle. However, stability was not obtained.

   b. The simulation of tool vibration control and its problem approach to determine the effect of typical tool vibration control via a SSA using a filtered-x LMS algorithm can be seen as a contribution towards problem understanding.

ii. A contribution towards TCM is an investigation of the viability of TCM using a unidirectional strain signal typical for SSA based systems.

iii. A further contribution is the combination of the SSA with an active control system as proof of concept typical for turning process conditions in a hardware-in-the-loop (HIL) experimental setup.

iv. A new application of the SSA concept and an extended functionality was investigated as contribution to the field of manufacturing. It was aimed to demonstrate that the SSA based control could be applied to structures in particular tool holders in typical turning processes. The principle of collocated control using an SSA will also be relevant to the field of structural vibrations in general.

v. The final contribution is the result that a test of the complete control system with the SSA concept produced, which suggest its viability.

   a. In this research a prototype system is developed. The minimum outcome was to investigate the potential that lies in this system to be developed further into a product and register a clear reduction in the root-mean-square value of tool vibrations.

b. Associated with the system tested is the evidence that the units in the system's forward and feedback paths can simultaneously bring forth the result of attenuated typical tool vibrations and information on tool condition.

1.4. ORGANIZATION

The further organization of this work covers 3 main chapters and a chapter of conclusions of the work followed by appendices.

In the second chapter a linear simulation is done on a desk top of active tool vibration control using a self-sensing actuator. Discrete z-domain transfer functions between nodes of the passive structure were used for this purpose. These originated from a finite element model of an industrially speaking common tool holder and properties of an existing type of piezoelectric actuator. In this simulation the signal representing the cutting force were data acquired from a turning process with a manually operated lathe.

The next chapter compares two neural network based tool condition monitoring (TCM) processes quantitatively. The two TCM processes differ from one another concerning their respective sensing method. Unidirectional cutting forces that would be sensed by an existing piezoelectric SSA are compared to orthogonal signals as sensed by a strain gauge instrumented tool holder. These methods then differ from one another with respect to tool wear sensitive feature selection as a result of their difference in sensing.

The fourth chapter is a realization of the simulation of the second chapter. This part of the work consists of a setup to demonstrate the concept of a self-sensing actuator in active control of typical tool vibrations. Instead of building the system to be controlled from separate transfer functions as in chapter 2, a single-input-single-output (SISO) model constituted the forward path. This path includes all modules between the DSP and a strain proportional signal from the sensing circuit. This chapter uncovers areas of the work that need further attention before a final implementation on a lathe.

The thesis ends with a conclusion of the studies and points out several aspects that constitute topics for projects towards research and development of a tool holder for active tool vibration control and simultaneous TCM.

CHAPTER 2

SIMULATION OF TOOL VIBRATION CONTROL IN TURNING, USING A SELF-SENSING ACTUATOR

2.1. INTRODUCTION

The first step of the investigation into the viability of using a self-sensing actuator for tool vibration control is the simulation of it. It consists of the formulation of the structural dynamic problem and using it as a plant model in the simulation of active tool vibration control. The main contents of this chapter consist of the paper by Freyer, Theron & Heyns (2008).

In machining, and particularly in turning processes, tool vibration is a problem which commonly has to be dealt with, mainly because of its constraining effect on productivity, work-piece surface finish and tool life. Tool vibration constrains productivity since the selection of cutting parameters is restricted to values lying in a region in which they guarantee a stable but not the most productive operation (Yeh & Lai, 1995). Tool vibration affects the surface finish of work-pieces during cutting owing to the relative motion of the tool and the work-piece (Cheung & Lee, 2000). Compression and friction during chatter are additional sources of energy dissipation, which promote flank wear on the cutting tool and reduce tool life (Chiou & Liang, 2000).

Control over tool vibration can be approached by using passive methods in which either structural stiffness is added to the lathe or a tuned vibration absorber is applied to the process (Tarng, Kao, & Lee, 2000). However, active control has become a favoured method since significant advances have been made in the development of micro-positioning actuators over the past decades. These developments allowed a choice between semi-active and fully active vibration absorbers. Semi-active means that the control force is located between the primary and absorber structure, whereas active means that the control force is applied more directly, between ground and the primary structure directly (Pratt & Nayfeh, 1997). Examples of active tool vibration control are represented by the work done by Andrén et al. (2003) and Pan et al. (2001). They respectively used adaptive filter and adaptive control methods to handle process uncertainties. In the control of tool vibrations, the problems other than process uncertainties are the lack of space around the tool tip and the

additional cost of a sensor to pick up the tool displacements. This chapter shows through simulation that these two problems can be solved when a self-sensing actuator is employed in the control system. Piezoceramics can be used in this fashion, because it is possible to exploit the piezoelectric and reciprocal effect simultaneously. Besides the piezoelectric effect of piezoceramics, i.e. the generation of a voltage if a force load is applied to such a material, it also exhibits a reciprocal effect which consists of undergoing a change in length when a voltage is applied across its electrodes. This means that the piezo actuator can simultaneously function as a sensor, i.e. as a self-sensing actuator (SSA). The possibility of functioning as an SSA has already been investigated by Dosch et al. (1992) and was then covered in further detail by Anderson et al. (1994). In turning processes, this principle can be used as a self-sensing actuator in a closed-loop tool vibration control system. Therefore, by using an SSA instead of a separate actuator and sensor, the above-mentioned problems can be overcome.

This chapter addresses critical issues in the simulation of tool vibration control in turning processes, using a self-sensing actuator. It answers the main question of how the displacement of the tool tip, as a result of both the cutting force and the actuator force can be measured when the SSA is placed at an offset from the tool tip. In this case, one could anticipate that models representing the force displacement relationships between the tool tip and the actuator and vice versa, would play a significant role in the simulation. The work in this chapter therefore shows how the actuator structure of the passive tool holder as well as the sensing path of the SSA may be modelled to incorporate not validated but realistic model parameters. It furthermore describes how these models, in the form of IIR-filters, can be incorporated into the feedback-filtered-x LMS adaptive algorithm. The stability problems associated with the IIR-filter are dealt with by using the principle of pre-filtering the error signal with the poles of the passive tool-holder structure (Vipperman, Burdisso & Fuller, 1993). Another critical question that is addressed here is what signal should be used to represent the cutting force during the simulation. Pertaining to this question this chapter gives details of how a representative cutting-force signal is obtained from a practical turning process and then processed for use in the simulation of tool vibration control. The results of a simulation of the control system give an indication of to what extent the attenuation of tool vibration is possible.

2.2. SELF-SENSING ACTUATOR (SSA) IN TURNING

2.2.1 Requirements to consider

Three equally important aspects need attention for the simulation of tool vibration control. They are firstly the question of a representative cutting-force signal, secondly the decision about a suitable actuator and thirdly the requirement of an effective control method.

As this part of the work deals with the simulation stage of vibration control, a signal was needed which could represent a typical cutting force in the turning process. To meet this need, the cutting force of a practical turning process was measured and the signal stored. This signal constitutes the source of vibration during simulation.

The decision about which actuator would comply with the requirements of the application under consideration was mainly based on the criterion that it should be self-sensing. The reasons for this criterion are the lack of mounting space at the tool tip and the additional cost of an otherwise separate sensor. Another requirement emanated from the nature of the turning process, which requires actuators that can control the vibration from high cutting forces at a high frequency. All these requirements for an actuator could be met by a piezoelectric type of actuator, which would satisfy the main need of serving simultaneously as an actuator and a sensor. The first purpose of the sensor is to pick up the resultant displacement of the tool tip, which can be used as feedback in a closed-loop control system. As the self-sensing actuator is a collocated sensor-actuator pair situated at an offset from the tool tip (Figure 2.1), it will not be able to capture the true displacement of the tool tip. It will only sense a voltage, which is also influenced by the dynamics of the passive tool-holder structure. Therefore linear parametric models of the passive tool-holder structure will be involved in the simulation of the control system. The position for the actuator at an offset from the tool tip requires the structural modes participating in the direction of the cutting force to be included in these models. Their digital representations should therefore be in the form of IIR-filters. These models are the elements of a dynamic flexibility matrix, which relates forces at two points of interest to their respective displacements. The two mentioned points of interest are the tool tip and the connecting point of the actuator and tool-holder. These are the points where internal and external forces respectively act in and on to the passive structure. The need for linear parametric models can be satisfied numerically by generating a finite element (FE) model of the passive tool-holder structure in MSC-Patran and running a modal analysis in MSC-Nastran.

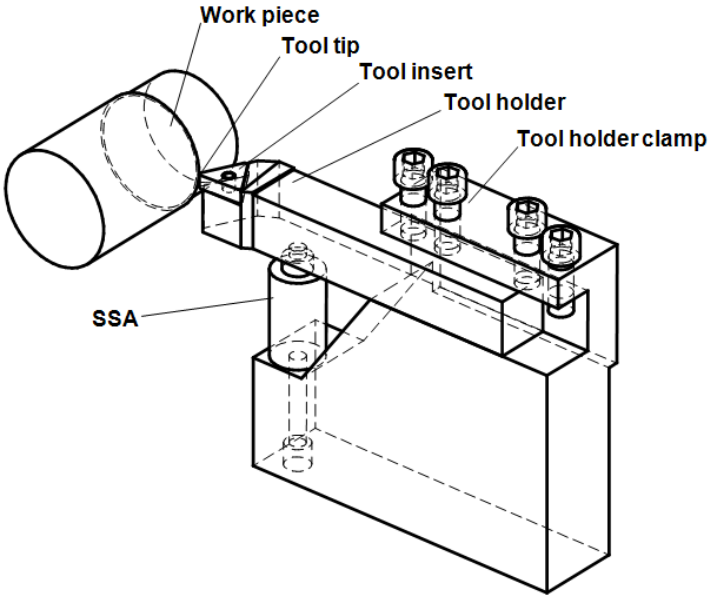

Figure 2.1: Tool-holder clamp with tool holder, SSA and work piece.

The third of the above-mentioned aspects is the requirement for an active control method. It is most important that such a method should have the property of being adaptive, owing to the random and non-stationary nature of a turning process. A control algorithm often recommended in the literature on active vibration control because of its simplicity, is the filtered-x LMS (Fuller et al., 1996). Because this algorithm makes use of an adaptive filter it is suited to dealing with the above-mentioned type of tool vibrations induced by the cutting force (Andrén et al., 2003). For the use of this control method, two problems have to be addressed. The first one is directly linked to the choice of the filtered-x LMS control algorithm. The uses of IIR-filters for the models, which form the elements of the dynamic flexibility matrix of the passive structure, introduce stability problems in an adaptive control algorithm such as the chosen LMS-type. This problem will therefore require stabilizing measures in the control system. The second problem, also linked to the LMS-type algorithm, is that a reference signal should be available to the adaptive filter and its algorithm. In the application to tool vibration control, the tool tip displacement, due to the control action and cutting forces should serve as a reference signal, but it cannot be measured. In relation to the first of these two problems, Vipperman et al. (1993) propose a technique, which is mentioned in the previous section and used to avoid the stability problem. It involves the pre-filtering of the error signal, which is the tool tip displacement resulting from both the actuator and the cutting force input into the tool holder. The second problem is overcome by using a feedback version of the filtered-x LMS algorithm as proposed by Kuo & Morgan (1996), so that the need for a reference

signal is met. This is possible because the cutting force measured for simulation purposes is close to being a narrowband disturbance.

2.2.2 Assumptions

This part of the work represents a preliminary investigation for the implementation of self-sensing actuators in turning. Various assumptions were made of which the validity will become clearer during future practical implementation. These assumptions are however believed to be reasonable.

- The cutting process (CP) causes a cutting force at the tool tip and there is no feedback from the controlled tool tip to the CP, i.e. the control system has no influence on the cutting force.
- The tool holder acts like a cantilever, which is supported by the SSA at an offset from the tool tip.
- The structure is lightly damped and a proportional viscous damping model is sufficient.
- In the envisaged implementation stage the sensing circuit will be of a full-bridge type. Here, the bridge is assumed to be balanced, i.e. the branch of the bridge parallel to the branch containing the SSA, contains an impedance component equal to that of the SSA.

2.3. REPRESENTATIVE CUTTING-FORCE VIBRATION SOURCE

Strain gauges mounted on a turning tool holder (Figure 2.2) were connected in bridge circuits also shown in Appendix B and served as transducers to measure the cutting force. The signal data acquired were then post-processed so that they could be used as a typical vibration source in the simulation of the control system.

The cutting was done by using a Mitsubishi TNMG 160408 UTi20T uncoated-carbide tool insert on EN 19 steel with the following cutting parameters:

Depth of cut: 1 mm
Feed: 0.3 mm/rev
Cutting speed: 84 to 124.2 m/min

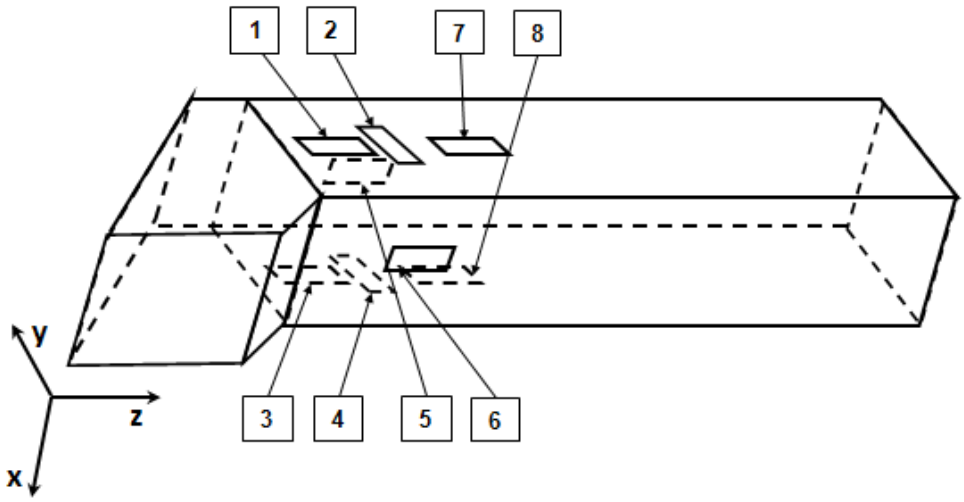

Figure 2.2: Tool holder with strain gauges (SG): SGs 1 to 4 in full-bridge measure the thrust force; SGs 5 and 6 in half-bridge measure the feed force; SGs 7 and 8 in half-bridge measure the cutting force.

The cutting parameters were chosen from a region recommended by the insert manufacturer for that specific insert and work-piece material. However, the parameters were selected as low as possible to avoid being forced by reducing the work-piece diameter to make large changes in the speed on the lathe. The cutting speed was then chosen so that the total time of cutting-force measurement was kept as short as possible and corresponded to an insert life span of 95 minutes of cutting time.

The static cutting force was calibrated on the abovementioned strain gauge instrumented tool holder. The modal mass of the tool holder was, however, taken into account later during the simulation stage. The calibration was performed by measuring voltages v_i while applying three different known forces in the *j*th direction and zero force in the remaining directions. Using the three different force/voltage pairs, each coefficient a_{ij} in the *j*th column of the calibration matrix $\boldsymbol{A}$ was determined three times from the relationship defined as

$$\boldsymbol{v} = \boldsymbol{A}\boldsymbol{f}, \tag{2.1}$$

where the force vector $\boldsymbol{f} = [F_x \quad F_y \quad F_z]^T$ and the average were then taken for each coefficient. The force vector signals, $\boldsymbol{f}_k$, could then be obtained from the measured voltage signals $\boldsymbol{v_k} = [\boldsymbol{v_{1_k}} \quad \boldsymbol{v_{2_k}} \quad \boldsymbol{v_{3_k}}]^T$ with

$$\boldsymbol{f_k} = \boldsymbol{A^{-1}} \boldsymbol{v_k}, \tag{2.2}$$

where the subscript k refers to the signal sequence at time t_k and will henceforth be used as such. The matrix inversion was simply performed in MATLAB (2003b) and the inverted matrix $\boldsymbol{A^{-1}}$ for this chapter is given in (A.2). The execution of (2.2) consisted of a matrix multiplication with the signals vectors $\boldsymbol{v_{i_k}}$. Furthermore, only the force contributions in the direction of the cutting force were used in the simulation.

Post-processing of the calibrated signal was done by removing the drift and noise contribution of the amplifier in the measurement path by filtering the signal with high-pass filter to remove the drift. This is done using an in-house program which transforms the signals to the frequency domain and removes the frequencies below 8 Hz. As a notch (band-stop) filter a linear-phase FIR filter was used to remove the noise of the amplifier. This was done by filtering the signals in the forward direction, and then, after having reversed the filtered signal, running it back through the filter again. In this way zero-phase distortion of the output signals for both abovementioned filter methods could be achieved.

An IIR-filter representing the modal model of the passive tool holder was applied to the cutting force signal that was obtained after calibration. This filtering is done in order to deliver displacement values. The above-mentioned filter and force signal together constitute the vibration source used for the simulation of control of a turning process tool vibration.

In this part of the work, two tool-holder structures are considered. One is the tool holder equipped with strain gauges (as in Figure 2.2) and not supported by an actuator, which is referred to as boundary condition 1 (BC1) tool holder. The tool holder supported by an actuator will be referred to as boundary condition (BC2) tool holder. The BC1 tool holder was used for the measurement of the cutting force. The second tool holder (BC2) is the passive structure used as a model in the simulation of the vibration control system. BC1 tool holder has its modes at frequencies differing from those of BC2 tool holder shown in Figure 2.1, because of different boundary conditions. Moreover, the additional mass of the strain gauges, strain gauge protection and cabling influenced the dynamics of the BC1 tool holder.

Each tool holder only passes those frequency components of the cutting force which are near the frequencies of the tool holder's modes participating in the cutting force direction. Therefore the tool holder acts as a mechanical filter. The measured signal is the one which was passed by BC1 tool holder, which has modes at lower frequencies than the equivalent modes of the BC2 tool-holder model used for simulation purposes. Therefore the measured cutting-force signal had frequency components corresponding to the frequency of the participating mode of BC1 tool holder. These frequency components were shifted to the frequency range of the equivalent mode of BC2 tool-holder model in order to obtain a new, adapted cutting-force signal. Power spectral densities of the cutting force measured by BC1 tool holder and the cutting force with shifted bending mode frequency content are shown in Figure 2.3.

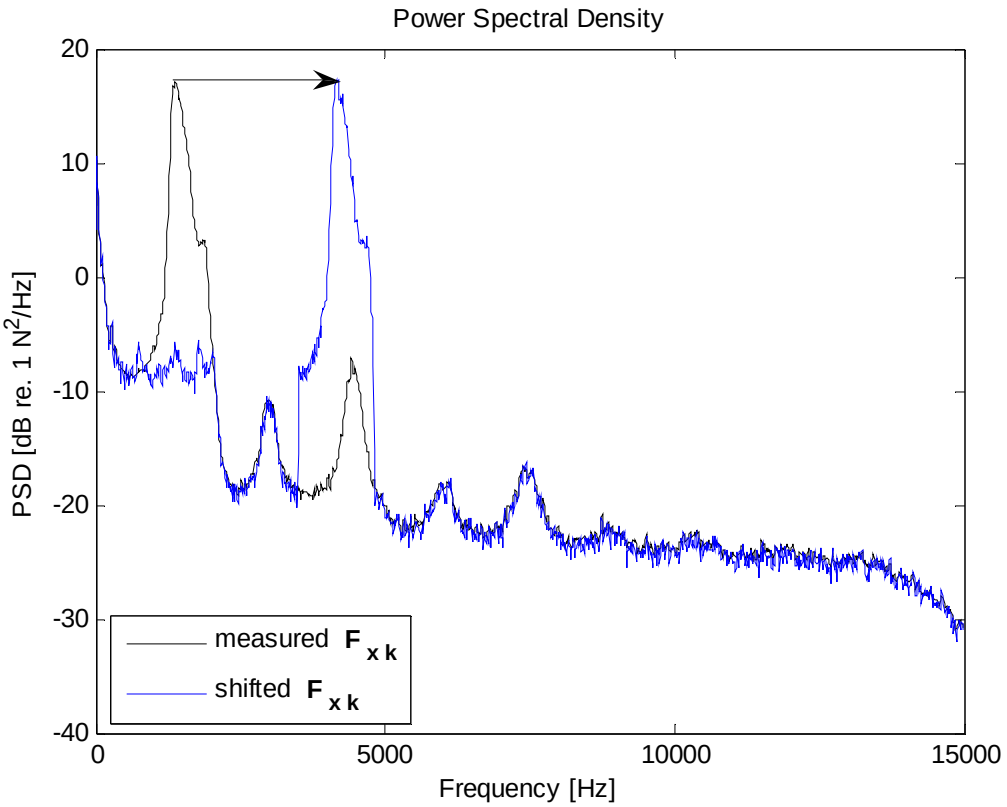

Figure 2.3: Power spectral density of measured and shifted cutting force signal $\boldsymbol{F_{x_k}}$.

For the remainder of this section and section 2.4 it is the convention to use capital letters for Laplace and z-domain variable and lower case symbols for time domain variables.

During the simulation abovementioned adapted cutting-force signal was passed through an IIR-filter representation of $T_{11}(s)$ which is the transfer function between the cutting force, $f_1(t)$,

exerted on the tool tip and the displacement of the tool tip (see Figure 2.1) due to the cutting force. A description how the modes of tool holder with BC2 were incorporated in the transfer function $T_{11}(s)$ is given in section 2.4. The filtering through IIR-filter of $T_{11}(s)$ produced a displacement signal, $d(t)$, which is the displacement contribution of the cutting force to the total displacement of the tool tip. The power spectral density of this signal is shown in Figure 2.4. In this vibration-control approach signal, $d(t)$, is regarded as narrowband; a feedback version of the filtered-x LMS-algorithm could therefore be used for tool-tip vibration control. Figure 2.5 shows that the probability distribution of the signal, $f_1(t)$, is a Gaussian process for the first 367500 samples but indicates a non-linearity during the two passes thereafter. This process non-linearity was observed to occur during different passes on three different lathes. No precise explanation of this phenomenon has as yet been found. It may be due to an interaction between the cutting parameters chosen and radial play on the spindle bearings.

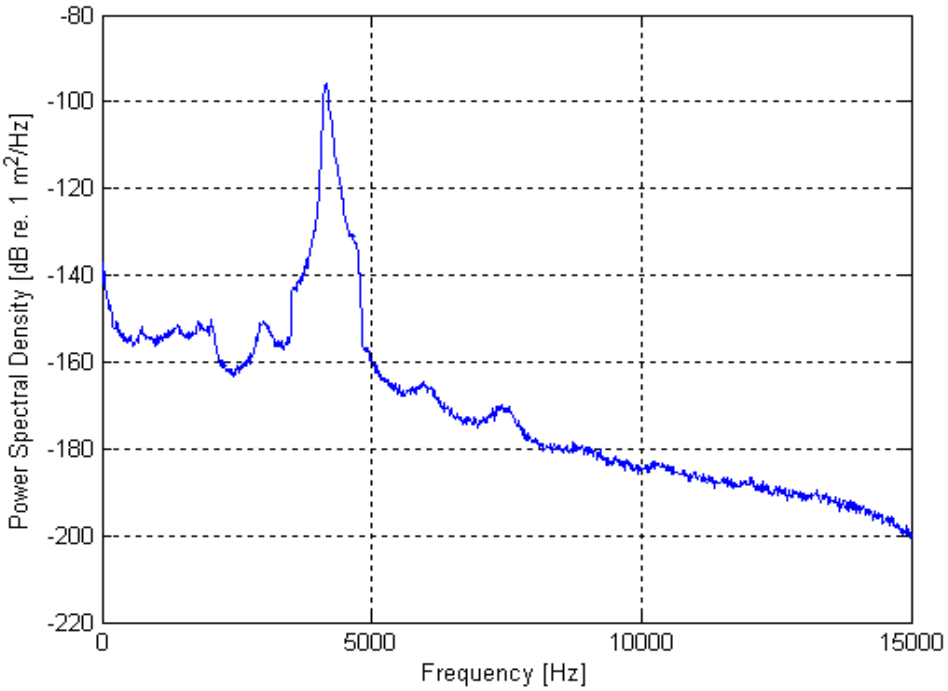

Figure 2.4: Power spectral density of the tool-tip displacement signal due to cutting force.

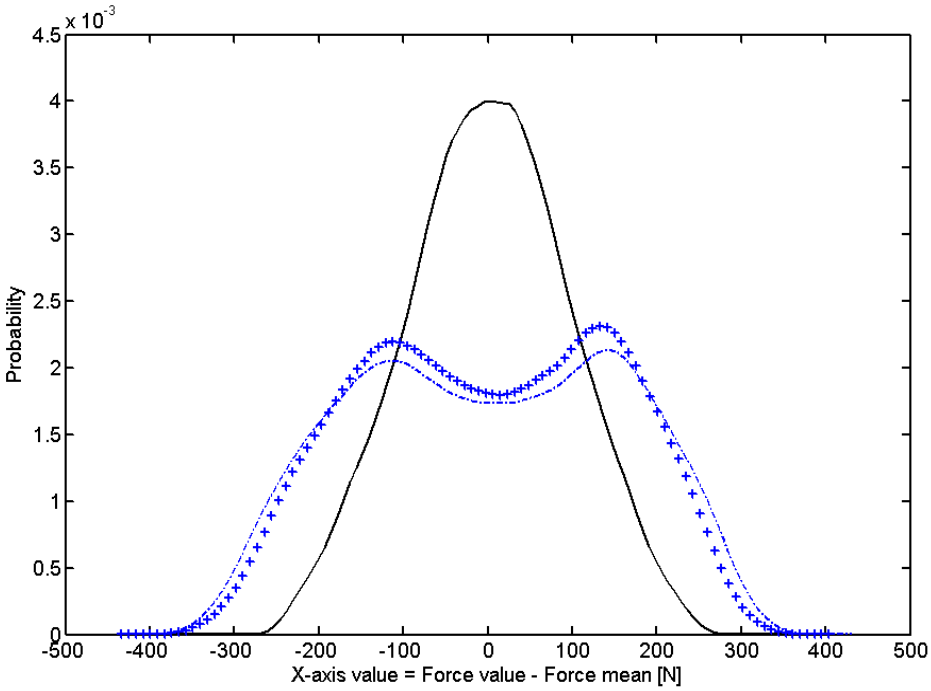

Figure 2.5: Probability density estimate of cutting-force signal: First pass (solid line), second pass (dotted line), third pass (crossed line) – each pass is equivalent to 367500 samples at $F_s = 15000\ Hz$.

2.4. MODELLING OF THE PASSIVE TOOL HOLDER

The tool-holder structure and the inactive SSA, positioned as shown in Figure 2.1, constitute a passive structure. The vertical tool-tip displacement is here called DOF 1 (first degree of freedom) and the vertical displacement of the actuator tool-holder connecting point is called DOF 2 (second degree of freedom) as shown in Figure 2.5. DOF 2 was introduced because the self-sensing actuator senses only the displacement of DOF 2, from which the displacement which here needs to be controlled, i.e. DOF 1, can be constructed mathematically. The shown passive structure has several modes. A constant or an FIR filter with only a few coefficients is therefore not sufficient to model the transfer behaviour from forces as inputs to DOF 1 and DOF 2 as outputs.

Modal models are therefore needed to model the passive tool-holder structure and incorporate its modes. The first model, $T_{11}(s)$, also mentioned in the previous section, is a model representing the contribution of the cutting force at the tool tip, $f_1(t)$, to the displacement that would occur at the tool tip, $r_1(t)$. The second model represents the contribution of the force at the actuator and structure's connecting point, $f_2(t)$, to the displacement, $r_1(t)$, at the tool tip and is denoted as

$T_{12}(s)$. The third model is $T_{22}(s)$. It is part of the term in (2.4) which is the contribution of the force, $f_2(t)$, at the connecting point to the displacement of the connecting point, $r_2(t)$. Specifically in this part of the work, which is a simulation using a self-sensing actuator, $T_{22}(s)$ serves as a model in the contribution of $f_2(t)$ to the displacement, $r_2(t)$, which is equivalent to what the self-sensing actuator measures, as in (2.4). The displacements at each DOF, $r_1(t)$ and $r_2(t)$, is caused by the joint influence of the two forces $f_1(t)$ and $f_2(t)$ at these two points. So, two equations are necessary to model the displacements of DOF 1 and DOF 2 because of the forces at these two points. They are given as follows in the Laplace-domain:

$$R_1 = T_{11}(s)F_1 + T_{12}(s)F_2 \tag{2.3}$$

$$R_2 = T_{21}(s)F_1 + T_{22}(s)F_2\ . \tag{2.4}$$

because of symmetry $T_{21}(s) = T_{12}(s)$. Three modal models are therefore needed to model the passive tool-holder structure and incorporate its modes.

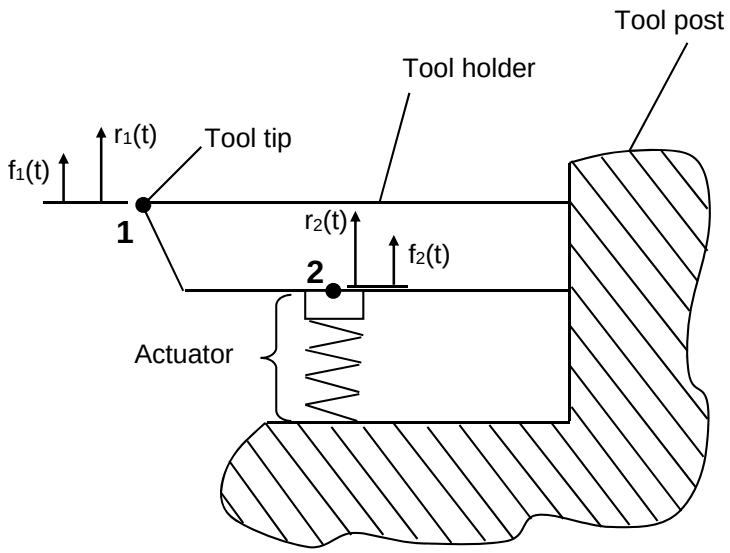

Figure 2.5: Tool holder and actuator with cutting and actuator forces.

In the frequency domain, the relationship between displacement vector $\boldsymbol{R}$ and input force vector $\boldsymbol{F}$ may be described by the dynamic flexibility matrix as

$$\boldsymbol{R} = [-\omega^2\boldsymbol{M} + j\omega\boldsymbol{C} + \boldsymbol{K}]^{-1}\boldsymbol{F} = \boldsymbol{T}(\omega)\boldsymbol{F} \tag{2.5}$$

and with $\boldsymbol{\Phi} = [\bar{\varphi}_1 , \bar{\varphi}_2 \ \ldots \ \bar{\varphi}_N]$, where $\bar{\varphi}_i$ is the orthonormal modal vector of the ith mode, using modal coordinates

$$\boldsymbol{R} = \boldsymbol{\Phi Z} = \boldsymbol{\Phi}\ diag\left\{\frac{1}{(\omega_i^2 - \omega^2 + 2j\xi_i\omega_i\omega)}\right\}\ \boldsymbol{\Phi}^T\boldsymbol{F}\,. \tag{2.6}$$

where $\boldsymbol{Z}$ is a vector of modal coordinates and where ω_i is the natural frequency, and the constant ξ_i represents the viscous modal damping ratio of mode i respectively. A modal damping ratio of $\xi_i = 0.01$ (Preumont, 2002:20) has been used throughout. The frequency responses $T_{11}(j\omega)$, $T_{12}(j\omega)$ and $T_{\boldsymbol{22}}(j\omega)$ are elements of the dynamic flexibility matrix

$$\boldsymbol{T}(\omega) = \sum_{i=1}^{N} \frac{\bar{\varphi}_i \bar{\varphi}_i^T}{(\omega_i^2 - \omega^2 + 2j\xi_i\omega_i\,\omega)}\,. \tag{2.7}$$

These modes were obtained from an eigenvalue extraction by means of the Lanczos method using MSC Nastran.

The passive tool holder/actuator structure was modelled as a supported cantilever in MSC Patran by using hex-8 elements for the tool holder. In order to account for the SSA connected to the tool holder, a grounded spring and a point mass were modelled and added at the SSA's point of connection to the tool holder. The values for this point mass and spring stiffness were those specified in technical data for the Pst 500/10/15 VS 18 actuator (from Piezomechanik GmbH).

The passive tool holder structure was modelled in MSC Patran as a cantilever supported by the SSA at an offset from the tool tip similarly to the configuration in Figure 2.5. The PTJNR-2020-16A tool holder was modelled with 6312 hex-8 elements in a finite element method (FEM), such that the $20 \times 20\ mm$ cross section consisted of 10×10 elements. Those nodes corresponding to the points of contact when clamped in the tool post of a Colchester Student lathe with $69.7\ mm$ overhang were constrained in all translational and rotational directions. In order to account for the SSA connected to the tool holder, a grounded spring and a point mass were modelled and added at the SSA's point of connection to the tool holder. With respect to this point of connection the overhang of the tool holder is $31.4\ mm$. The point mass was obtained from

$$m = \frac{K_a}{(2\pi f)^2} \tag{2.8}$$

Where K_a and f are the stiffness of $120\,kN/mm$ and resonance frequency of $27\,kHz$, respectively, specified for the SSA. The values for this point mass and spring stiffness were those specified in technical data for the Pst 500/10/15 VS 18 actuator (from Piezomechanik GmbH).

The clamping position of the tool holder as shown in Figure 2.1 is equivalent to the position when the cutting force was measured with the strain-gauged tool holder as described in the previous section. This position was at an increased distance from the tool tip to provide space for strain gauges. For the purposes of vibration control simulation, the same clamping position is used. However, the simulations are based on tool-tip displacement sensing that is done not by means of strain gauges but by means of a self-sensing actuator instead.

Figures 2.6 to 2.8 show the FEM-calculated frequency response functions of the three models. The residuals, $\varphi_{i_j}\varphi_{i_l}$, of the three modal models are given in Table 2.1 with the subscripts, j and l, referring to the respective DOF. These graphs as well as the residuals, from Table 2.1, indicate that modes above the chosen participating mode, Mode 2, have magnitudes less significant than the magnitude of Mode 2.

Table 2.1: Natural frequencies and residual values of passive-structure models

Mode i	$\omega_i/_{2\pi}$ [Hz]	$\varphi_{i_1}\varphi_{i_1}$ of $T_{11}(z)$	$\varphi_{i_1}\varphi_{i_2}$ of $T_{12}(z)$	$\varphi_{i_2}\varphi_{i_2}$ of $T_{22}(z)$
1	2859.6	0.0002	0.0002	0.0002
2	4152.7	21.8427	6.1581	1.7361
3	9764.6	12.8141	-1.4122	0.1556
4	13735	2.8190	-0.7420	0.1953
5	14412	4.3376	-1.5224	0.5343

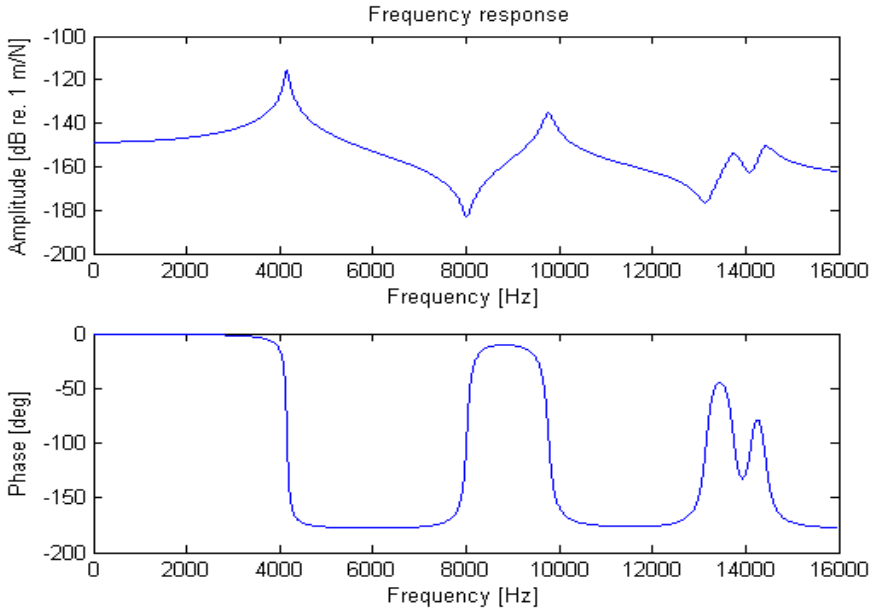

Figure 2.6: Frequency response of tool-holder collocated cutting-force path. Cutting force is input and tool-tip displacement is output (1st five participating modes of which the first is invisible).

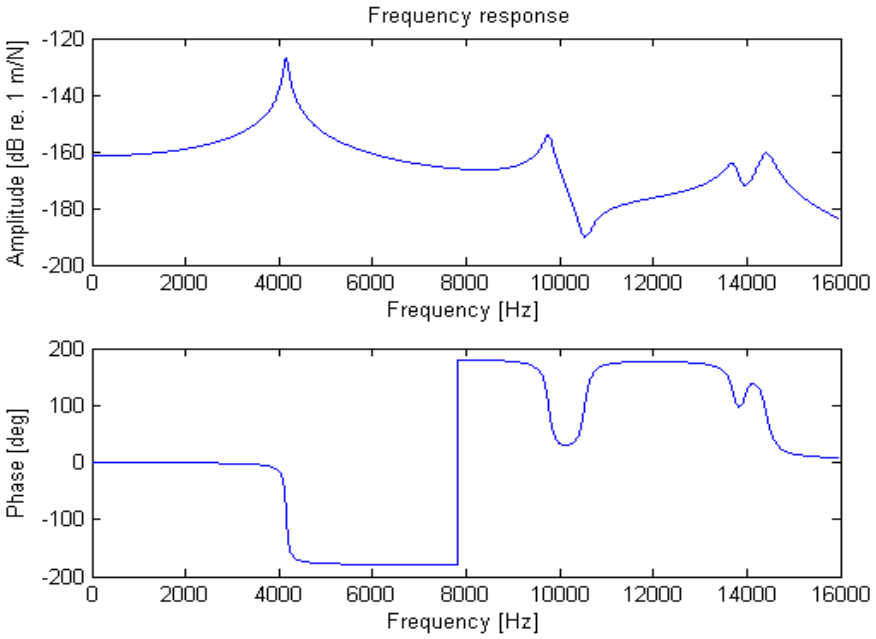

Figure 2.7: Frequency response tool-holder forward path when actuator is passive. Actuator force is input and tool-tip displacement is output (1st five participating modes of which the first is invisible).

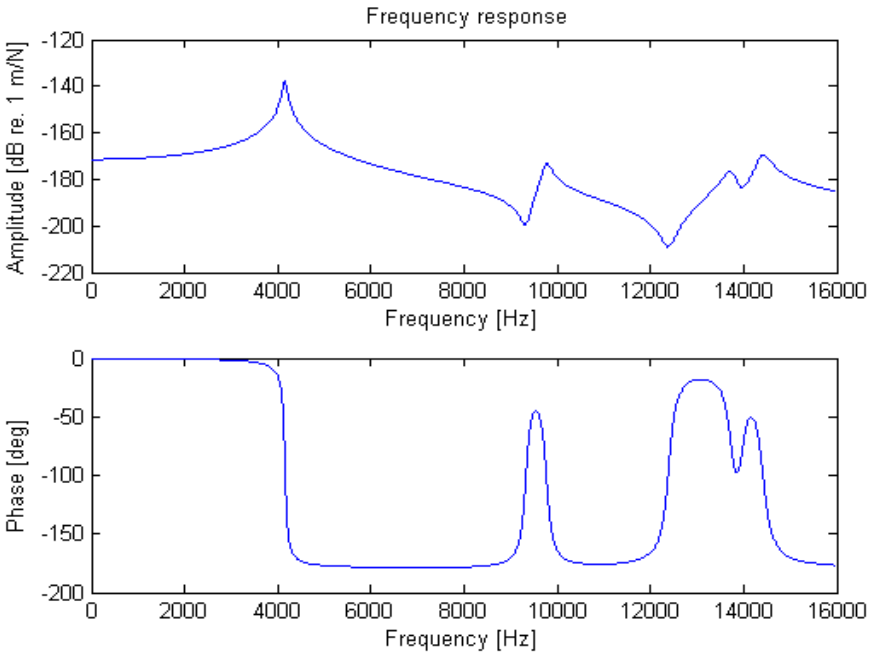

Figure 2.8: Frequency response of passive tool-holder collocated actuator path with actuator force as input and actuator extension as output (1st five participating modes of which the first is invisible).

2.5. MODELLING OF THE ACTIVE TOOL HOLDER

This section shows how the active actuator is incorporated into the structure with the relationship between the voltage applied to the actuator and the force generated by it, based on a derivation by Preumont (2002:58).

If a voltage, u, is applied to the actuator, its unconstrained extension is

$$\delta = g_a u \tag{2.9}$$

where g_a is the gain of the actuator, $g_a = n\, d_{33}$, with n the numbers of layers in the stack actuator and d_{33} a piezoelectric constant in [m/V].

The piezoelectric load along a line of action coaxial with the actuator is considered in the same fashion as if it were a thermal load. It is computed as

$$f_p = K_a \delta \,, \tag{2.10}$$

where K_a is the stiffness of the actuator. The actual load on the tool-holder structure at point 2, $f_{el_2}(t)$ will be proportional to the relative expansion, i.e. the elastic change in the length of the actuator. The elastic change in the length is the difference between the actual displacement of point 2, $r_2(t)$, and the unconstrained expansion, $\delta(t)$, for the given applied voltage, $u(t)$. Therefore $f_{el_2}(t)$ is given as

$$f_{el_2}(t) = K_a(r_2(t) - \delta(t)) \tag{2.11}$$

If f_p is handled in the same way as a thermal load, it can be made part of the stiffness force vector of the homogeneous equation of motion of the passive structure, so that the element of that vector corresponding to DOF 2 is equal to $f_{el_2}(t)$. If the f_p term of $f_{el_2}(t)$ is then brought to the right-hand side of the initially homogeneous equation of motion for the passive structure, the equation of motion then becomes

$$\boldsymbol{M\ddot{r} + C\dot{r} + Kr = f} \tag{2.12}$$

where f_p is an element of the force vector $\boldsymbol{f}$ and $\boldsymbol{M}$, $\boldsymbol{C}$ and $\boldsymbol{K}$ are the mass, damping and stiffness matrices respectively of the passive structure, which in this way also incorporate the mass of the actuator and its stiffness K_a. When substituting $r_2(t)$ in (2.11) with modal coordinates, one obtains

$$f_{el_2}(t) = K_a\left(\sum_{i=1}^{N} z_i(t)\, \varphi_{i_2} - g_a u\right) \tag{2.13}$$

From (2.6) one can see that the modal coordinates, z_i, in the frequency domain are

$$\boldsymbol{Z}(\omega) = diag\left\{\frac{1}{\omega_i^2 - \omega^2 + 2j\xi_i\omega_i\,\omega}\right\}\boldsymbol{\Phi}^T\boldsymbol{F}(\omega) \tag{2.14}$$

For the i'th mode, (2.14) becomes

$$Z_i(\omega) = \frac{1}{(\omega_i^2 - \omega^2 + 2j\xi_i\omega_i\,\omega)}\sum_{l=1}^{N_{dof}} \varphi_{i_l} F_l(\omega) \tag{2.15}$$

where N_{dof} is the number of degrees of freedom. Then for $F_l(\omega) = 0 \;\; \forall \; l \neq p$, $Z_i(\omega)$ becomes

$$Z_i(\omega) = \left(\frac{\varphi_{i_p}}{\omega_i^2 - \omega^2 + 2j\xi_i\omega_i\,\omega}\right) F_p(\omega) \tag{2.16}$$

In order to derive a relationship between the applied actuator voltage, $U(\omega)$, and the force, $F_{el_2}(\omega)$, exerted by the actuator on the structure at point 2, (2.13) becomes

$$\frac{F_{el_2}}{U} = K_a\left(\sum_{i=1}^{N}\frac{Z_i\varphi_{i_2}}{U} - g_a\right) \tag{2.17}$$

Substituting the modal coordinates Z_i of (2.15), and using $F_p(\omega)$ as the excitation at point 2, (2.17) becomes

$$\frac{F_{el_2}}{U} = K_a\left(\sum_{i=1}^{N}\frac{\varphi_{i_2}\varphi_{i_2}F_p}{(\omega_i^2 - \omega^2 + 2j\xi_i\omega_i\,\omega)U} - g_a\right) \tag{2.18}$$

Replacing U on the right-hand side of (2.18),

$$\frac{F_{el_2}}{U} = K_a\left(\sum_{i=1}^{N}\frac{\varphi_{i_2}^2F_pK_ag_a}{(\omega_i^2 - \omega^2 + 2j\xi_i\omega_i\,\omega)F_p} - g_a\right), \tag{2.19}$$

and simplifying (2.19), the transfer function from $U(\omega)$ to $F_{el_2}(\omega)$ becomes

$$\frac{F_{el_2}}{U} = K_ag_a\left(\sum_{i=1}^{N}\frac{\varphi_{i_2}^2}{(\omega_i^2 - \omega^2 + 2j\xi_i\omega_i\,\omega)}K_a - 1\right) = K_ag_a(T_{22}(\omega) - 1) = K_ag_aT_a(\omega), \tag{2.20}$$

where $F_2 = F_{el_2}$.

2.6. THE CONTROL METHOD

By means of the zero-order-hold all the s-domain transfer functions, $\boldsymbol{T_{11}(s)}$, $\boldsymbol{T_{12}(s)}$, $\boldsymbol{T_{22}(s)}$ and $\boldsymbol{T_a(s)}$ were converted to discrete filters in the z-domain and subsequently used as such $\boldsymbol{T_{11}(s)}$, $\boldsymbol{T_{12}(s)}$, $\boldsymbol{T_{22}(s)}$ and $\boldsymbol{T_a(s)}$ are proper transfer functions of which inversions are not realizable. But because the discrete versions of these models and inversions of some of them had to be used as part of the control algorithm they were inverted by incorporating their numerators in an all-pole IIR-filter and their denominators in an all-zero FIR-filter.

In this section, lower-case bold symbols are used for the vectors that represent sample sequences. All the subscripts k in this section, indicates a sample sequence of a signal at time t_k .

Proceeding with the model of the previous section, i.e. the tool holder supported by the passive actuator, Figure 2.9 shows how the transfer behaviour of the passive structure is accounted for in the simulation of the control system. That part of the block diagram surrounded by the dashed line constitutes the plant and the SSA, as represented during simulation. In the simulation used in this work, the plant and the SSA are represented by filters as shown in Figure 2.9. In this control system the plant is simulated with the path from the voltage, $\boldsymbol{u}'_k$, applied as a control input into the actuator and the tool-tip displacement, $\boldsymbol{y}_k$, induced by the actuator as the plant output. The voltage, $\boldsymbol{v}_{s\,k}$, is the voltage sensed by the SSA as a result of the displacement along DOF 2. The tool-tip displacement due to the cutting force, $\boldsymbol{f}_{1\,k}$, is represented here by $\boldsymbol{d}_k$ and the resulting tool-tip displacement is denoted by $\boldsymbol{e}_k = \boldsymbol{r}_{1\,k}$. The simulation of the voltage sensed by the SSA, $\boldsymbol{v}_{s\,k}$, due to the total displacement of the tool tip, $\boldsymbol{e}_k$, i.e. the sensing path, is that part of the block diagram lying between $\boldsymbol{e}_k$ and $\boldsymbol{v}_{s\,k}$.

$T_a(z)$ in the forward path, i.e. the plant, induces a behaviour which is initially divergent and finally convergent in its step response. Since the poles and zeros of $T_a(z)$ are located inside the unit-circle of the z-plane, one can apply pole-zero cancellation of $T_a(z)$ in the controller, which is that part in Figure 2.9 outside the dashed line. $T_c(z) = T_a^{-1}(z)$ is therefore used in the controller to compensate for $T_a(z)$ which induces the abovementioned divergent/convergent behaviour.

$T_{12}(z)$ is a simulation of the plant since its input is the actuator force, $\boldsymbol{f}_{2\,k}$, and the tool-tip displacement, $\boldsymbol{y}_k$, is its output. The displacement at point 2 (see Figure 2.5) is simulated by using (2.3) and (2.4) and solving for $\boldsymbol{r}_{2\,k}$. This displacement is due to the forces to which the structure, including the structural effects of the actuator, is subjected during the turning process. The voltage sensed by the SSA, $\boldsymbol{v}_{s\,k}$, at point 2 is

$$\boldsymbol{v}_{s\,k} = -Z_m(z)\boldsymbol{\Theta}\boldsymbol{r}_{2\,k} = K_m\boldsymbol{r}_{2\,k} \tag{2.21}$$

where $\boldsymbol{Z_m}(\boldsymbol{z})$ represents the sensing circuit and $\boldsymbol{\Theta}$ describes the SSA parameters according to the notation used by Anderson et al. (1994). The latter two are furthermore accommodated in the constant gain, $\boldsymbol{K_m}$, since all complex variables cancel out when the impedances appearing in the sensing circuit are assumed to consist of capacitors only.

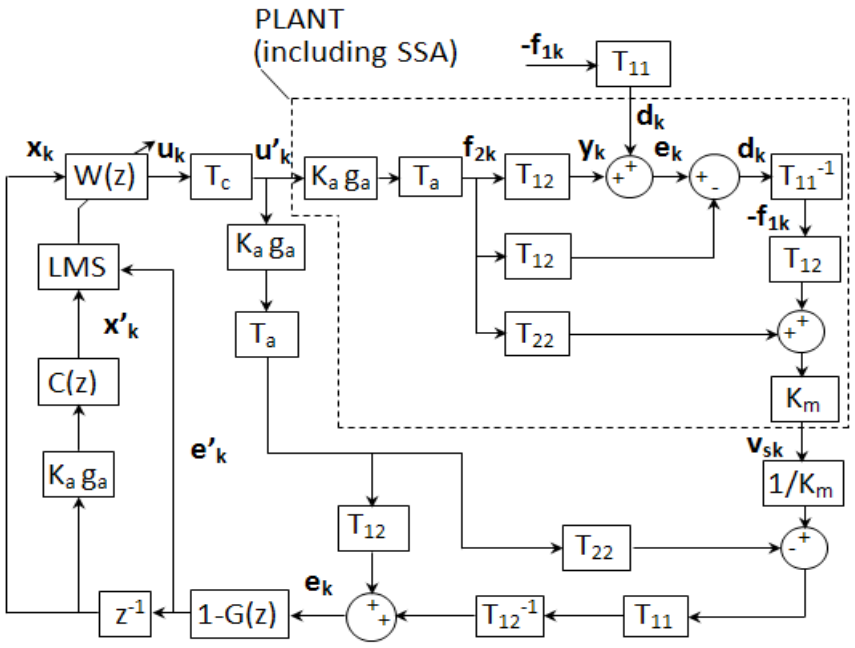

Figure 2.9: Block diagram of the tool vibration control system.

Operations exactly opposite to those in the simulation of $\boldsymbol{r}_{2\,k}$ are then done on $\boldsymbol{v}_{s\,k}$ in order to recover the error, $\boldsymbol{e}_k$, which is needed to compute the coefficients of the adaptive filter $\boldsymbol{W}(z)$. This section describes how this computation is done.

The model of the passive structure's forward path between a force input at the actuator position and its contribution to the total displacement of the tool tip as output, has poles and zeros and is given as.

$$T_{12}(z) = \frac{C(z)}{1-G(z)} = \frac{\sum_{i=0}^{LC-1} c_i z^{-i}}{\left(1-\sum_{j=1}^{LG} g_j z^{-j}\right)} \tag{2.22}$$

where LC and $LG$are filter lengths.

The transfer function of the passive structure with the force and the displacement at the actuator connection point as the collocated input and output respectively, has the same form as in equation (2.22) above, and is given as

$$T_{22}(z) = \frac{P(z)}{1-H(z)} = \frac{\sum_{i=0}^{LP-1} p_i z^{-i}}{\left(1-\sum_{j=1}^{LH} h_j z^{-j}\right)}. \tag{2.23}$$

where LP and LH are filter lengths again.

The error, $\boldsymbol{e}_k$, which is the resulting displacement of the tool tip in the direction of the cutting force, is given as

$$\boldsymbol{e}_k = \boldsymbol{y}_k + \boldsymbol{d}_k. \tag{2.24}$$

In order to obtain the plant output, $\boldsymbol{y}_k$, a force input from the actuator, $\boldsymbol{f}_{2\,k}$, is given to the plant, $T_{12}(z)$. When replacing $\boldsymbol{y}_k$ in (2.24) by

$$\boldsymbol{y}_k = T_{12}(z)\boldsymbol{f}_{2k}, \tag{2.25}$$

$\boldsymbol{e}_k$ is obtained with a dependency on the control input, $\boldsymbol{u}_k$, as

$$\boldsymbol{e}_k = K_a g_a T_{12}(z)\boldsymbol{u}_k + \boldsymbol{d}_k. \tag{2.26}$$

This is the error, i.e. the resultant displacement of the tool tip. For the sake of simplicity in this section, it is assumed that $T_c(z) = T_a^{-1}(z)$ so that $T_c(z)$ and $T_a(z)$ are perfectly cancelled. To prevent the poles of the passive tool-holder structure from participating in the error signal, the error, $\boldsymbol{e}_k$, is pre-filtered with the poles of $T_{12}(z)$. The new error, $\boldsymbol{e}'_k$, becomes

$$\boldsymbol{e}'_k = \big(1 - G(z)\big)\boldsymbol{e}_k = K_a g_a C(z)\boldsymbol{u}_k + \big(1 - G(z)\big)\boldsymbol{d}_k. \tag{2.27}$$

The minimization of $\boldsymbol{e}'_k$ can be done by finding the coefficients, w_i, of the adaptive FIR-filter, that minimize the expected value of the squared error, expressed as the cost function

$$J(w_i) = E\big[\boldsymbol{e}'_k \boldsymbol{e}'^T_k\big]. \tag{2.28}$$

This search for coefficients, w_i, occurs along the direction of the negative gradient,

$$\frac{\partial J}{\partial \boldsymbol{w}_k} = 2\boldsymbol{e}'_k \frac{\partial \boldsymbol{e}'_k}{\partial \boldsymbol{w}_k}, \tag{2.29}$$

towards the minima of the quadratic error surface, also known as performance surface. The coefficients, w_i, are updated for each time-step, using

$$\boldsymbol{w}_{k+1} = \boldsymbol{w}_k - \mu \frac{\partial J}{\partial \boldsymbol{w}_k}. \tag{2.30}$$

Since

$$\boldsymbol{u}_k = W(z)\boldsymbol{x}_k = \sum_{i=0}^{LW-1} w_i \boldsymbol{x}_{k-i} \,, \tag{2.31}$$

with LW the adaptive filter length, the derivative term in the above equation is determined from

$$\frac{\partial e'_k}{\partial \boldsymbol{w}_k} = K_a g_a \sum_{i=0}^{LC-1} c_i x_{k-i} \,, \tag{2.32}$$

which is the reference signal, $\boldsymbol{x}_k$, filtered.

Inserting the corresponding terms, the final updating (2.30) for the adaptive filter coefficients become

$$\boldsymbol{w}_{k+1} = \boldsymbol{w}_k - \alpha e'_k K_a g_a C(z)\boldsymbol{x}_k \,, \tag{2.33}$$

where $\alpha = 2\mu$ is a convergence coefficient, computed as in Elliott (2001:78,82) as

$$\alpha = \frac{\tilde{\alpha}}{I\overline{\boldsymbol{x}'_k{}^2}} \,. \tag{2.34}$$

Here $\overline{\boldsymbol{x}'_k{}^2}$ is the mean-square of the filtered reference signal, $\boldsymbol{x}'_k$, as indicated in Figure 2.9, and L represents the number of adaptive filter coefficients and

$$0 < \tilde{\alpha} < 2. \tag{2.35}$$

One advantage of the LMS algorithm is that the terms in the cost function, such as the term due to the disturbance by the cutting force, which are not dependent on the adaptive filter weights, vanish in the gradient.

2.7. SIMULATION RESULTS

It was found that if the poles and zeros of the compensator, $T_c(z)$, are not accurately placed, i.e. $T_c(z) \approx T_a^{-1}(z)$ and their real and imaginary parts are 10% closer to the origin in the z-plane, an even better vibration control can be obtained. The simulations discussed in this section were therefore done under the above-mentioned conditions.

Simulations were performed with the SSA in two different positions:

Position A: The SSA is connected at the bottom surface of the tool holder at an offset from the tool-holder tip.

Position B: The SSA is connected at the bottom surface at the tip of the tool holder.

Initially a sampling frequency of $F_s = 45kHz$ was considered for the simulation of the vibration control system. With the SSA at position A, the percentage reduction of the displacement r.m.s. of the tool tip was only 88%. It is interesting to note that in order to increase the performance of the vibration control by decreasing the frequency of the participating modes, a mass of approximately $0.57\ kg$ would have to be added to the tool holder close to its tip. This would increase the overall reduction performance of the tool-tip vibration r.m.s. by 7%. It is, however, more appropriate to increase the sampling frequency of the vibration control system to $F_s = 90kHz$. The reason for choosing this sampling frequency is to enable the control system to function more accurately due to more accurate models. The improved accuracy results from a shorter one-sample-delay which is introduced by the zero-order-hold when the models are converted from the continuous s-domain to the discrete z-domain. The choice of the above-mentioned two sampling frequencies was based on the commonly used guideline for the implementation of digital control systems, where $\omega_s = 2\pi F_s > 10\omega_b$. Here ω_b is the bandwidth of the closed-loop control system. In the control system, as used in this work, the bandwidth was taken to be equivalent to the highest participating mode, i.e. mode 2. Thus the lower bound for ω_s is $10\ \omega_b$ but at $\omega_s = 20\omega_b$, $T(s) \approx T(z)$. This can be seen by inspection of the bode plots of $T(s)$ and $T(z)$ respectively. In Seborg et al. (1989) it can furthermore be seen that

$$\lim_{T_s \to 0} H(z)T(z) = T(s)\ , \tag{2.36}$$

where $T(s)$ is the sampling time and

$$H(s) = \frac{1-e^{-sT_s}}{s} \tag{2.37}$$

is the zero-order hold.

Figures 2.10 and 2.12 show the tool-tip displacements as the uncontrolled vibrations, $d(t)$, and the controlled vibrations, $e(t)$, in the form of a time domain plot for the actuator in positions A and B respectively. The power spectral densities for case A and B are shown in Figures 2.11 and 2.13

respectively. Table 2.2 shows the percentage reductions of the displacement r.m.s. values for the resulting motion of the tool tip, $e(t)$, with the SSA in the above-mentioned two positions. The results indicate that the percentage reduction of displacement r.m.s. with the SSA in position A is higher than with the actuator in position B. When looking at the overall reduction, however, i.e. from the displacement r.m.s. with the passive SSA at position A to the displacement r.m.s. with the active SSA at position B, one can see that the reduction with the actuator in position B is higher than with the actuator in position A. When the actuator is in position B, therefore, the vibrations are reduced by a combination of the increased stiffness of the passive structure and the active vibration control. This shows that although having the SSA at position B is more effective in reducing the overall vibration, the SSA at position A would be a more practical way to control tool vibrations because it is out of the way of the tip where the cutting takes place.

Back to Figures 2.10 and 2.12 it is clear that they show the overall higher reduction in tool tip displacement with the SSA passive at A to the displacement with the SSA active at B.

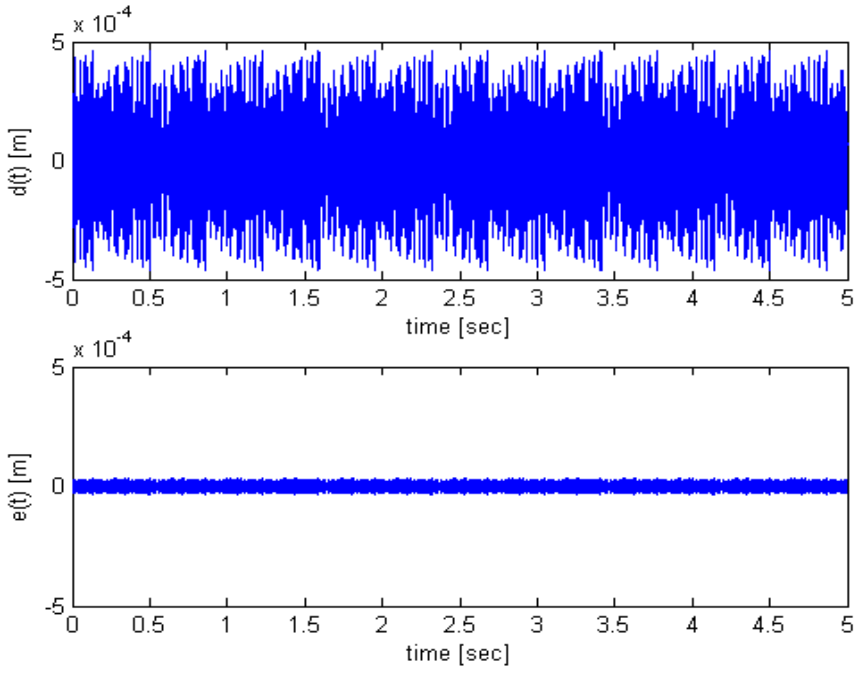

Figure 2.10: Cutting-force-induced vibrations, $d(t)$, and resultant vibrations, $e(t)$, with SSA below the tool holder at an offset from the tool tip (position A).

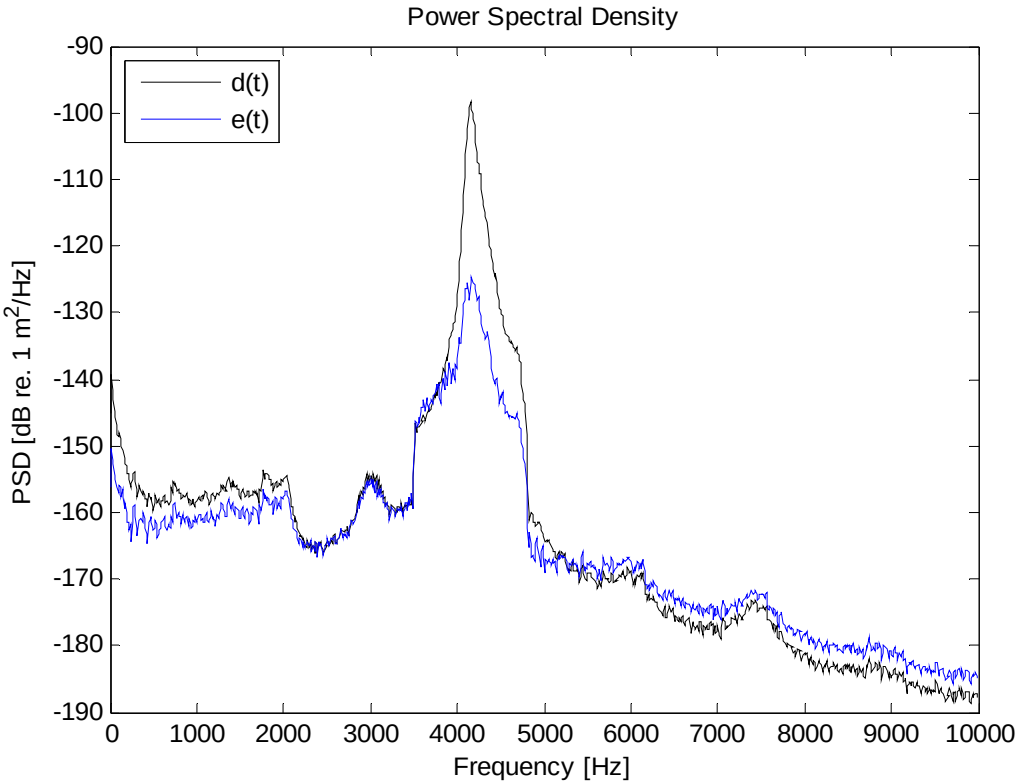

Figure 2.10: PSD of cutting-force-induced vibrations, $d(t)$, and resultant vibrations, $e(t)$, with SSA below the tool holder at an offset from the tool tip (position A).

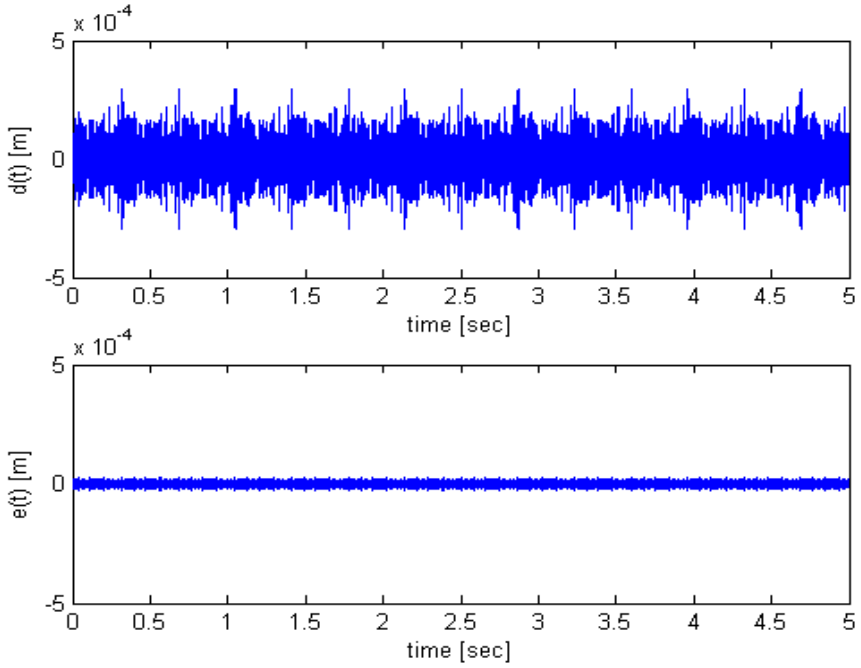

Figure 2.11: Cutting-force-induced vibrations, $d(t)$, and resultant vibrations, $e(t)$, with SSA below the tool holder and tool tip (position B).

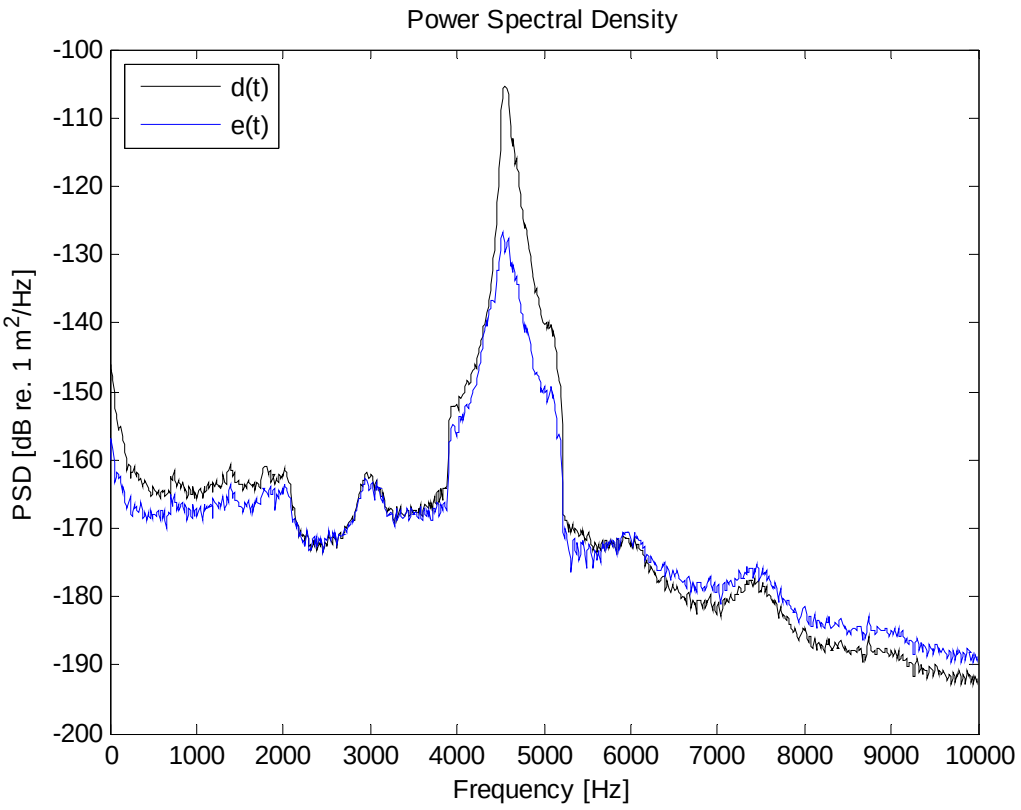

Figure 2.12: PSD of cutting-force-induced vibrations, $d(t)$, and resultant vibrations, $e(t)$, with SSA below the tool holder and tool tip (position B).

Table 2.2: Percentage reduction of displacement r.m.s., from $d(t)$ to $e(t)$, after 0.0111 secs.

	$d(t)[m]$	$e(t)[m]$	**Percentage reduction**
State of SSA	passive	active	
SSA at position A	1.62×10^{-4}	1.18×10^{-5}	93%
SSA at position B	8.04×10^{-5}	8.54×10^{-6}	89%

2.8. LIMITATIONS

Resulting from the structural model and the control system chosen, there are two main limitations to this concept.

- While the system is expected not to be limited to the cutting of specific work piece shapes or materials, it is assumed that a specific tool post, tool holder and insert is used in a single-point turning process and that the clamping conditions are repeatable.
- The unique feature of this self-sensing concept compared to conventional control with direct measurement of the plant output, is that here the plant output has to be recovered from a signal picked up by the SSA. This is done, by using models of the structure. The accuracy of the recovered plant output thus depends on the accuracy of the models. The results obtained in this simulation are expected to be the best possible results obtainable in practice since the models used for plant output recovery are identical to the models representing the plant.

2.9. CONCLUSION

It has been shown through simulation that the concept of a self-sensing actuator (SSA) can be applied to the turning process. IIR-filters were used in the simulation of the tool vibration control system to represent the discrete transfer functions of the passive tool-holder structure. The stability requirements for the use of IIR-filters in the mechanical structure of the control system had to be met by using the known principle of pre-filtering of the error signal with the poles of the structure. It has been shown that the position of the SSA plays a significant role in the performance of the control system and that a displacement r.m.s. reduction of 93% is possible with the SSA in a practical position at an increased offset from the tool tip. One could argue that given that estimates of the plant were perfect the simulation results should be perfect also. However the disturbance, i.e. the tool vibrations, is random and therefore non-deterministic. This means they cannot be predicted with 100 % precision. Another point is that, as mentioned in section 1.1.3 in the previous chapter turning process tool vibration are non-stationary the adaptive filter coefficients must be updated each sample and can’t converge to constitute an optimal filter (Elliott, 2001:77).

CHAPTER 3

COMPARING ORTHOGONAL FORCE AND UNIDIRECTIONAL STRAIN COMPONENT PROCESSING FOR TOOL CONDITION MONITORING

3.1. INTRODUCTION

This chapter gives an evaluation of the potential sensing capabilities that lie in a self-sensing actuator. While in the previous chapter the focus was on its ability to be used in the structural conditions of a turning process as feedback signal for tool vibration control the focus is here directed at its usefulness in tool condition monitoring (TCM). The main contents of this chapter consist of the paper by Freyer, Heyns & Theron (2014).

In harsh machining circumstances tool condition monitoring sensors may have to be embedded or semi-embedded in a tool holder in such a way that they do not interfere with the cutting process. A single axis sensor might then only be able to provide a signal, which is a linear combination of the orthogonal cutting force components. An example of such an application would be a piezoelectric self-sensing actuator (SSA) used as a sensor and an actuator simultaneously in the active control of vibrations. The signal from the SSA, which is the feedback signal for the vibration control system, could be made available for TCM while simultaneously playing a role in tool vibration control.

In TCM the measurement of its orthogonal components often provides the necessary cutting force information as can be found in the work of Jemielniak et al. (1989), Purushothaman (2010) and Sharma, Sharma, & Sharma. (2008). This part of the work however compares TCM based on orthogonal forces to the one based on measurement of only the unidirectional strain signal. An opportunity for the application of the latter comes with the implementation of the SSA concept in turning processes. The SSA senses the strain caused by a linear combination of the orthogonal cutting force components. With a single-stack SSA it is possible to sense only the unidirectional strain it experiences, so that only the joint effect of the tangential, feed and thrust components of the cutting force can be exploited in TCM and not the effect of the individual components.

The main topic explored in this chapter is the feasibility of a monitoring system. This system makes use of a signal, which is a linear combination of the cutting force components. It is compared to a reference case, which is a system using signals of the individual orthogonal force components themselves. The focus is therefore on the comparison of two different cases of input signals to the monitoring systems used for the same TCM algorithm in each case. The focus is therefore not on the TCM algorithm itself, since the latter is already known in literature (Scheffer, Kratz, Heyns & Klocke, 2003; Sick, 2002). Part of the objective for this work was to use typical rather tool holder models which would be validated against real tool holders. For this work is it an objective this part of the study is also a step towards the implementation of a SSA-based TCM system. The main question pertaining to this monitoring problem is whether the difference in performance between the proposed way of monitoring and the reference case is sufficiently small to justify implementation of such a monitoring system.

Neural networks (NN) are commonly used for TCM (Scheffer et al., 2003; Liu et al., 1998). In the case of Liu et al. (1998) it is argued that their particular NN algorithm is dependent on the robustness and practicality of cutting-force sensors. This is an argument assumed here to be applicable to all NN-type TCM algorithms. This argument favours an investigation into monitoring done with a piezoelectric transducer, semi-embedded underneath the tool holder. The research on the simultaneous monitoring of tool condition and vibration control capabilities may improve the versatility of the tool holder and may also pave the way for a fully embedded transducer. This could mean almost eliminating its interference with the performance of the tool, which is important in this context as Lundholm, Yngen & Lindström (1988) have put it.

Literature reports on various measurement systems, depending on the type of measured variable for TCM. When cutting force is the measured variable for TCM, it is often acquired by means of dynamometers (Bahre et al., 1992:65; Seah, Li & Lee, 1995; Audy, 1992). Others have used accelerometers to measure tool vibration (Bonifacio et al., 1994; Abouletta et al., 2001) whereas methods based on strain gauges are used for measuring either cutting forces as in Scheffer et al. (2003) or vibrations as in Li & Ulsoy (1999). Papers by Cho et al. (1999) as well as Sick (2002) show that cutting force is the process variable that is most commonly used for tool wear monitoring. It was therefore decided to measure cutting forces using a strain gauge instrumented tool holder.

The signals sensed with the strain gauge instrumented tool holder were converted into the dynamic force acting at the tool tip. In aid of this conversion was a modal state space model of this tool holder. A Laplace domain model of the tool holder for use with the SSA supplied the parameters when the dynamic force signal was filtered to simulate the correct strain signal that would be measured by the SSA.

Work by Sick (2002), Scheffer et al. (2003), Choudhury et al.(2003) as well as Liu et al. (1998) was used as the basis for the tool wear-monitoring aspects pertaining to the use of NNs. The use of wavelet packet analysis for the computation of tool wear sensitive features was adopted from Wu and Du (1996) and Pal, Heyns, Freyer, Theron & Pal (2011). In chapter 2 vibration control in a turning process using an SSA was already suggested (Freyer et al., 2008). This chapter however discusses how a linear combination of the force components is associated with their use in TCM.

The following section shows how the force component, to be used for the SSA involved TCM, can be reconstructed from signals of a strain gauge instrumented tool holder. The content of the section on data acquisition, describes an experiment conducted to obtain data on cutting forces and flank wear. The sections on feature selection and data-processing methods then follow with the latter, containing the artificial intelligence basis of the TCM. A statistical presentation of the results is then given in the next section. This means that the actual signal processing for TCM purposes is only contained in the section on data-processing, while the preceding sections describe measurements and modelling performed to provide the data for this investigation, however as mentioned above the objective of this investigation is a comparison of TCM based on orthogonal versus unidirectional sensed signals.

3.2. RECONSTRUCTUION OF UNIDIRECTIONAL SENSED STRAIN SIGNAL

3.2.1. Modelling problem definition

The SSA tool holder configuration shown in Figure 3.1 represents the configuration considered here for investigating the concept of simultaneous tool vibration control and TCM. It must be remarked however that this configuration could not be used in the implementation

of the control system later discussed in Chapter 4. This is because Chapter 4 as the final main chapter indicates how far this work could progress given the time constraints on the project.

The signals that are normally desired for TCM purposes are the components, f_{1x}, f_{1y} and f_{1z} of the cutting force $\boldsymbol{f}_1$, acting at node 1, as shown in Figure 3.1. However, the SSA can only sense its own axial strain, which results from the external forces and also the voltage applied to it as elaborated in Anderson et al. (1994). The displacements $u_{1x}(t)$ and $u_{2z}(t)$ of the tool holder in Figure 3.1 are a result of all the forces acting on this structure, namely the components of $\boldsymbol{f}_1$ and $\boldsymbol{f}_2 = f_{2z}$. Due to the voltage that would normally be applied to the SSA it exerts the actuation force f_{2z} on the tool holder at node 2, as indicated in Figure 3.1. It is assumed that there is no displacement at node 3 and that the SSA can therefore be assumed being grounded at this node. In the Laplace domain, $u_{1x}(t)$ and $u_{2z}(t)$ can be represented by the following relationships:

$$\begin{bmatrix} U_{1x} \\ \vdots \\ U_{2z} \\ \vdots \\ V_{nz} \end{bmatrix} = \begin{bmatrix} T_{1x1x} & T_{1x1y} & T_{1x1z} & \cdots & T_{1x2z} & \cdots & W_{1zmz} \\ \vdots & \vdots & \vdots & \ddots & \vdots & \ddots & \vdots \\ T_{2z1x} & T_{2z1y} & T_{2z1z} & \cdots & T_{2z2z} & \cdots & W_{2zmz} \\ \vdots & \vdots & \vdots & \ddots & \vdots & \ddots & \vdots \\ T_{nz1x} & T_{nz1y} & \cdots & \cdots & \cdots & \cdots & W_{nzmz} \end{bmatrix} \begin{bmatrix} F_{1x} \\ F_{1y} \\ F_{1z} \\ \vdots \\ F_{2z} \\ \vdots \\ M_{nz} \end{bmatrix} \tag{3.1}$$

where models T_{ivjw} represent force F_{jw} to translation U_{iv} transfer functions and W_{ivjw} represent moment M_{jw} to torsion V_{iv} transfer functions. Their subscripts i and j refer to the nodes of output and input respectively. Subscripts v and w refer to the x-, y- or z-axis of the corresponding output displacement and input force respectively. It is here dealt with the influence of $\boldsymbol{f}_1(t)$ on $u_{2z}(t)$ only i.e. with the SSA as a passive element of the tool holder structure. With $f_{2z} \neq 0$, the SSA would be active. From (3.1) only displacements U_{1x} and U_{2z} will henceforth be considered. The displacements and rotations at the remaining nodes will be discarded.

A model of the Mitsubishi DTGNR 2525 M16-type tool holder was created in MD Patran. This tool holder with the SSA support brackets (Figures 3.1 and 3.2), are modelled as one solid part. It was meshed with 91361 tet10 elements, which had edge lengths of typically 2 mm. The SSA was modelled as a 1-D bar with a mechanical stiffness K_a equal to that of the Piezomechanik GmbH-type PSt 500/10/15 VS 18 piezoelectric stack actuator.

In this part of the work $\boldsymbol{f}_1(t)$ has been determined from signals sensed by tool holder equipped with strain gauges as shown in Figure 3.3. How the force $\boldsymbol{f}_1(t)$ is reconstructed from the strain gauge signal is described in the following section.

The strain gauges of the half bridges had a length of 3 mm and of 6 mm in the full bridge, which make measurement at least up to frequencies such as 20 kHz possible according to a relationship between peak strain and frequency for a certain gauge length. The paper of Swantek, Wicks & Wilson (2001) contains such a relationship.

The tool holder in Figures 3.3 and 3.4 a Seco PTJNR-2020-16A, was modelled as a cantilever clamped as shown in Figure 3.5. It was modeled with 6312 hex-8 elements in a finite element method (FEM), such that the cross section of 20 × 20 mm consisted of 10 × 10 elements. The tool holder had an overhang of 69.7 mm and those nodes corresponding to the points of contact when clamped in a tool post of a Colchester Student lathe were constrained in directions of translation and rotation. The strain gauge protection as well as weight of cabling in a conduit was modelled as a point mass $m_{pm} = 0.58196\ kg$ located at the centre of this protection. The reason for this particular value lies in the requirement to set the frequency of the first bending mode of the model equal to the equivalent frequency observed on the real strain gauge instrumented tool holder. This setting was done by adjustment of m_{pm}.

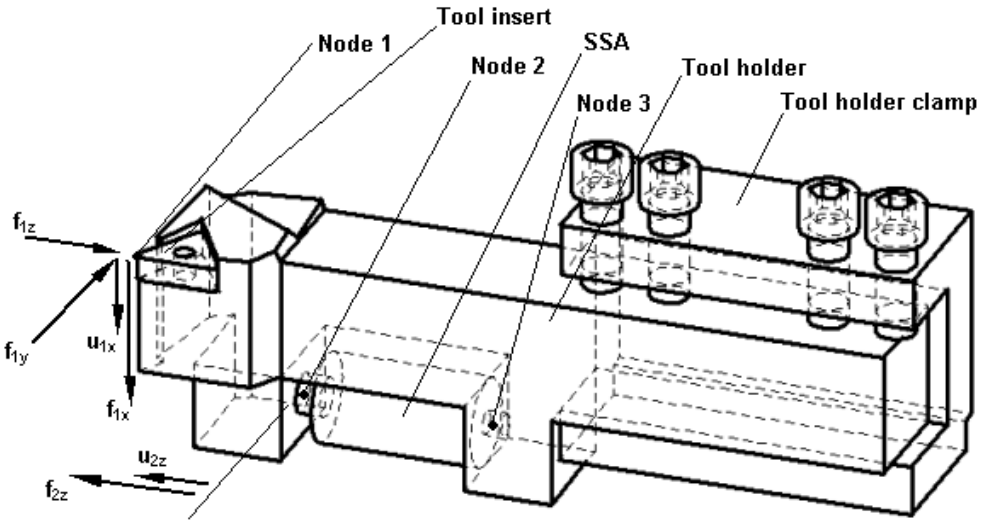

Figure 3.1: Tool holder and SSA with degrees of freedom indicated

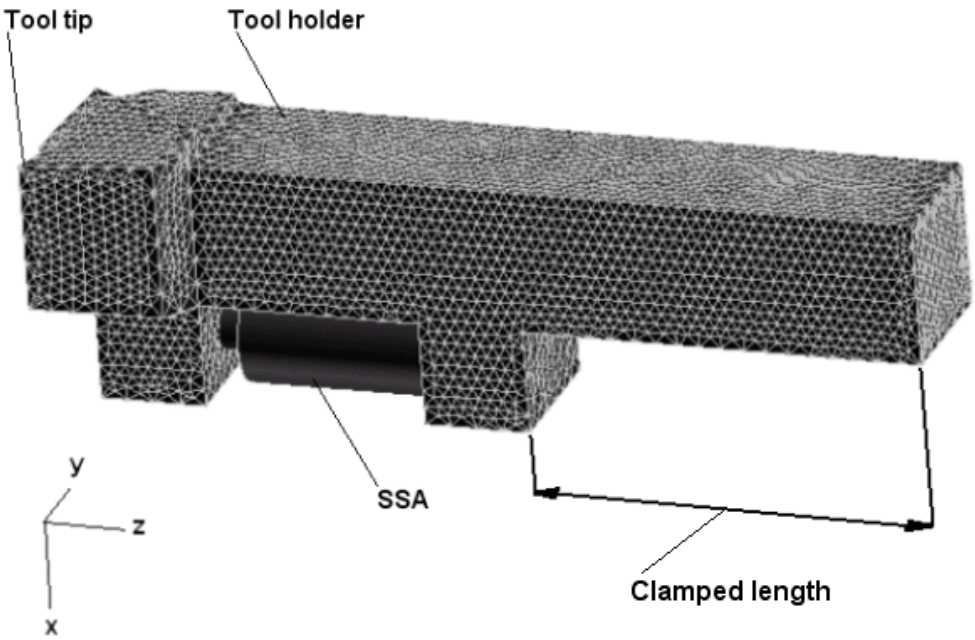

Figure 3.2: FE model of Mitsubishi DTGNR 2525 M16-type tool holder and SSA

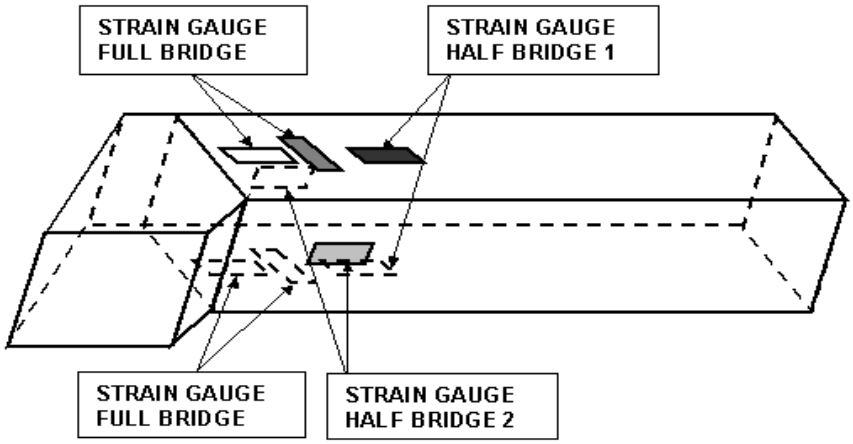

Figure 3.3 : Strain gauge (SG) instrumented Seco PTJNR-2020-16A tool holder with SG1 dark-gray, SG2 light-gray and SG3 gray.

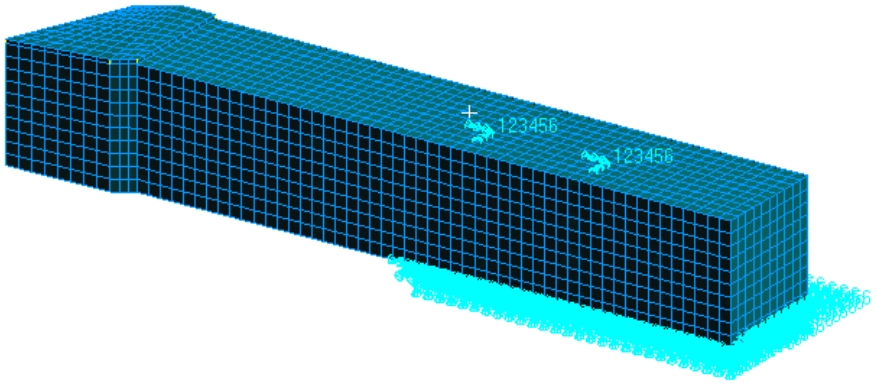

Figure 3.4 : FE model of strain gauge (SG) instrumented Seco PTJNR-2020-16A tool holder with light blue markers for constrained nodes where it's clamped.

The strain gauge half bridges were placed at a position where sufficient strain due to bending could be sensed. In order to let this bending happen an abnormally long overhang of the tool holder was chosen.

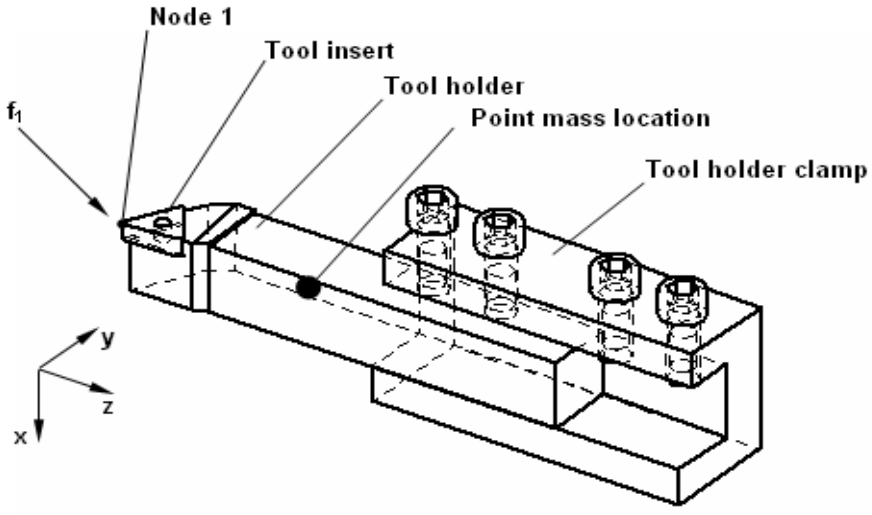

Figure 3.5: Strain gauge instrumented tool holder as clamped

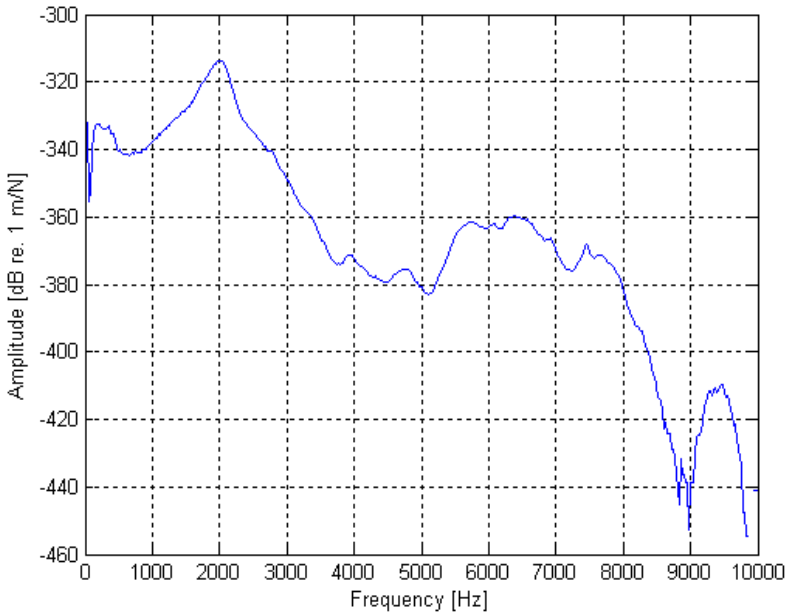

Figure 3.6: Frequency response from strain gauge instrumented tool holder when clamped with force and displacement at tool tip as input and output respectively.

To be able to reconstruct the dynamic force at the tool tip one only has the modal properties of the tool holder and measurements of three strain gauge bridges. In order to have a model linking displacement to input force and with the absence of mass stiffness and damping matrices, it is convenient to work in the modal domain and then also with some input-output (I/O) model of which one can transform the output to a variable with physical meaning.

Without two operations, one being an I/O model having forces as input and modal coordinates, as output and successive transformation from modal to physical coordinates the modelling problem would be more complicated. An I/O model however can be formulated to make the required variable accessible at the output, e.g. in state space formulation, as given in Balmés & Leclère (2003). Even though only 3 inputs and outputs are required in this part of the work the latter is a manageable type of a multivariable model and has advantages over e.g. Laplace domain models especially for higher numbers of I/O variables.

A reconstruction of $f_1(t)$ from the available strain gauge measurement was therefore done by means of a multi-input-multi-output (MIMO) state space formulation of the structural dynamics in the modal domain. Even though a model in the modal domain, physical displacements become accessible at the output by means of a transformation. Likewise strains

can be made accessible by means of transformation with a strain eigenvector. Its relationship with displacement modes is shown in the following subsection.

3.2.2. Modeling problem description

The following symbols are among those used for the formulation of a model, which has strain measurements as inputs and dynamic force components at the tool tip as outputs.

p_j: modal coordinate corresponding to mode j

p_j^{ε}: strain modal coordinate corresponding to mode j

$\boldsymbol{x}$: $n \times l$ physical coordinate, such that $\boldsymbol{x} = \boldsymbol{\Phi}\, \boldsymbol{p}$

$\boldsymbol{u}$: $n \times l$ displacement vector

$\boldsymbol{r}$: $n \times l$ position vector

$\boldsymbol{\varepsilon}$: strain tensor

$\boldsymbol{\Phi}$: $n \times m$ modal matrix with displacement eigenvectors as columns, n DOFs and m modes

$\boldsymbol{\phi}_j$: j'th normal mode of the system

ϕ_{ji}: i'th entry of j'th normal mode of the system

$\boldsymbol{\psi}_j$: strain eigenvector tensor for mode j

ψ_{jkl}: component (k, l) of strain eigenvector tensor for mode j

$\boldsymbol{\Omega}^2$: $\boldsymbol{\Omega}^2 = diag\left(\boldsymbol{\omega}_i^2\right),\ \ i = 1,2, \ldots m$, where m is the number of modes

$\boldsymbol{\Gamma}$: $\boldsymbol{\Gamma} = \mathbf{2}\boldsymbol{\xi}\boldsymbol{\Omega}$ where $\boldsymbol{\xi} = diag(\xi_i),\ \ i = 1,2, \ldots m$

$\boldsymbol{E}_{S2}$: vector of three Laplace domain strain outputs at selected DOFs, set $S2$ of DOFs

$\boldsymbol{F}_{S1}$ vector of three Laplace domain input force components for translation DOFs at tool tip, set $S1$ of DOFs

$\boldsymbol{b}$: $n \times 3$ locating matrix with $b_{ij} = 1$, for translation DOFs at tool tip, set $S1$ of DOFs

$\boldsymbol{c}$: $3 \times n$ locating matrix with $c_{ij} = 1$ at DOFs for selected outputs, set $S2$ of DOFs

ξ_i is the viscous modal damping and ω_i the natural frequency at mode i. For the first five modes the damping has been determined from the percentage overshoot (Dorf & Bishop, 2005:251) of the tool tip at each mode during a sudden release test of the tool holder in Figure

3.3. ξ_1 to ξ_3 have been determined as 0.4468, 0.4605, and 0.4076 while ω_1 to ω_3 were found at $1978\,Hz$, $2100\,Hz$ and $4169\,Hz$ from FEM software MD Nastran, where ω_2 corresponds to the first bending mode of this tool holder around the y-axis. The bending mode is also shown in the frequency response function of Figure 3.4. Since the eigenvectors are produced in a normal mode solution type in Nastran we can write the following state-space representation of our normal mode model:

$$\begin{Bmatrix}\dot{\boldsymbol{p}}\\ \ddot{\boldsymbol{p}}\end{Bmatrix} = \begin{bmatrix}\mathbf{0} & \boldsymbol{I}\\ -\boldsymbol{\Omega^2} & -\boldsymbol{\Gamma}\end{bmatrix}\begin{Bmatrix}\boldsymbol{p}\\ \dot{\boldsymbol{p}}\end{Bmatrix} + \begin{bmatrix}\mathbf{0}\\ \boldsymbol{\Phi^T b}\end{bmatrix}\{\boldsymbol{f}(t)\} \tag{3.2a}$$

$$\{\boldsymbol{u}(t)\} = [\boldsymbol{c\Phi} \quad \mathbf{0}]\begin{Bmatrix}\boldsymbol{p}\\ \dot{\boldsymbol{p}}\end{Bmatrix} \tag{3.2b}$$

Our problem is as follows. In (3.2) we have three time-varying input force components at three DOFs of the tool tip and three time varying displacements at the output $\boldsymbol{u}(t)$. Pisoni, Santolini, Hauf & Dubowsky (1995) show that from the relationship of the strain tensor at each position to the displacements in the structure,

$$\boldsymbol{\varepsilon}(\boldsymbol{r},t) = \frac{1}{2}\left(\frac{\partial \boldsymbol{u}}{\partial \boldsymbol{x}} + \left[\frac{\partial \boldsymbol{u}}{\partial \boldsymbol{x}}\right]^T\right) = \sum_{\boldsymbol{j=1}}^{\infty}\frac{1}{2}\left(\frac{\partial \boldsymbol{\phi}_j(\boldsymbol{r})}{\partial \boldsymbol{x}} + \left[\frac{\partial \boldsymbol{\phi}_j(\boldsymbol{r})}{\partial \boldsymbol{x}}\right]^T\right)p_j(t) \tag{3.3}$$

an equivalent relationship of the strain eigenvector tensor $\boldsymbol{\psi}_j(\boldsymbol{r})$ for mode j and at each position of the system in terms of the j'th normal mode, $\boldsymbol{\phi}_j$, of the system as

$$\boldsymbol{\psi}_j(\boldsymbol{r}) = \frac{1}{2}\left(\frac{\partial \boldsymbol{\phi}_j(\boldsymbol{r})}{\partial \boldsymbol{x}} + \left[\frac{\partial \boldsymbol{\phi}_j(\boldsymbol{r})}{\partial \boldsymbol{x}}\right]^T\right), \qquad j = 1, \ldots \infty\ . \tag{3.4}$$

The strain field in the structure is given in terms of the strain eigenvector tensors as

$$\varepsilon(\boldsymbol{r},t) = \sum_{j=1}^{\infty}\psi_j(\boldsymbol{r})p_j^{\varepsilon}(t)\ . \tag{3.5}$$

.

Pisoni et al. (1995) show, that modal coordinates corresponding respectively to strain and displacement can be set equal. Then (3.5) becomes

$$\boldsymbol{\varepsilon}(\boldsymbol{r},t) = \sum_{j=1}^{\infty}\boldsymbol{\psi}_j(\boldsymbol{r})p_j(t)\ . \tag{3.6}$$

If the position vector $\boldsymbol{r}_m$ indicates the strain tensors at positions of the strain gauges, (3.6) becomes

$$\boldsymbol{\varepsilon}(\boldsymbol{r}_m, t) = \sum_{j=1}^{\infty} \boldsymbol{\psi}_j(\boldsymbol{r}_m) p_j(t)\,. \tag{3.7}$$

The components (k, l) of the strain eigenvector tensor, $\boldsymbol{\psi}_j(\boldsymbol{r}_m)$, can be used to determine the strain tensor, $\varepsilon_{kl}(\boldsymbol{r}_m, t)$, at the position indicated by $\boldsymbol{r}_m$ with the relationship

$$\varepsilon_{kl}(\boldsymbol{r}_m, t) = \sum_{j=1}^{\infty} \psi_{jkl}(\boldsymbol{r}_m) p_j(t), \tag{3.8}$$

where $\psi_{jkl}(\boldsymbol{r}_m)$ is component (k, l) of the strain eigenvector tensor $\boldsymbol{\psi}_j(\boldsymbol{r}_m)$.

The three strain gauge bridges measured only strains in normal directions. Therefore in this chapter only the normal strains are considered and therefore only those components for which $k = l$, i.e. those on the diagonal of the strain tensor $\varepsilon(\boldsymbol{r}_m, t)$. For a specific strain gauge with orientation along DOF d, the strain measurement output would be

$$\varepsilon_d = \sum_{j=1}^{3} \left(\frac{\partial \phi_{jd}}{\partial x_d}\right) p_j(t) = \varepsilon_{kl} = \sum_{j=1}^{3} \psi_{jkl} p_j(t), \tag{3.9}$$

with $(d, k, l) \in \{(x, 1,1), (y, 2,2), (z, 3,3)\}$.

where x, y and z represent the three translation DOFs at that point. Therefore $\boldsymbol{\psi}_{jd}(\boldsymbol{r})$ is denoted as a vector consisting of the diagonal entries of the strain eigenvector tensor $\boldsymbol{\psi}_j(\boldsymbol{r})$ for mode j with j running to 3 only, i.e. for the first three modes considered. Each entry of $\boldsymbol{\psi}_{jd}(\boldsymbol{r})$ is associated with a translation DOF. Here $\boldsymbol{\Psi}_D$ is then denoted as a matrix with the vectors $\boldsymbol{\psi}_{jd}$ as columns, where each element of $\boldsymbol{\psi}_{jd}$ is associated with one of the DOFs of the structure.

State space model (3.2) then becomes

$$\begin{Bmatrix} \dot{\boldsymbol{p}} \\ \ddot{\boldsymbol{p}} \end{Bmatrix} = \begin{bmatrix} \boldsymbol{0} & \boldsymbol{I} \\ -\boldsymbol{\Omega}^2 & -\boldsymbol{\Gamma} \end{bmatrix} \begin{Bmatrix} \boldsymbol{p} \\ \dot{\boldsymbol{p}} \end{Bmatrix} + \begin{bmatrix} \boldsymbol{0} \\ \boldsymbol{\Phi}^T \boldsymbol{b} \end{bmatrix} \{\boldsymbol{f}_{S1}(t)\} \tag{3.10a}$$

$$\{\boldsymbol{\varepsilon}_{S2}(t)\} = [\boldsymbol{c}\boldsymbol{\Psi}_D \quad \boldsymbol{0}] \begin{Bmatrix} \boldsymbol{p} \\ \dot{\boldsymbol{p}} \end{Bmatrix} \tag{3.10b}$$

which is of the form

$$\{\dot{\boldsymbol{z}}(t)\} = \boldsymbol{A}\{\boldsymbol{z}(t)\} + \boldsymbol{B}\{\boldsymbol{f}(t)\} \tag{3.11a}$$

$$\{\boldsymbol{\varepsilon}(t)\} = \boldsymbol{C}\{\boldsymbol{z}(t)\}, \tag{3.11b}$$

where

$$\{\boldsymbol{z}(t)\} = \begin{Bmatrix} \boldsymbol{p} \\ \dot{\boldsymbol{p}} \end{Bmatrix} \tag{3.12}$$

(3.10) can be written in Laplace domain as

$$\boldsymbol{E}_{S2}(s) = [\boldsymbol{C}(s\boldsymbol{I} - \boldsymbol{A})^{-1}\boldsymbol{B}]\boldsymbol{F}_{S1}(s) = \boldsymbol{H}(s)\boldsymbol{F}_{S1}(s) \tag{3.13}$$

High frequency effects were added to the entries of rational matrix $\boldsymbol{H}(s)$ in terms of zeros at $s = -20000$ and $s = -25000$ in order to make them bi-proper. This was necessary to obtain a transmissibility matrix $\boldsymbol{D} \neq \boldsymbol{0}$ for $s \to \infty$ (Skogestad & Postlethwaite, 2001:5). Following this modification a state space realization was obtained from the modified rational matrix $\boldsymbol{H}_n(s)$ aided by the Control System Toolbox from MATLAB (2003a). From the resulting state space realization an inverse realization was obtained as the quadruple

$$\begin{bmatrix} \boldsymbol{A}_n & \boldsymbol{B}_n \\ \boldsymbol{C}_n & \boldsymbol{D}_n \end{bmatrix} = \begin{bmatrix} \boldsymbol{A} - \boldsymbol{B}\boldsymbol{D}^{-1}\boldsymbol{C} & \boldsymbol{B}\boldsymbol{D}^{-1} \\ -\boldsymbol{D}^{-1}\boldsymbol{C} & \boldsymbol{D}^{-1} \end{bmatrix} \tag{3.14}$$

Along with

$$\boldsymbol{F}_D(s) = \boldsymbol{F}_{S1}(s) = [\boldsymbol{C}_n(s\boldsymbol{I} - \boldsymbol{A}_n)^{-1}\boldsymbol{B}_n + \boldsymbol{D}_n]\boldsymbol{E}_{S2}(s) = \boldsymbol{G}(s)\boldsymbol{E}_{S2}(s) \tag{3.15}$$

the dynamic forces at the tool tip can now be determined from the corresponding measured elastic force components. These dynamic force signals were then converted into strain sensed by the SSA, $\boldsymbol{u}_{2z}$. This conversion was done by means of a frequency domain filter, which was determined similarly to the IIR filters in chapter 2, and based on the structure dynamical properties obtained from an MD Patran model in Figure 3.2 of the tool holder also shown in Figure 3.1.

(3.3) requires that partial derivatives, specifically directional derivatives in 3 dimensions be computed numerically. For this purpose the software FreeFEM3D from Del Pino & Pironneau (2008) was utilized. The input files for FreeFEM3D had to contain geometry information of the tool holder, which originated from the MD Patran model of the tool holder shown in Figure 3.3 and its model in Figure 3.4. These input files were generated with the aid of custom made m-files from MATLAB (2003b) as well as gmsh software from Geuzaine &

Remacle (2009). Visualization of the geometry information contained in the input files was possible through Medit software from Frey (2001).

3.3. DATA ACQUISITION

3.3.1. Experimental set-up

A turning experiment was conducted to measure the three components of a cutting force using the type of tool holder shown in Figure 3.2 and instrumented with strain gauges as was mentioned in section 3.2.1. These signals were acquired such that they could be used to compare conventional strain gauge based TCM by sensing the cutting force components with TCM based on sensing of a single SSA signal. A schematic diagram of the experimental set-up is shown in Figure 3.4. The equipment used for the work of this chapter is listed in Table 3.1.

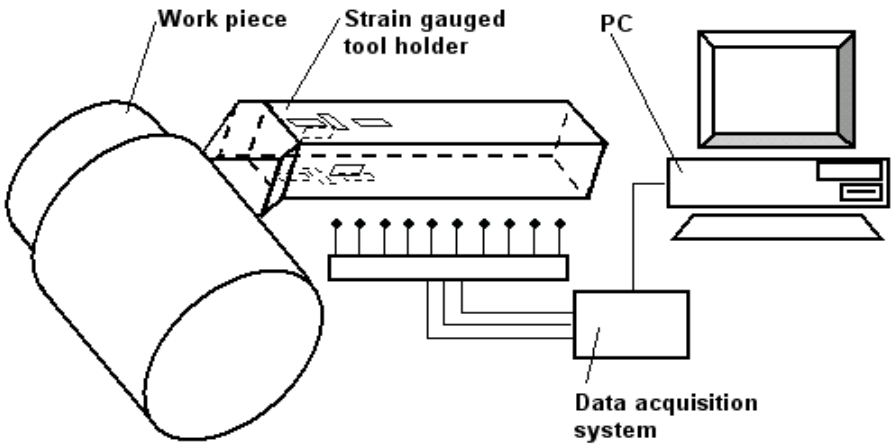

Figure 3.7: Experimental set-up

Pre-cutting was done with a 0.4 mm nose radius for the insert, however a larger radius, in this case 0.8 mm, was selected here so that the tool would vibrate with larger amplitudes and consequently better exploit the resolution capabilities of the acquisition system's range setting.

Table 3.1: Experimental equipment

Machine, tools and work piece	
Lathe	Colchester Student 1800 (manually operated)
Tool holder	SECO PTJNR-2020-16A
Insert	Mitsubishi TNGG 160408R – Carbide UTi20T
Work piece material and properties	EN19 oil-quenched, tempered to T-condition, same batch, 269-285 BHN hardness, 900-965 MPa UTS
Work piece dimensions	Ø 100 to 89 mm × Length 500 mm
Work piece surface	Pre-cutting with 0.4 mm nose radius inserts and 0.25 to 0.28 mm/rev feed rate

Instrumentation	
Feed force sensing	HBM strain gauge, 3/120ALY41, half-bridge
Tangential force sensing	HBM strain gauge, 3/120ALY41, half-bridge
Thrust force sensing	HBM 90º rosette strain gauge, 1-XY31-6/120, full-bridge
Flank wear measurement	Kyowa microscope, magnification: 40, 26 µm accuracy
Data acquisition system	eDAQ lite by SOMAT
Anti-aliasing	eDAQ built-in 6667 Hz linear phase LP filter
Data storage	PC, Pentium 4, with SOMAT test control environment (TCE) and Infield software

3.3.2. Experimental procedure

The experiment was designed in the finish cutting range based on Mitsubishi (2007:A042) so that measurements could be taken and monitoring done at different machining conditions, consisting of all possible combinations of the following settings for cutting speed (CS) in m/min, depth of cut (DOC) in mm and feed rate (FR) mm/rev:

$$\left.\begin{array}{c} CS_i \in \{128.8, 119.8, 114.6\} \\ DOC_i \in \{1.2, 1.4, 1.6\} \\ FR_i \in \{0.1, 0.16, 0.2\} \end{array}\right\} \quad for \;\; i = 1, 2, 3$$

The selection of the specific insert and these particular cutting parameters was influenced by a number of requirements, which had to be met. They were

i. observable progression of flank wear, hence the choice of a uncoated carbide insert
ii. fast tool wear, in order to speed up experiment and reduce the number of work pieces needed
iii. cutting forces should cause measurable deflection of tool holder

iv. the selected values of the cutting parameter should have sufficient spread to give statistical confidence for a model derived from quadratic regression mentioned in a section about the accuracy of the TCM systems.

The influences of the insert type on chip formation and also its resulting effect on cutting force is not the object of this chapter's study. The same insert types were used in the cutting process from which the cutting force signals used for this study originated.

Chen et al. (1993) describe how the state of the work piece surface before cutting, critically influences the cutting forces. Therefore the work pieces were pre-cut to keep their surface condition approximately constant.

The discrete measurements included the diameter of the work piece before and after a pass, the axial length, the duration of each pass and the photographic capture of insert flank wear. Flank wear is the deteriorating condition of the tool insert on its flank. The flank is that side of the tool insert's nose facing the feed direction during cutting. True values for CS and DOC could then be determined for every pass. The true FR of the lathe was determined by means of a dial gauge to 0.01 mm/rev accuracy. Flank wear was measured from the photographs as $VB = {}^{A}/_{L}$, where VB is the flank wear in mm and A is the area of the major flank wear, including the area of the primary groove (see Figure 3.8).

The variable error of each flank wear measurement is between -0.0006 and $+0.0006\,mm$ - this error can be different for each VB-measurement and is based on accuracy of the ruler used to do the measurements. The constant, i.e. the consistent error is between -0.026 and $+0.026\,mm$ – this error is the same for all VB-measurements and is based on the microscope accuracy.

Continuous measurements comprised the acquisition of three signals from a strain-gauged tool holder by a data acquisition system at a sampling frequency of $20\,kHz$. The instrumentation of the tool holder was designed so that it could sense bending by tangential and feed forces and also the longitudinal deformation caused by the thrust force.

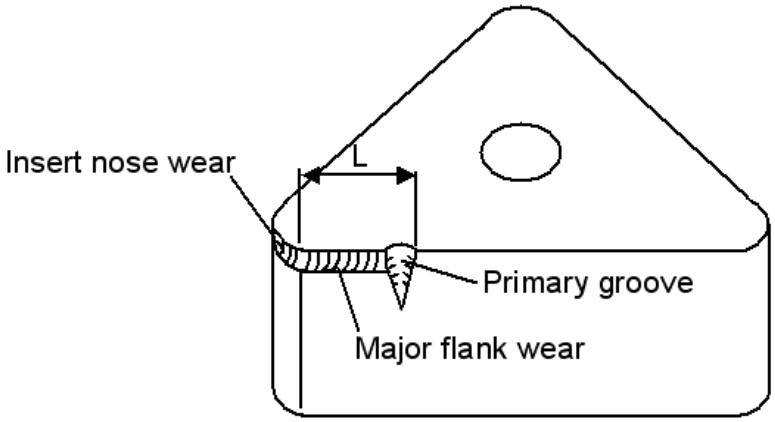

Figure 3.8: Measurement of flank wear

A calibration matrix $\boldsymbol{A}$ was determined to uncouple the interaction between the actual forces and the measured signals on each channel by means of transformation of coordinates.

The coefficients a_{ij} of this matrix are the ratios of voltages $v_i,\ i \in [1,2,3]$ measured at each of the three channels of the strain gauge instrumented tool holder to a force f_j applied in one of the three directions (tangential, feed and thrust) at the tool tip, while $f_l = 0$ with $l \neq j$ and $j,l \in [x,y,z]$ i.e. $a_{ij} = \frac{v_i}{f_j}$. Each a_{ij} was averaged over three sets of force and voltage values.

Post-processing of the signals consisted of multiplication of the inverse calibration matrix in order to obtain the three orthogonal force components from the three voltage signals, i.e. at time instant k,

$$\boldsymbol{f}_k = \boldsymbol{A}^{-1}\boldsymbol{v}_k\ , \tag{3.16}$$

where $\boldsymbol{f}_k = [f_{x_k} \quad f_{y_k} \quad f_{z_k}]^T$ and $\boldsymbol{v}_k = [v_{1_k} \quad v_{2_k} \quad v_{3_k}]^T$.

With (3.16) the inputs for the orthogonal TCM system were produced. The following signal conditioning however had to be done to obtain the inputs to the unidirectional TCM system. As inputs to the model in (3.15), the true strain values at selected nodes, with the dynamic force components at the tool tip as outputs, had to be obtained. These nodes were selected to coincide with SG1, SG2 and SG3 in Figure 3.3.

Two types of causes of combined loads on strain gauges were considered. One of them results in strain gauges measuring combined loads such as SG1 and SG2 in Figure 3.3. They sense strain due to bending around the y- and x-axis respectively and are also affected by the axial load along the z-axis. However the second cause of combined load sensing is due to alignment errors of the individual strain gauges on the tool holder. Such errors occur where a half bridge, which was designed to sense only bending around a certain axis, is to some degree also sensitive to bending around another axis or to axial thrust. The effect of thrust on half bridges, which are by design bending moment-sensitive, has been accounted for. The strain sensed by SG1, SG2 and SG3 due to alignment errors was less than 5.4 % of the designed sensitivity and was therefore neglected. To obtain true strain values the signals acquired by the data acquisition system via the strain gauge bridges were converted to strain at the particular nodes as follows. The strain gauge bridge equation is

$$\frac{v_{o_k}}{v_s} = \frac{k_g}{4}\left(\varepsilon_{1_k} - \varepsilon_{2_k} + \varepsilon_{3_k} - \varepsilon_{4_k}\right) \tag{3.17}$$

where v_{o_k} and v_s are the bridge output and supply voltages respectively and k_g is the gauge factor of the gauge type used for a particular bridge. The full bridge was used to measure thrust and was configured such that $\varepsilon_{2_k} = \varepsilon_{4_k} = \nu\varepsilon_{z_k}$ and $\varepsilon_{1_k} = \varepsilon_{3_k} = -\varepsilon_{z_k}$, where $\nu = 0.3$ was used as the Poisson's ratio with the convention that strains due to compression and elongation are negative and positive respectively. The half bridge was used to measure bending around the x- and y-axis respectively and was configured such that $\varepsilon_{3_k} = \varepsilon_{4_k} = 0$, $\varepsilon_{1_k} = \varepsilon_{z_k}$ and $\varepsilon_{2_k} = -\varepsilon_{z_k}$. Since the signal measured by the data acquisition system was

$$\varepsilon_{bi_k} = \varepsilon_{1_k} - \varepsilon_{2_k} + \varepsilon_{3_k} - \varepsilon_{4_k} \quad for \quad i = 1, 2, 3 \tag{3.18}$$

for the two half bridges measuring bending around the y- and x- axis and the full bridge respectively in $[\mu\varepsilon]$. The strains at the three nodes selected for computation of the dynamic force at the tool tip therefore were

$$\varepsilon_{SG3_k} = \left(\frac{1}{2(1+\nu)}\varepsilon_{b3_k}\right)\nu \tag{3.19a}$$

$$\varepsilon_{SG1_k} = 0.5\varepsilon_{b1_k} - \varepsilon_{SG3_k}\left(\frac{1}{\nu}\right) \quad \text{and} \tag{3.19b}$$

$$\varepsilon_{SG2_k} = 0.5\varepsilon_{b2_k} - \varepsilon_{SG3_k}\left(\frac{1}{\nu}\right) \tag{3.19c}$$

3.4. WAVELET PACKET BASED FEATURES

3.4.1. Wavelet transform

Tool wear sensitive features had to be found for training and test purposes of the neural network based tool wear monitoring methods. Initially signal properties such as the mean values to indicate the static cutting force and the mean energy in a frequency band were used as signal features. The latter was determined to indicate the energy of cutting force received by the tool holder within a specified frequency band. Other tested features were root mean square to indicate general vibration energy in the signal, and the crest factor to indicate an increase in signal peak values in relation to general vibration energy. Given the limited amount of neural network training data available and the weak correlation of abovementioned features with tool wear it was decided to use a systematic analysis such as wavelet packet analysis to recover wear sensitive features. This decision was also taken against the background of results obtained by Pal et al. (2011).

A wavelet transform is an integral transform with the integrands being the signal and the mother wavelet function or shifted and scaled versions of the latter. Including the mother wavelet function, these are all wave forms. Changes in scale and time shift respectively result in dilation and translation of the wavelet function as described in Wu et al. (1996). The wavelet function therefore has the prescribed property of localization in both time and frequency together with the smoothness property giving them the ability to convey essential information of the signal without noise.

Wavelet transforms have an analysing function of finite extent, which is one reason for its time localization property and this makes it suitable to capture features of non-stationary signals such as cutting forces in turning processes. In this chapter's study however the wavelet packet transform where each packet is a particular linear combination of their parent wavelet, is used.

3.4.2. Wavelet packet analysis

In wavelet analysis the signal is passed through two complementary filters, G and H, splitting it into two signals. The low-pass filter H yields one signal with low frequency components known as an approximation coefficient vector. The high-pass filter G yields the other signal with high frequency components known as detail coefficient vector. In Wavelet analysis this process of regarding the coefficient sequences as signals and splitting them as mentioned above is continued only on the approximation coefficient sequences.

In wavelet packet analysis however both approximation and detail are split in a recurring way, again each into approximation and detail. This is known as decomposition of the signal. The wavelet functions at each level of decomposition have an increased degree of dilation also known as increased scale.

Each wavelet packet is part of a family of packets, e.g. Daubechies 1 to 15, Symmlets 2 to 8 and Coiflet 1 to 5 families, and forms an orthonormal basis of the parent wavelet as shown by Wickerhauser (1994:242). Using the notation of Wickerhauser (1994:245), the set of functions $\{W_{jn}(k): k \in \mathbb{Z}\}$ consists of the inner products of a function $x = x(t)$ square integrable, which is, in the case of this chapter's study, the signal to be processed, with the base functions ϕ_{jnk} and is defined as

$$W_{jn}(k) \stackrel{\text{def}}{=} \langle x, \phi_{jnk} \rangle = \int_{\mathbb{R}} \bar{x}(t) 2^{-j/2} \phi_n\left(2^{-j}t - k\right) dt \tag{3.20}$$

where $\bar{x}(t)$ is the complex conjugate of $x(t)$.

Here the three-indexed analysing functions, which are a family of wave forms, are

$$\phi_{j,n,k}(t) = 2^{-j/2} \phi_n(2^{-j}t - k), \quad n \in \mathbb{N} \text{ and } (j,k) \in \mathbb{Z}^2 \tag{3.21}$$

Index k can be interpreted as the time localization parameter, index $j$as the scale parameter and n the frequency index.

By proven lemma in Wickerhauser (1994:245) it can be said that the coefficient sequences $\{W_{jn}\}$ are then decomposed to the next level $j+1$ and satisfy the recursion relations

$$W_{j+1,2n}(k) = HW_{jn}(k) \tag{3.22}$$

and

$$W_{j+1,2n+1}(k) = GW_{jn}(k) \tag{3.23}$$

If the wavelet packet decomposition is organized in a tree with the set of functions $W_{jn} = \{W_{jnk}(x): k \in \mathbb{Z}\}$ representing the (j,n) wavelet packet, the tree will be as shown in Figure 3.9, where $W_{0,0}$ and $W_{1,1}$ are defined by the scaling function φ and the wavelet function ψ respectively as

$$W_{0,0} = \{\varphi(x-k), k \in \mathbb{Z}\} \tag{3.24}$$

and

$$W_{1,1} = \left\{\psi\left(\frac{x}{2} - k\right), k \in \mathbb{Z}\right\}. \tag{3.25}$$

One-dimensional wavelet analysis, such as in this application, is based on one scaling function φ and one wavelet function ψ, also called the parent wavelets. The Daubechies 1 to 15, Symmlets 2 to 8 and Coiflet 1 to 5 families of parent wavelets as used in the study in this chapter, each have their particular scaling function and wavelet function. Decomposition of the signal to be analysed was done to a certain level starting with a single parent wavelet, e.g. Symmlets 3 at the top level and then dilated and translated, i.e. shifted versions of it at the successive levels.

Interpreted this means that the function space V_o (in which lies the signal, $x(t)$, to be analysed) is spanned by the family, $W_{0,0}$. Each subspace spanned by $W_{j,n}$ is further split or decomposed into subspaces spanned by $W_{j+1,2n}$ and $W_{j+1,2n+1}$ respectively. Such decomposition is organized in the tree mentioned above. The wavelet packet analysis in this study was aided by the Wavelet Toolbox from MATLAB (2006a).

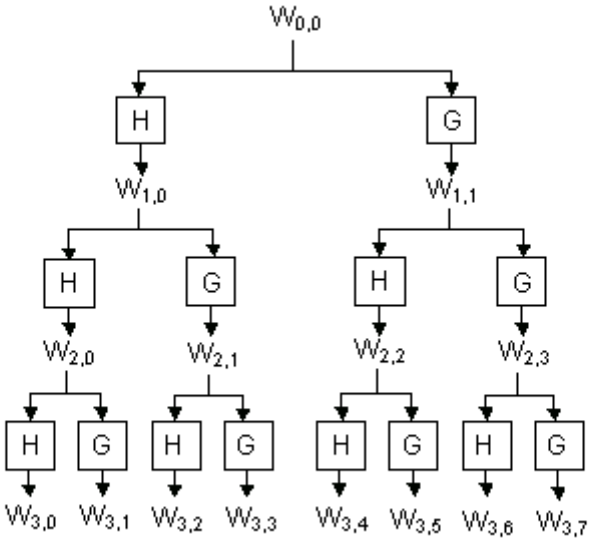

Figure 3.9: Wavelet packet tree

Different criteria are available to determine the depth of decomposition in the tree. The entropy criterion was used here because it is commonly used in signal processing applications MATLAB (2006h). The maximum depth for which the entropy of more than 50 % of the children coefficient sequences of a certain level is less than their corresponding parent sequence was chosen as the level or depth of decomposition.

The Shannon entropy relationship

$$E(S) = -\sum_{k=1}^{N} S_k^2 log\left(S_k^2\right) \tag{3.26}$$

was used here to determine the entropy of a signal S.

The coefficient sequences of each level of Figure 3.9 each represent a frequency sub-band. If the original signal was sampled at $F_s = 20kHz$ with a usable frequency $\frac{F_s}{2} = 10kHz$ then in level $j = 3$ there are 2^j sub-bands of equal width.

3.4.3. Feature selection

The decomposition level depends on the type of parent wavelet and the signal, i.e. tangential, feed or thrust force signal or the SSA strain signal. The signal was decomposed into a number of coefficient sequences representing abovementioned sub-bands. Coefficients for the detail of the decomposed signal are smaller than those of the approximation part, which represents the lower frequency sub-bands. Energy values of frequency sub-bands were considered for the removal of noise. The root-mean-square (RMS) values of each sub-band's coefficient vector were taken as a measure of that particular sub-band's energy. Frequency bands, which together had an energy sum below a threshold of 2 % were discarded. This method of noise removal can be regarded as a type of threshold technique.

For TCM based on a strain-gauge instrumented tool holder the features are classified according to three degrees of freedom, namely the signal of a particular force component, the wavelet type and sub-band energy number. Regarding the TCM based on a SSA, features are classified according to only two degrees of freedom, namely the wavelet type and sub-band energy number. For the purpose of TCM the most wear sensitive features were selected as in Scheffer & Heyns (2004) by correlation using

$$\rho = \frac{\sum_i (V_{Bi} - \bar{V}_B)(\theta_{ni} - \bar{\theta}_n)}{\sqrt{\sum_i (V_{Bi} - \bar{V}_B)^2 \sum_i (\theta_{ni} - \bar{\theta}_n)^2}} \quad , \tag{3.27}$$

with V_{Bi} and θ_{ni} being flank wear and the corresponding n'th feature at the i'th instant of measurement. Since the feature space is here defined by a component of the wavelet type and also the frequency sub-band component, the selection of a certain correlating feature would then determine by which wavelet and sub-band it is described.

For strain gauge based TCM the following two features, each described by three degrees of freedom, have been selected.

1)	Force component	:tangential
	Wavelet type	:Symmlets 1
	Feature/Sub-band/Decomposition level	: θ_{16}/2344 to 2500 Hz/ 6

2)	Force component	:feed
	Wavelet type	:Symmlets 8
	Feature/Sub-band/Decomposition level	: θ_1 / 0 to $156Hz$/ 6

For TCM based on a SSA the two features, each described by two degrees of freedom were selected as follows.

1)	Wavelet type	:Symmlets 4
	Feature/Sub-band/Decomposition level	:θ_1 / 0 to $312Hz$ / 5
2)	Wavelet type	:Daubechies 1
	Feature/Sub-band/Decomposition level	:θ_{40} / 6094 to $6250Hz$/6

3.5. DATA PROCESSING

3.5.1. Design of experiments

For the cutting parameters CS, DOC and FR, a full factorial design of experiment (DOE) was chosen, i.e. a number of $q = 3$ levels for each cutting parameter so that the total number of experiments for the design was $3^q = 27$. This means that for every set of three experiments, one parameter was adjusted to three different levels, while the other two were kept constant. The experiment was also conducted according to DOE in order to obtain data, which allow for training the neural networks with the influence of all the above-mentioned cutting parameters.

3.5.2. Neural networks

A NN-approach was used for the comparison of two ways of monitoring tool wear, because it has already successfully produced results that appeared in the literature and was mentioned in section 3.1. In the first, features are obtained from strain gauge based sensing of the orthogonal cutting force components. In the second, tool wear monitoring is based on features available from a single strain signal that would be experienced by the SSA due to the cutting force at the tip.

A network structure as depicted in Figure 3.10 was selected. This is based on a structure published by Sick (2002) and later also applied by Scheffer et al. (2003), and consists of a dynamic network (DN) with time-delayed inputs and a number of static networks (SN) corresponding to the number of features involved. All networks are of the feed-forward type with the first layer consisting of tan-sigmoid neurons to provide non-linear properties and the output layer of a linear transfer function to allow for a wide range of output values. The architecture choice of the DN and the SN are 5-1 and 5-1 respectively, resulting in 26 and 31 parameters for the DN and SN respectively.

The DN was trained online, using the Particle Swarm Optimisation Algorithm (PSOA) as in the work of Scheffer et al. (2003). In this algorithm a complete set of n network parameters (weights and biases) constitutes a multi-dimensional particle position, $\boldsymbol{w}$, at a given instant in time. A swarm size of 25 is considered. This is a value used in Scheffer et al. (2003) and it was also found that a larger swarm population, such as 40, did not improve the monitoring capabilities. The optimisation starts with the initialised space

$$D = \{\boldsymbol{w} \in \mathbb{R}^{\boldsymbol{n}} : -1 < w_i < 1,\ i = 1 \dots n\} \tag{3.28}$$

and considers the optimisation problem

$$min\ \ g_k(\boldsymbol{w}) = \sum_{\boldsymbol{j=1}}^{m} e_{jk} \tag{3.29}$$

where

$$e_{jk} = \sqrt{\left(\theta'_{jk} - \theta_{jk}\right)^2}\ ,\ j = 1 \dots m \tag{3.30}$$

with θ'_{jk} and θ_{jk} the j'th true and estimated signal features for a certain interval respectively at the k'th measuring instant.

The optimisation before each true time increment was performed for 40 pseudo time steps, τ. The algorithm is briefly described by the updating equations for velocity, $\hat{\boldsymbol{v}}$, of particle i at pseudo time step $\tau + 1$, namely:

$$\hat{\boldsymbol{v}}^i_{\tau+1} = q\hat{\boldsymbol{v}}^i_{\tau} + c_1 r_1\left(\boldsymbol{p}^i_{\tau} - \boldsymbol{w}^i_{\tau}\right) + c_2 r_2\left(\boldsymbol{p}^g_{\tau} - \boldsymbol{w}^i_{\tau}\right) \tag{3.31}$$

with $\boldsymbol{p}_\tau^i$ the best ever position of particle i at time τ and $\boldsymbol{p}_\tau^g$ the global best position in the swarm at time τ. In (3.31), r_1 and r_2 are random numbers chosen as

$$H = \{r_i \in \mathbb{R}:\ -1 < r_i < 1,\ \ i = 1,2\}, \tag{3.32}$$

and $c_1 = c_2 = 2$ in order to keep the mean gain of each term equal to 1. The inertia parameter, q, in (3.31) was initially set to 0.99 and then decreased linearly during optimisation. The updating equation for position, $\boldsymbol{w}$, is

$$\boldsymbol{w}_{\tau+1}^i = \boldsymbol{w}_\tau^i + \hat{\boldsymbol{v}}_{\tau+1}^i\ . \tag{3.33}$$

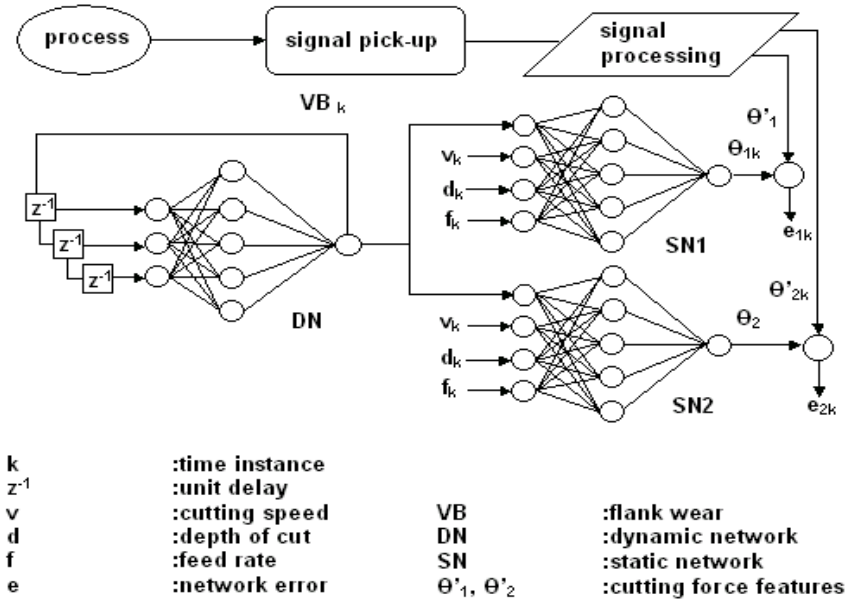

Figure 3.10: Monitoring with a time-delay neural network structure

Due to the design of the experiment as well as the factors influencing the process as mentioned in section 3.3.2., limited data was available to train the SNs. Consequently, SN-training was done by means of Bayesian Regularisation, using the Neural Network Toolbox of MATLAB (2003c), to improve generalisation and prevent over-fitting. In order to deal with the lack of training data an attempt was made to reduce the input space by applying principal component analysis (PCA) as described in Jackson (1991:10). However from the input space consisting of 27 entry vectors of the inputs CS, DOC and FR, none of the inputs could be discarded because each of them contributed at least 30% to the total variance of the

inputs. Discarding one of the cutting parameters could not perform a reduction of abovementioned input space. If the features are also seen as system inputs one cannot reduce the input space by discarding certain features because doing that one also has to discard SNs and this in turn will change the whole system.

The neural network structure including the number of parameters to be trained is the same for both TCM systems, i.e. the one based on processing of orthogonal force signals and the other, which is based on processing of unidirectional strain signal. Therefore the estimating speed of tool wear is the same for both. It is approximately 60 seconds per data point while the cutting time intervals between data points are above 180 seconds for the cutting conditions of this work. The data processing was done on a Pentium® 4 with 2.4 GHz CPU.

3.6. RESULTS

3.6.1. Quadratic regression

The response surfaces in Figure 3.11 show flank wear, VB, as a function of cutting parameters at 1296 seconds after commencement of cutting. These graphs can thus be used to predict VB at the given time instant and cutting parameters only. From the response surfaces in Figure 3.11 it is clear, that flank wear, VB, is nonlinearly related to cutting parameters and that flank wear is most sensitive to cutting speed, v.

A fully quadratic regression fit between flank wear and the three cutting parameters at 1296 seconds after commencement of cutting gives the relationship

$$VB = 0.2817 + 0.4588v - 0.0598d - 0.0250f - 1.8422vd \\ -0.0443vf + 0.1668df + 0.2301v^2 - 0.5064d^2 - 0.1288f^2 \quad (3.34)$$

where v, d and f are normalized values and are related to their true values according to:

$$w = (W - W_{mean}) \cdot \left(\frac{1}{(W_{max} - (W_{max} - W_{min})/2)}\right) \quad (3.35)$$

where w refers to the normalized values, W to the true values, and, W_{mean}, W_{max} and W_{min} to the mean , maximum and minimum values of W respectively.

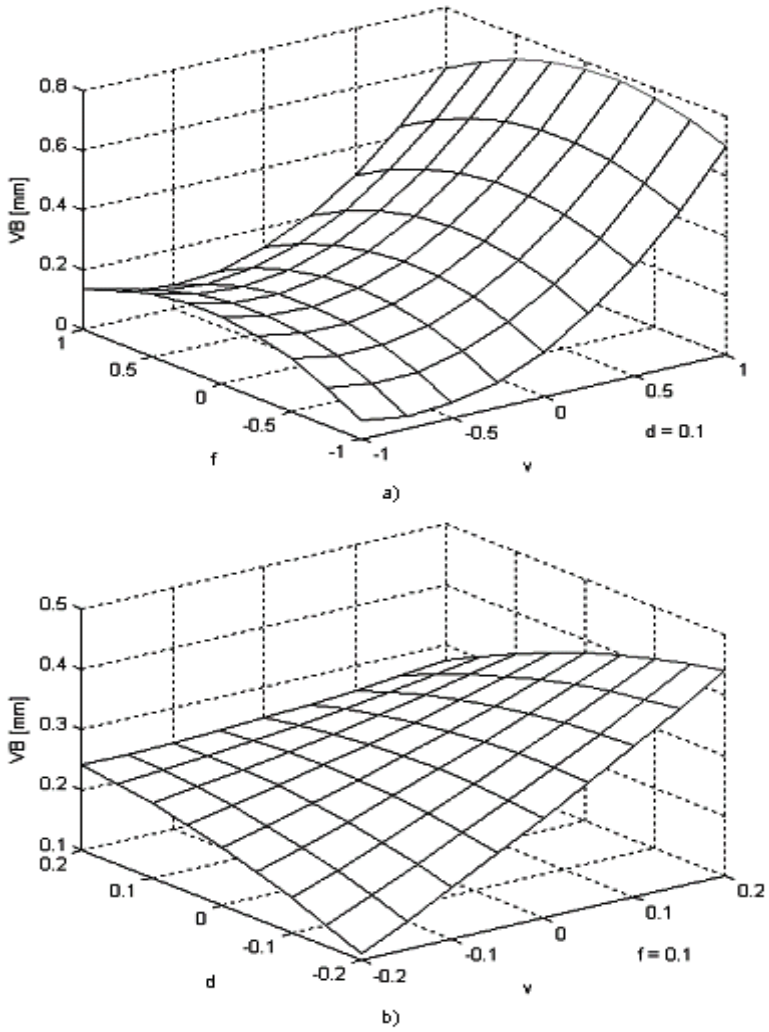

Figure 3.11: Response surfaces of flank wear, VB a) versus feed rate, f, and cutting speed, v, with depth of cut, d = 0.1, b) versus depth of cut, d, and cutting speed, v, with feed rate, f = 0.1.

3.6.2. Selection of training sets

From the 27 tool insert data sets, Q_i, with $i = 1, \ldots 27$ first a selection E_2 based on two criteria was used to determine the relative performance of the two TCM systems under consideration. These two criteria are described as follows.

1) The correlation coefficient of the features with tool wear on an insert should be larger than 0.85. Let the set which satisfies this criterion be called E_1, i.e.

$$E_1 = \{Q_i:\ \rho_i > 0.85,\quad i = 1, \dots 27\} \tag{3.36}$$

2) At least 4 of the data sets Q_i with $i = 1, \dots 27$, which are elements of E_1 should be part of the abovementioned selection with an approximately equal representation of each of the three speed settings:

$$E_2 = \left\{Q_i:\ P(A/E_1) \approx P(B/E_1) \approx P(C/E_1) \geq \frac{4}{27},\quad i = 1, \dots 27\right\} \tag{3.37}$$

where $P(J/K)$ means the probability of J given K and

$$A = \{Q_i:\ CS = 128.8\, m/min\},$$
$$B = \{Q_i:\ CS = 119.8\, m/min\},$$
$$C = \{Q_i:\ CS = 114.6\, m/min\}.$$

This criterion was included since for the ranges of cutting parameters used in the experiment described in this chapter, tool wear is more sensitive to changes in CS than to changes of any of the two other cutting parameters. This could be seen on the three-dimensional response surfaces of flank wear versus CS and FR and flank wear versus CS and DOC in Figure 3.11.

The selection of the training set can be illustrated in a Venn diagram as shown in Figure 3.12 with E_2 as a subset of E_1.

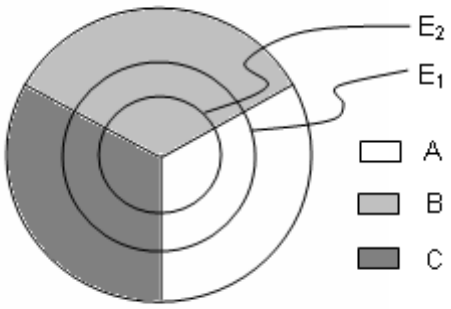

Figure 3.12: Venn diagram of selected training set

In order to increase the statistical confidence in the results of the relative performance of the two TCM systems a number of 9 out of 12 data sets, which were most sensitive to tool wear, were used for training and the remaining 3 sets, were used for testing of the TCM systems to be compared. Each experiment (i.e. each data set) provided 6 training input patterns corresponding to the 6 instances of flank wear measurement. Using 9 data sets each with 6 instances of measurement results in 54 input vectors each mapped to a target vector for training of the SNs.

3.6.3. Hypothesis test

In this hypothesis test the difference in mean errors $\delta\mu_{err}$ in the estimation of flank wear values between the two TCM systems are under consideration. The general requirement with respect to the TCM based on a linear combination of the orthogonal force components is that

$$\delta\mu_0 - l \leq \delta\mu_{err} \leq \delta\mu_0 + l, \text{ with } l = 0.05 \text{ and } \delta\mu_0 = 0 \tag{3.38}$$

The difference in mean errors is defined as

$$\delta\mu_{err} = \mu_{err\ SSA} - \mu_{err\ SG}\ , \tag{3.39}$$

where

$$\mu_{err\ SSA} = \frac{1}{N}\sum_{i=1}^{N}\left|V_{B\ true_i} - V_{B\ SSA_i}\right| \tag{3.40}$$

and

$$\mu_{err\ SG} = \frac{1}{N}\sum_{i=1}^{N}\left|V_{B\ true_i} - V_{B\ SG_i}\right|\ , \tag{3.41}$$

with N the number of measurements. Subscripts SSA and SG refer to the SSA – and the strain gauge-based TCM systems respectively for the remainder of this section.

The graph in Figure 3.13 shows the relative probability of $\{\delta\bar{x}_{err} : -1 < \delta\bar{x}_{err} < 1\}$ where $\delta\bar{x}_{err} = \delta\bar{x}_{err\ SSA} - \delta\bar{x}_{err\ SG}$. All $|\delta\bar{x}_{err}| \geq 1$ were regarded as outliers. It can be seen that the difference in sample means has a clear central tendency of $\delta\bar{x}_{err} \approx 0.0218$ but a high variance, which is expected to be the result of process uncertainties. Here $\bar{x}$ refers to the sample mean. Since the value of $\delta\bar{x}_{err} \approx 0.0049$ already falls in the required interval

specified in (3.38) it is further determined by hypothesis testing with what probability will it be found at the value $\delta\mu_1 = 0.0048$, i.e. close to $\delta\bar{x}_{err} \approx 0.0049$.

The hypothesis to be tested here is as follows. For the null-hypothesis to be true there should be no difference in the mean errors of flank wear estimation between the TCM systems, i.e.

$$H_0: \quad \delta\mu_{err} = \delta\mu_1 \tag{3.42a}$$

$$H_1: \quad \delta\mu_{err} \neq \delta\mu_1 \tag{3.42b}$$

with significance level of $\alpha = 0.95$, in order to keep the probability of a type II error β, for which $\beta \to 1 - \alpha$ if $\delta\mu_{err} \to \delta\mu_1$ as low as possible. A type II error occurs if H_0 is false and is not rejected but if H_1 which would then be true is wrongly rejected instead.

Generally it is not known on which side of zero $\delta\mu_{err}$ lies, a two-tailed test for the variable of differences between means $\delta\mu_{err}$, is therefore done. The test of the statement in (3.42) is based on the statistic

$$t_0 = \frac{\delta\bar{x}_{err} - \delta\mu_1}{S/\sqrt{n}} \tag{3.43}$$

where n is the sample size and S the standard deviation of the sample.

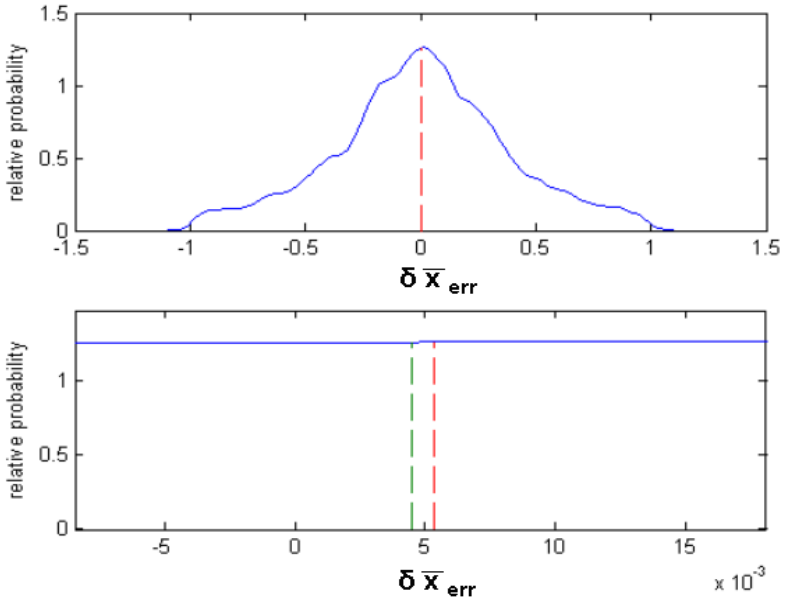

Figure 3.13: Subplot 1: Complete density of relative probability Subplot 2: Density of relative probability zoomed in on 5 % confidence interval.

For a sample of $n = 3310$ and $S = 0.383$, which result in $t_0 = 0.015$. With a significance level $\alpha = 0.95$ and using a t-distribution, the corresponding interval $[-t_{\alpha/2;n-1}, t_{\alpha/2;n-1}]$ is determined using the t-distribution calculator at Berman (2016) as $[-0.063,0.063]$. Since t_0 is bracketed by this interval H_0 is accepted.

The significance of having made an error with this acceptance is $\beta \approx 0.05$. This is the probability of a type II error, which would be the failure to reject H_0 if it is false. Therefore H_0 as formulated in (3.42) is accepted. This also satisfies the general requirement set in (3.38).

3.6.4. Accuracy of monitoring systems

This section is organized in two parts. The first one contains a description of the procedure by which the accuracy of abovementioned two systems was measured. The contents of the second part describe the room found to improve the accuracy of the two systems after they were trained using different standard deviations of error for tool wear data.

3.6.4.1. Current accuracy

The accuracy of these monitoring systems was tested by using any 24 from the total of 27 data sets for training of the networks. For the testing of the networks the remaining 3 data sets were used. The only condition to this selection was that each of the three cutting parameter settings would be represented an equal number of times in the data sets used for testing. Each data set contributed 6 measurement points and in neural network terminology 6 patterns. With 24 data sets therefore the input vectors, i.e. patterns, each mapped to a target vector for training of the SNs for estimation of the current accuracy of the monitoring systems amounted to 144.

The average accuracy of the remaining tool wear estimation expressed as the percentage of the error with respect to the measured values for tool wear for orthogonal TCM and unidirectional TCM is given in Table 3.2. The cutting parameter values given in section 3.3.2 correspond to the notation in Table 3.2.

Table 3.2 Flank wear error statistics

Data set/s for testing with 24 training data sets *	All combinations, that have all cutting parameter values represented in a test set consisting of 3 data sets		(CS_1, DOC_2, FR_2), (CS_2, DOC_1, FR_1), (CS_3, DOC_3, FR_3)	
TCM system	Orthogonal	Unidirectional	Orthogonal	Unidirectional
Std. deviation	0.23	0.248	0.194	0.258
Mean error μ_{err} : Current accuracy	32.0 %	33.3 %	31.3 %	36.7 %
Mean error μ_{err} : Improved accuracy	-	-	18.2 %	16.4 %

* Estimated data points of set D which were discarded (see text)

Human decision making may be incorporated in condition monitoring algorithms such as dealt with in Gajate, Haber, del Toro, Vega & Bustillo (2010). For the NN-algorithm as used in this chapter, decision-making can be avoided with the availability of a much larger number of training data sets. In Table 3.2 reasoning however is used to discard estimation errors greater than 100 %, since these could be an indication of insert breakage rather than expected wear. In the light of measured flank wear increments between consecutive measurement instants of between 1 % and 69 % this is a justifiable limit of exclusion. The category of insert breakage is beyond the scope of this chapter and is regarded as an error by the monitoring system rather than an estimation of expected flank wear. Therefore the estimated data points in set $D = \{\mu_{err} : -1 > \mu_{err} > 1\}$ have been discarded for the figures given in Table 3.2. However the absolute maximum and minimum values of estimated flank wear VB are shown in Figures 3.14 and 3.15 except for a 0.6 % of the data points which were regarded as outliers.

Figures 3.14 and 3.15 show the results for orthogonal and unidirectional TCM respectively for a test data set as specified in the right half in Table 3.2.

The range limits and standard deviation envelopes in Figures 3.14 and 3.15 were calculated from the population of 9 flank wear measurements at a particular measurement instance for each of the three cutting speed settings using MATLAB (2003d).

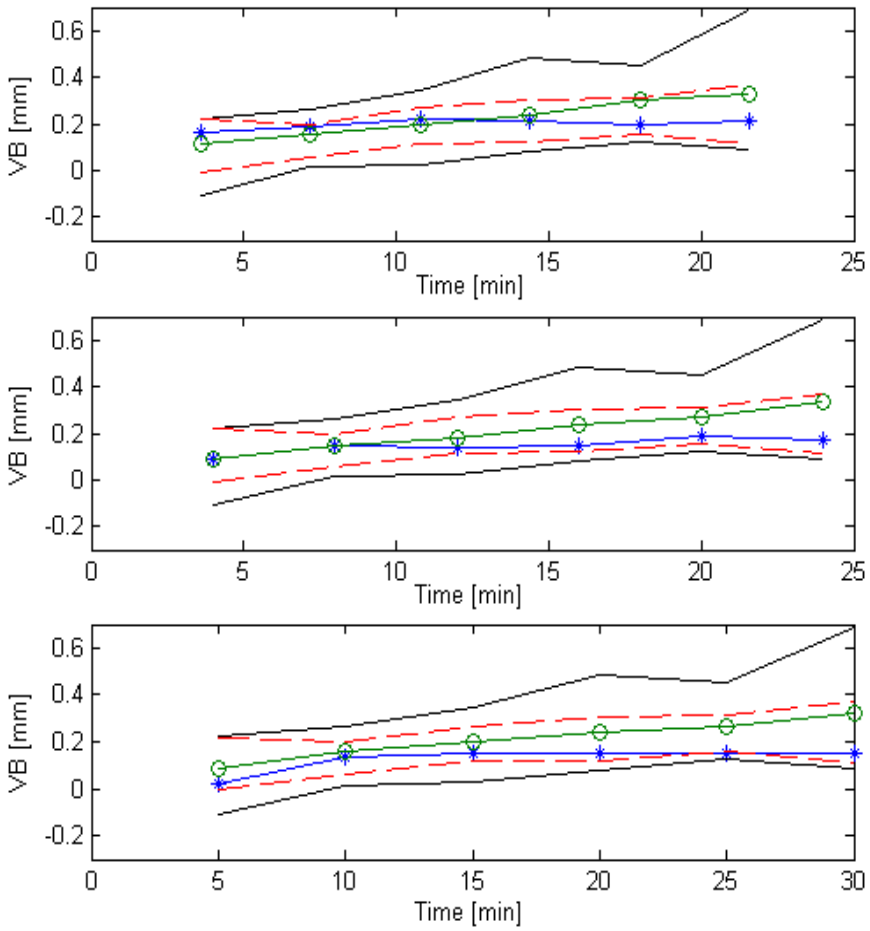

Figure 3.14: Estimated VB (*) compared with measured VB (o) using orthogonal TCM and standard deviation (dashed red) as well as range limits (solid black) of estimated VB.

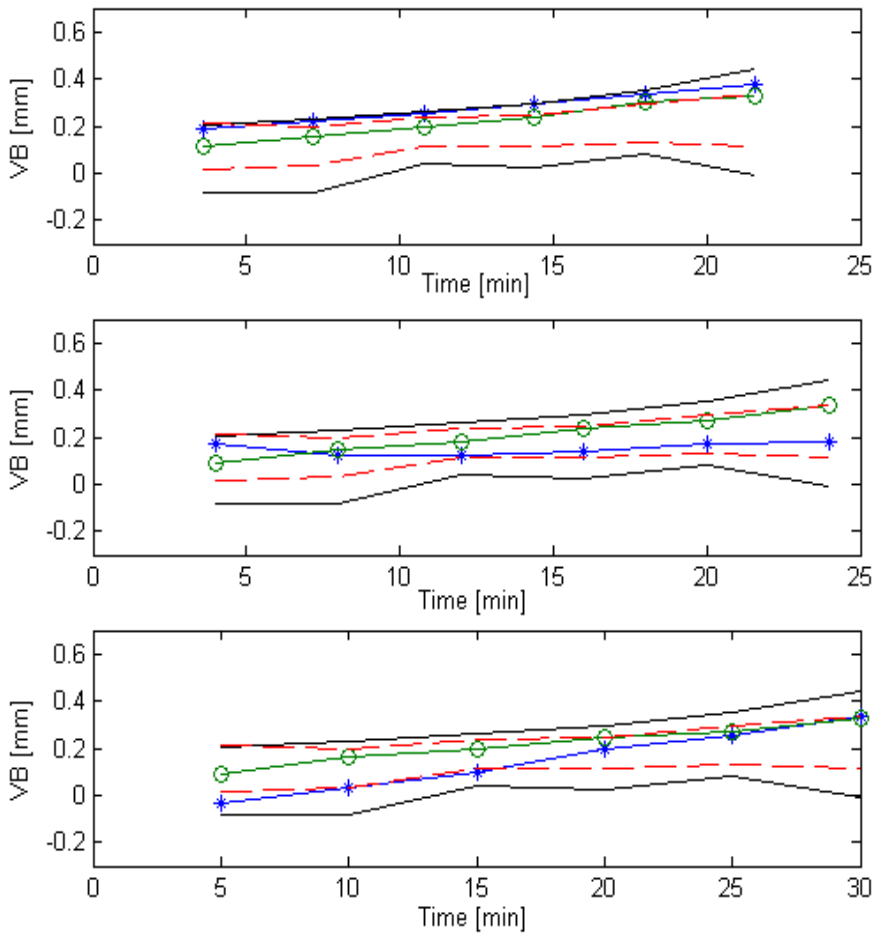

Figure 3.15: Estimated VB (*) compared with measured VB (o) using unidirectional TCM and standard deviation (dashed red) as well as range limits (solid black) of estimated VB.

Figure 3.16 shows the range of measurement errors of true flank wear with the range as well as true flank wear averaged over all 27 data sets. The average error VB_{err} due to ruler and photo contrast and resolution was measured by a microscopic photo scale as $|VB_{err}| < 0.0136\ mm$. If expressed as percentage of the corresponding true flank wear at the first and last of 6 measurement instances this error ranges between and 17.7 and 3.7 % . The accuracy of the microscope for the given magnification is specified in Table 3.1.

The results in Table 3.2 and Figures 3.14 and 3.15 must be interpreted against this background and that only a small number of input patterns were available for training of the static networks.

To get an impression about the improvement of accuracy of a multi-layer perceptron type of NN the interested reader is referred to Wang, Wang, Huang, Nguyen & Krishnakumar (2008). The next section shows what room there is to improve the accuracy of the NN used in this work without changing its structure.

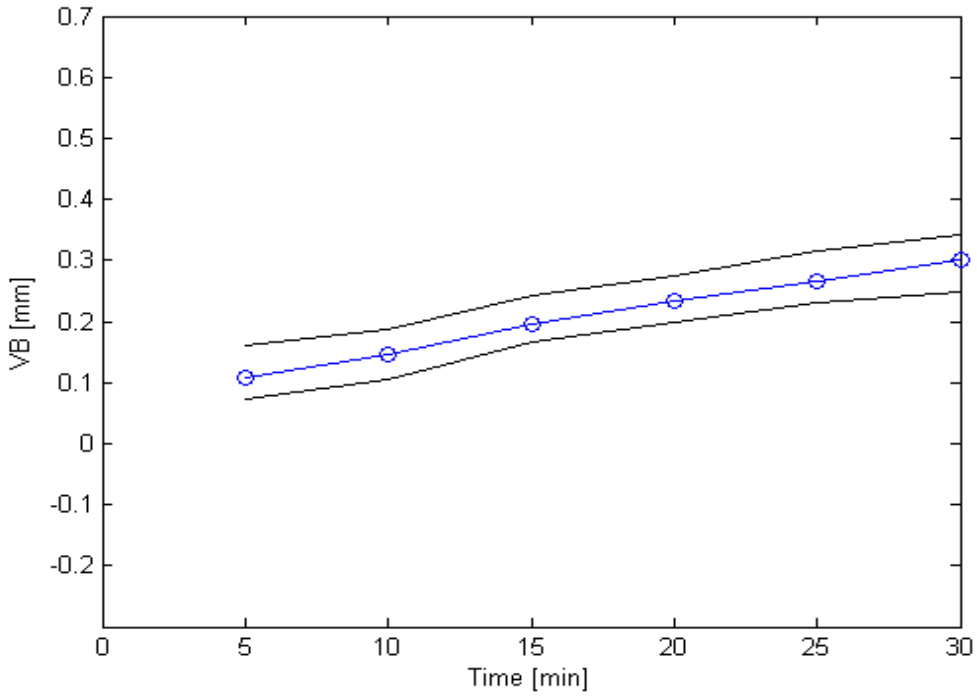

Figure 3.16: Range of measurement errors of true flank wear

3.6.4.2. Improved accuracy

Figure 3.17 shows the sensitivity of the monitoring systems. The points that the curve is fitted on are described by the graphs ordinate and abscissa. The ordinate represents the standard deviation of the error of the tool wear estimated by NNs. The abscissa in turn represents a standard deviation of the error of tool wear values which were used for training purposes of these NNs. A robust regression polynomial curve fit was performed on the points shown in Figure 3.17 (MATLAB, 2003d). The reason for this was that the fitting method should have

robustness with respect to outliers. The cutting parameter settings of the training and test sets that were used to find the improved accuracy were the same as was used to find the current accuracy of the two systems described in the section 3.6.4.1. However the reference values for tool wear used here were determined by means of models, which in turn were obtained through full quadratic regression as described in section 3.6.1 at 6 linearly spaced time instances of the cutting process from $t = 300$ to 1296 seconds. The tool wear data for this regression fit was obtained by linearly interpolating the tool wear values for each cutting parameter setting at abovementioned time instances. The resulting 6 models then yielded the tool wear reference values as functions of the three cutting parameters, CS, DOC and FR. The coefficients for these relationships are given in Appendix C.

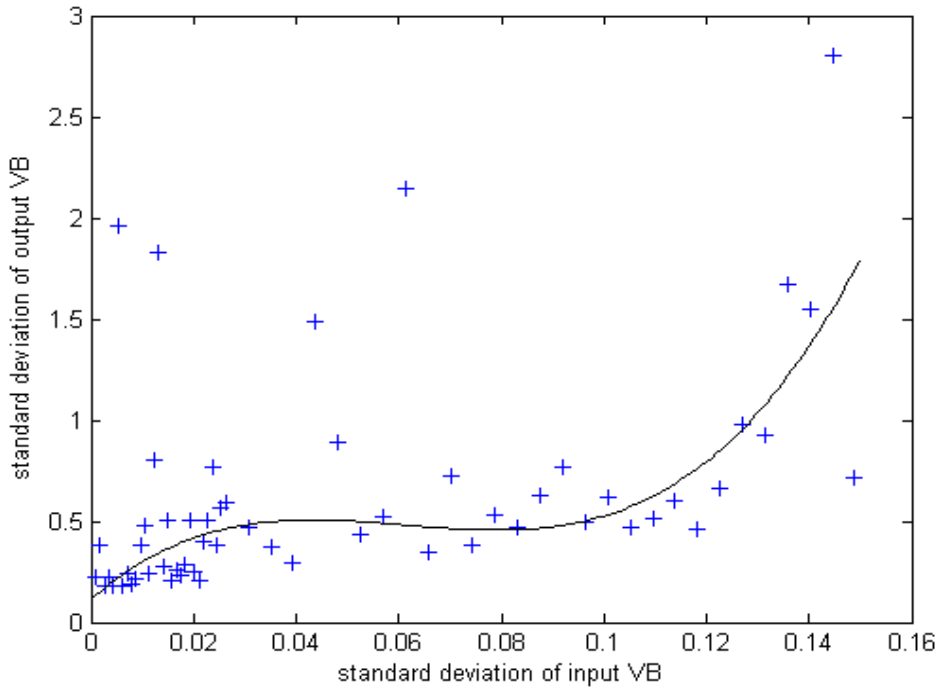

Figure 3.17: Standard deviation of estimated (output) VB values versus standard deviation of VB values used for training purposes (input) determined with 3rd order robust regression fit .

Figure 3.17 shows that a reduction of standard deviation on the error of the input training data from $S_{VBerr\ tr} = 0.015$ down to zero would result in a standard deviation of as low as $S_{VBerr\ est} = 0.114$ in the error of tool wear estimation at the output side of system 1 and system 2 instead of the $S_{VBerr\ est} = 0.22$ and 0.33 before such a reduction. A $S_{VBerr\ est} = 0.114$ due to abovementioned reduction of error standard deviations in input training tool

wear data would then correspond to an average tool wear estimation error of 18.2 % and 16.4 % for orthogonal TCM and unidirectional TCM respectively. These percentages may be improved even further by using data, which corresponds to at least twice as many patterns for training of the networks and improved noise reduction in the signals sensed from the cutting process.

3.7. CONCLUSION

Cutting-force measurements were used to investigate whether it would be feasible to utilise a signal, which is a linear combination of the orthogonal force components at the tool tip. The feedback signal, which a semi-embedded self-sensing actuator provides in an active vibration control system, was mentioned as specific case where this signal would be used for condition-monitoring purposes. A derivation of the models linking strain to dynamic force on the specific tool holder, which was used for this study, was therefore given.

Under manual machining conditions with non-stationary cutting force signals a wavelet packet analysis was followed to generate tool wear sensitive features of the signals to be used in the two different monitoring systems under consideration. One system was based on the processing of orthogonal force components and the other on the processing of a linear combination of these components.

A loss of accuracy for TCM based on a unidirectional sensed signal as compared to the orthogonal reference case would have been plausible. However a hypothesis t-test showed that the probability of a difference of flank wear estimation error by less than 5 percentage points for these two monitoring systems is 0.95 when using a time-delayed neural network algorithm. Based on information about the sensitivity of the standard deviation of tool wear estimation error versus the standard deviation of the tool wear error for network training an accuracy of the two monitoring systems can be indicated. It is indicated as 18.2 % and 16.4 % for the TCM system based on processing of orthogonal force components and the TCM system based on the processing of unidirectional strain respectively. This justifies further research into tool condition monitoring using signals, which are a linear combination of the orthogonal components sensed as in the specific application described in this study.

The strain-gauge based orthogonal TCM may be the easier option to implement. However it was shown that unidirectional piezoelectric transducer based TCM could be an added benefit to the use of an SSA in tool vibration control.

CHAPTER 4

ACTIVE CONTROL OF TOOL VIBRATIONS USING A SELF-SENSING ACTUATOR

4.1. INTRODUCTION

The second and third chapters dealt with the viability of exploiting the actuating and sensing functions of a self-sensing actuator. In the current chapter instead a look is taken at the capability of a complete hardware control system to actively control tool vibrations by means of a self-sensing actuator. The main contents of this chapter consist of the paper by Freyer, Theron, Heyns & Pickelmann (2016).

In Chapter 2 it was mentioned that by using a piezoelectric self-sensing actuator for tool vibration control two problems can be overcome. These are the problem of a lacking space around the tool tip and increased costs if separate actuators and sensors are used. What hasn't been mentioned though is that in spite of its small size a piezoelectric actuator is capable of exerting high forces. This property makes the SSA suitable to be positioned close to the neutral axis of tool holder subjected to bending by tangential cutting forces as depicted in Figure 3.1 and in Andrén et al. (2003). Even though undergoing little strain close to the neutral axis it is sufficiently sensitive to make a signal available for both, TCM and control system feedback purposes. As already said in Chapter 3 such a tool holder-SSA configuration could due time constraints not be included in this work.

By the piezoelectric actuator's suitability as stated above and also accompanying advantages for the turning process as mentioned in Chapter 1 and 2, tool vibration control in general but also using a self-sensing actuator in particular is motivated.

Literature shows that the general concept of a SSA has been proven in laboratory environment before (Anderson et al., 1994). This however was not on a set-up typical of a turning process as offered in this chapter. This part of the work makes use of a practical set-up. A mechanical structure of a representative tool post with tool holder is excited by narrow band tool vibration force inputs. These were previously recorded as tangential cutting force signals in a real turning process and were for initial simplicity purposes confined to respectively 100 and 200 Hz bandwidths. This proposed practical solution comprises two essential building blocks. These are the sensing circuit with integrated SSA and the control

algorithm with an incorporated linear time invariant (LTI) forward path model. Besides identification of the forward path, measures toward linearization of the SSA are described in this chapter.

The sensing circuit is a hardware building block. It is basically adopted from Anderson and Hagood (1994) as a bridge circuit with the SSA as an active component in one of its branches. It captures a strain proportional signal which constitutes the variable directly affected by a force induced disturbance on the strain of the SSA.

An embedded controller is the software building block. This includes the control algorithm and model by way of its coefficients being the information for a digital signal processor (DSP) application. Real cutting forces are non-stationary (Sturesson, Håkansson, & Claesson, 1997). They therefore require a type of adaptive control algorithm. A filtered-x LMS (FXLMS) algorithm was selected as in Andren et al. (2003), however with modifications originating from Kuo, Kong & Gan (2003). This is referred to as the adaptive feedback noise control algorithm (AFANC). Instead of the delayed error, in this chapter a delayed disturbance signal as suggested in Kuo et al. (2003) constitutes the reference signal for the algorithm. This algorithm was selected due to improved performance it showed in simulation with a perfect plant estimate. This performance is here traded off against a decreased stability region with an imperfect plant model (Elliott, 2001:135).

The main objective of the work described in this chapter is to demonstrate how the building blocks introduced above function as a complete system. This includes a suitable signal-to-noise ratio not below a required minimum for the sensing circuit. From the software building block it is required that it should demonstrate clear performance w.r.t. vibration attenuation. All the modules that would be present in a real turning process are involved in the proposed concept paving the way towards application in such processes. A simplified yet adequately efficient system constitutes the contribution of this chapter.

The next section gives a description on material and methods of the experimental set-up. This includes a description of the test structure, sensing circuit and information that entered the DSP. The same section discusses the force signals for the experiment and also the experimental procedure. A section on theory and calculations contains sensing circuit theory and linearization measures. Furthermore it provides system identification, and the vibration

control algorithm description as part of the DSP information. The remaining sections show the results due to vibration control using a self-sensing actuator and their discussion.

4.2. MATERIAL AND METHODS

This section describes the set-up w.r.t. the structure under test, where the vibration problem is located and two building blocks of the solution. Test signals previously recorded as tangential cutting force signals from a real turning process, are used to drive a shaker which in turn excites emulated tool vibration. This section also briefly deals with these signals. At the end of this section a description of a procedure by which the experiment was conducted is given.

The actuator/tool holder configuration used for simulation purposes in chapter 2 to demonstrate the use of a SSA was similar but not exactly the same as the used in chapter 4. Chapter 2 described the simulation of the principle of which a test bench implementation with a slightly different algorithm is shown in chapter 4. Figure 4.1 gives an overview of this actuator/tool holder structure as well as the two main building blocks, viz. sensing circuit and embedded controller information on the DSP. The test signals in Figure 4.1 follow the path via the PA100E amplifier to the shaker which then converts them into a force to excite the tool holder substitute. This results in emulated tool vibrations. Figure 4.1 also shows complementary equipment for the experiment. Photos of the set-up of Figure 4.1 can be seen in Appendix H. Table 4.1 lists the equipment that was used for the experiment.

4.2.1. Test structure

The structural part of the set-up gives account of the structural dynamic problem. This part constitutes a structure representative of a tool-holder as it would be clamped in a tool post and is depicted in Figure 4.1. A stack actuator, here also referred to as SSA, extended in a direction opposite to the force by the shaker. The stack actuator made contact with the substitute tool holder at an offset from the shaker force application point. This contact was not by positive form locking but by a spherical actuator tip against a flat surface to prevent damaging moments being transferred from the substitute tool holder to the ceramic stack of the SSA.

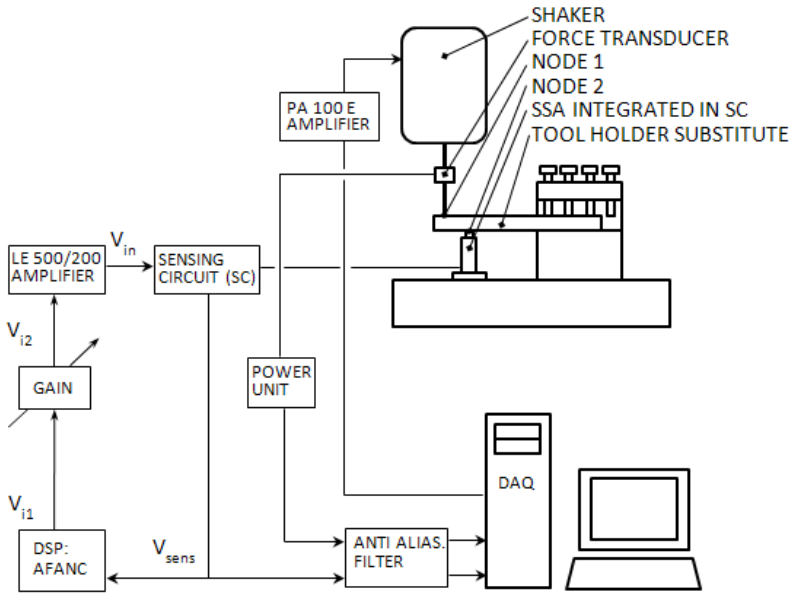

Figure 4.1: Experimental set-up for active control of emulated tool vibration using a self-sensing actuator.

Table 4.1: Equipment used in experimental set-up

Item	Type
Piezo drive amplifier	LE 500/200 voltage amplifier, Piezomechanik GmbH
Piezoelectric actuator	Stack actuator: PSt 500/10/15 VS18, Piezomechanik GmbH : $n = 50$, $K_a = 120\ N/\mu m$, $d_{33} = 450\ pm/V$
Electrodynamic shaker	Ling Dynamic Systems, V406/8
Shaker drive amplifier	Ling Dynamic Systems, PA100E
Force transducer	Model 208B02, PCB Piezotronics
Force transducer power unit	Model 480E09 ICP, PCB Piezotronics
Digital signal processor	TMS320C6713, Texas Instruments
Analog-to-digital converter	ADS 8361, Texas Instruments
Digital-to-analog converter	DAC 8554, Texas Instruments
Converter interface	5-6K Interface, Texas Instruments
Data acquisition card (DAQ)	PCI-6251 M-series, National Instruments
DAQ connector block	BNC-2110, National Instruments

4.2.2. Sensing circuit

The sensing circuit (SC) block in Figure 4.1 is shown in detail in Figure 4.2. The principle of the SC is mainly that of an impedance bridge. It is a module with several electrical time

dependent variables as states. One of them is the voltage difference in the sensing branch which is an output variable of interest in this chapter.

The output, also used as feedback variable, is proportional to the axial strain of the stack SSA. Another output, ΔV_{shunt}, only plays a role in a feedback system alluded to in section 4.3.2.1. For the purpose of this part of the work the sensing circuit thus is a single input single output (SISO) unit.

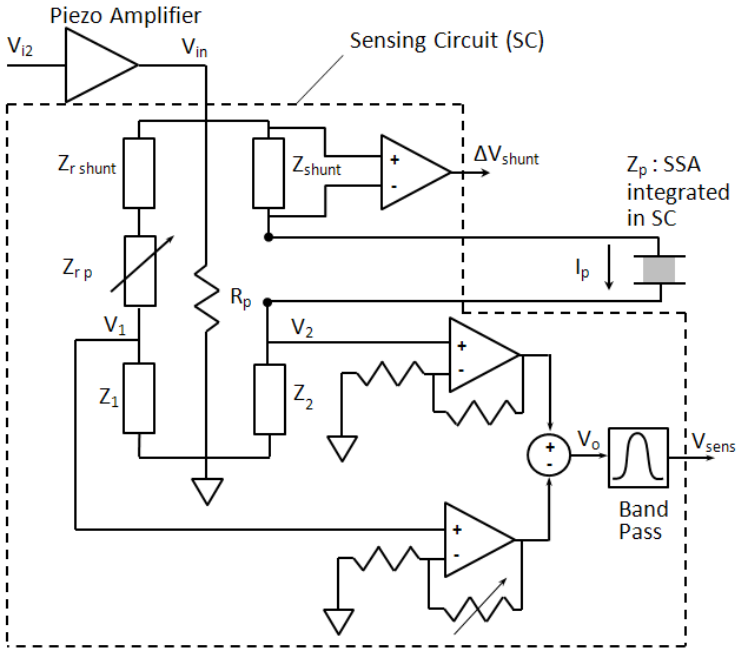

Figure 4.2: Circuit diagram of sensing circuit with integrated SSA

The parameterization of this circuit is determined by the capacitance of the SSA. The ratios between $Z_{rp}/\,Z_1 = Z_p/Z_2$, with $Z_p = Z_{rp}$, are according to values suggested by Anderson et al. (1994). The reason for the parallel resistors in Z_1 and Z_2 is mentioned in that source. The purpose of additional parallel capacitances in Z_{shunt} and $Z_{r\,shunt}$ was to increase the small parallel inherent capacitance of the high power shunts of Z_{shunt} and $Z_{r\,shunt}$ respectively. This is done to ascertain that the main voltage drop between V_{in} and ground is across Z_p and its matching reference impedance, Z_{rp}, respectively. The components and specifications of respectively the impedance bridge and band pass filter of the sensing circuit are listed in Table 4.2.

4.2.3. DSP information

The basis for the information coded for the DSP is further considered in this section. The C-coded information that entered the DSP application consisted of the AFANC algorithm and also the model coefficients that were obtained through mode finding and model identification of the forward path of the control system.

The model coefficients for the AFANC filters are based on a sampling time of 4 μs which corresponds to a $250kHz$ sampling rate. This is the sampling rate at which the external data converters were run at. The used DSP and external data converter types are listed in Table 4.1. The decision for external data converters was associated with the advantage of lower phase loss than would have been the case with on-board coder-decoder (codec) of the DSP.

Table 4.2: Impedance bridge and band pass data

Impedance bridge	
Impedance	Value
$Z_{r\,shunt}, Z_{shunt}$	$6\ \mu F\ ||\ 2.9\ Ohm$
$Z_{r\,p}, Z_p$	$207\ nF$
Z_1, Z_2	$2.2\ \mu F\ ||100\ Ohm$
R_p	$220 \cdot 10^3\ Ohm$
Band-pass	
Parameter	Value
Bandwidth	$\Delta\omega = 205 \cdot 2\pi\ rad/s$
Centre frequency	$f_o = 2050\ Hz$
Gain at f_o	$G = 1$
Quality factor	$Q = \Delta\omega/(2\pi f_o) = 10$

4.2.3.1. Mode finding

A model of the path consisting of the digital signal processor (DSP), the voltage amplifier and the impedance bridge was needed in the form of a linear parametric model. The bending mode of the substitute tool holder had to be known while the tool holder is subjected to the mass load effect of the force transducer and stinger. This had to be done because of the

influence the mass-to-stiffness ratio has on the bending mode when the substitute tool holder is connected to the shaker.

The mode finding procedure therefore followed two steps. These were followed to determine the mass load effect of the force transducer and the shaker's stinger on the substitute tool holder. The first step consisted of application of a zero to 8000 Hz bandwidth random noise to the shaker, which exerted the output force onto the passive cantilever structure shown in Figure 4.3. The associated force signal and a strain signal were measured as input and output signals by a dynamic force transducer and the SSA respectively and resulted in the frequency response function (FRF) in Figure 4.4. In this configuration the signal V_{ssa} was recorded directly at the SSA terminals without the SSA being integrated in the sensing circuit. This first step was to find the frequency of the first bending mode of the substitute tool holder when it is connected to the shaker via the stinger. Figure 4.4 shows that this could be obtained at 2050 Hz. The peaks at this frequency and at 6500 Hz refer to modes, i.e. natural frequencies of the tool holder substitute for transfer behaviour with the force, V_{ft}, signal close to its tip as input and the strain proportional signal sensed by the SSA, V_{ssa}, as output.

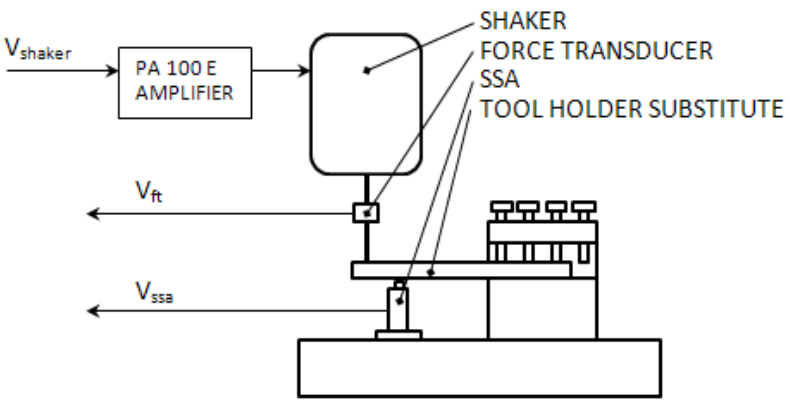

Figure 4.3: Experimental set-up for input-output data measurements for estimating the FRF exhibiting of the substitute tool holder.

The second step was to then disconnect the shaker and adjust the mass load at the stinger connection point of the cantilever, such that the frequency of the first bending mode would be at a value of the one obtained in the first step. The bending mode after adjustment was observed on an FRF graph with voltage input to a buffer before piezo amplifier as input and V_o as output signal as in Figure 4.5. After applying the mass load needed to shift the bending

mode to 2050 Hz one can see minor frequency effects at 2050 Hz in Figure 4.5. They are hardly visible due to other units such as the piezo amplifier and the impedance bridge on the path of the FRF measurements.

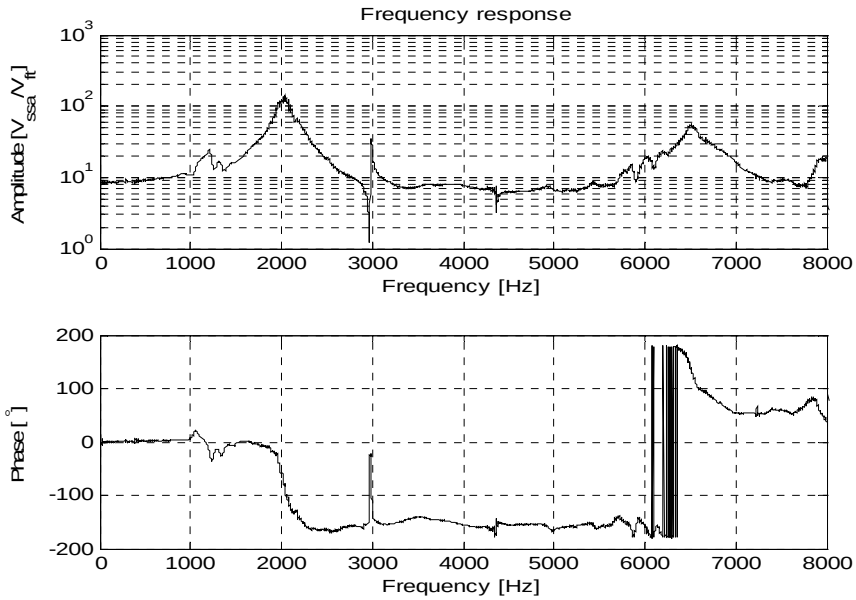

Figure 4.4: FRF with force transducer signal, V_{ft} , as input and signal, V_{ssa}, obtained from piezo SSA as output.

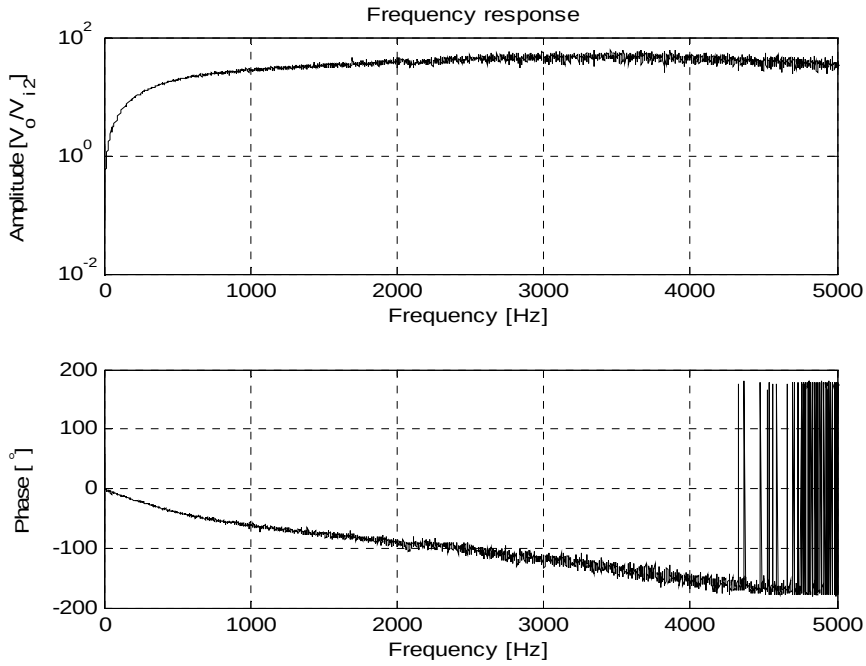

Figure 4.5: FRF of forward path section with voltage input to buffer before piezo amplifier as input and V_o as output signal.

4.2.3.2. Model identification

With knowledge of the bending mode from the first step in section 4.2.3.1 and mass load adjusted as in the second step in section 4.2.3.1 model identification could be performed. This could be done on the substitute tool holder disconnected from the shaker and with its mass load adjustment.

A 0 to 8000 Hz white noise input signal, $V_{i\,dsp}$, to the DSP and an anti-alias filtered V_{sens}, respectively provided the input and raw output data. The anti-alias low pass filter (6^{th} order Butterworth) had a $30kHz$ corner frequency. Data consisting of $V_{i\,dsp}$were read from and then acquired as anti-alias filtered V_{sens} by the data acquisition card specified in Table 4.1. Delayed by only a sampling instant the raw output data was acquired similarly. A sampling rate as high as $100kHz$ was used to be above a minimum of at least 10 times the bandwidth of the control system in order to approach a continuous model (Lutz & Wendt, 2002:667). The reason for conservatively choosing it much higher was to prevent loss of accuracy in case of a wider bandwidth. Before used for model identification the raw output data was filtered through an inverse model of abovementioned anti-alias filter.

The model identification itself was performed to obtain a linear parametric model, here also referred to as the forward path. During this identification, the algorithm instructions on the DSP were programmed to contribute to processing time only and not to data manipulation. This was done by letting the algorithm instructions be processed, but assigning the input data instead of the algorithm output directly to the output variable. The band pass filter at the impedance bridge's sensing branch was the last unit of the forward path. The output signal from this unit was the result from the strain of the piezoelectric transducer. Therefore it is here called a self-sensing actuator, which fulfils the two functions of sensing and actuation respectively.

Modeling of structures is often done using structural dynamics software packages. However instead of the latter type of software it was decided to use System Identification (SID) Toolbox by MATLAB (2007). There were mainly two reasons for this decision and that is that SID Toolbox is also suited for the modelling of a general system which includes an actuator and also the transfer behaviour of the electronic and electrical equipment.

Pre-processing was performed on the SID data set by removing the means and pre-filtering over the interval $[1942 \quad 2149]\,Hz$. This allowed the fit of the model to focus on that interval. Furthermore this modelling software allows focus on stability, i.e. all poles to lie within the unit circle of complex z-domain, when doing the model parameter estimation. It was reasonable to expect the system to be stable due to the viscous modal damping that occurs in the structure and the collocated actuator/sensor pair.

4.2.3.3. Control method

In the remainder of this chapter it is the convention that lowercase bold symbols represent vectors of delayed samples at the time instant indicated by the subscript, k.

The control method as shown in Figure 4.1 encompasses a vibration control loop with feedback signal, V_{sens} . It is also represented as the block diagram shown in Figure 4.6. In this diagram the filters indicated with a T stand for the linear time-invariant (LTI) transfer behaviour between a sampled input signal and a sampled output signal. T_f in particular is the transfer function of the forward path, i.e. the physical set-up, which includes the DSP, the voltage amplifier and the impedance bridge to the sensed bridge voltage, V_{sens} , as output. The signal sample $e_k = V_{sens\,k}$ is the signal sample sensed by the sensing circuit at time instance k and is the input to the control algorithm embedded on the DSP. The signal commanded by the control algorithm to the SSA, i.e. the output signal from the DSP at time instance, k, is represented by the sum of the signal samples u_k and n_k. Here n_k is the noise imposed on the adaptive filter output, u_k.

The forward path is denoted as

$$T_f(z) = \frac{C(z)}{1-G(z)} \tag{4.1}$$

and $T_{21}(z)$ denotes the filter of the transfer function relating the input force at node 1, at the tool tip to the displacement, d_k, at node 2, resulting from the input force to the structure, f_k. Node 2 is the point of contact of the SSA and the bar representing the tool holder as indicated in Figure 4.1.

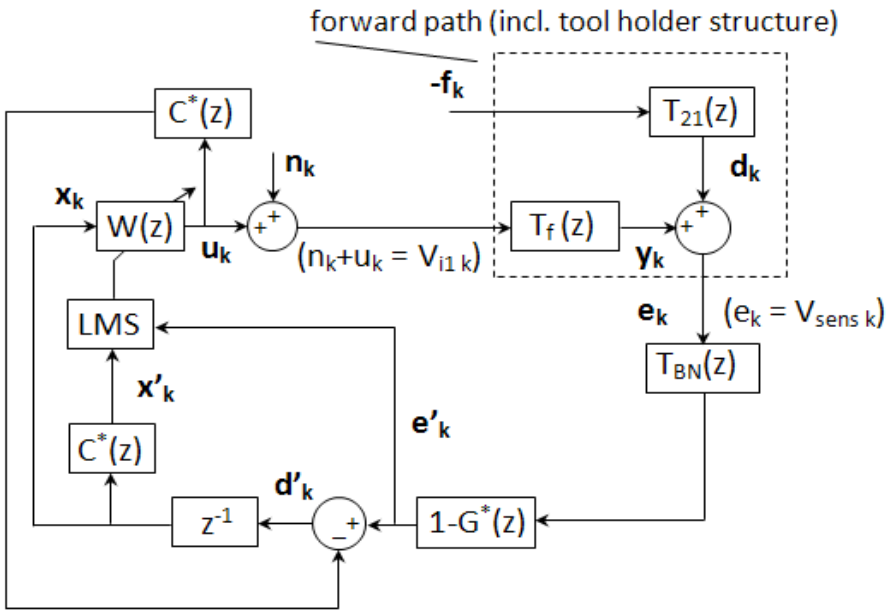

Figure 4.6: Block diagram of control system based on AFANC

The input to the controller first undergoes a bias removal using the bias-notch filter

$$T_{BN}(z) = \frac{z-1}{z-0.995} \tag{4.2}$$

with a pole slightly left of the zero on the unit circle as discussed by Widrow & Stearns (1995:323). Filter, $W(z)$, is a 16 tap adaptive finite impulse response (FIR)-filter.

The C-code for the least-mean-square (LMS) section of the AFANC algorithm was adopted from Chassaing (2005:263). On the DSP in Table 4.1 it was subjected to processor-in-the-loop (PIL) testing using MATLAB (2006b,c,d,e,f,g,h) with the following toolboxes:

a) Simulink
b) Embedded Target for TI C6000 DSP(tm)
c) Link for Code Composer Studio
d) Real-Time Workshop
e) Signal Processing Block Set
f) Signal Processing Toolbox

Two real time data exchange (RTDX) channels respectively for write and read purposes and a buffer in a MATLAB loop structure program on the host PC were created (Chassaing (2005:313). The RTDX channels then allow data exchange between the host PC and the processor (DSP). This means that data are sent sample by sample from to the processor through RTDX channels via the on-board Joint Test Action Group (JTAG) interface. After being processed by the DSP, data is received via the JTAG and an RTDX channel by the MATLAB program and workspace. A functional AFANC algorithm in Simulink with exactly the same parameters as the C-program on the processor was used as reference. The received data, i.e. output data from the processor, was compared to the output of the reference program. This comparison showed that there was no processing error by the C-coded AFANC algorithm on the processor. The Simulink program was again tested in simulation of tool vibration control and reached performance levels similar to that in Chapter 2.

4.2.4. Test signals

The test signals for this work were previously measured in a turning process on a manually operated Colchester Student lathe. The cutting speed, feed rate and depth of cut during this measurement were 86.4 to $96.6\,m/min$, $0.3\,mm/rev$ and $1\,mm$ respectively. The measurements were conducted by means of a strain gauge instrumented tool holder according to the method that has been described in Chapter 2. There it is shown how a calibration matrix is used to convert the so measured vibration signals into force signals.

The decision to use the force component tangential to the work piece as a test signal is based on information regarding its contribution to relative tool work piece displacement. The force components in turning are the tangential component, P_1 and two components, P_2 and P_3 orthogonal to it respectively in feed and radial direction. According to Koenigsberger (1964:5), P_1 is the main component normally with $P_3 \approx 0.3P_1$ and $P_2 \approx 0.15P_1$ to $P_2 \approx 0.5P_1$. A relatively high force-to-stiffness ratio in the direction of P_1 for a standard tool holder results in its increased deflection in that direction. A consequence of this is a significant contribution towards tool work piece displacement with resulting surface roughness.

During these measurements the first bending mode of the strain gauge instrumented tool holder in tangential direction was excited by the force in the same direction and was at $1355.9\ Hz$.

Allowing the effects of the tangential excitation force through, the tool holder has a pass band for vibrations in that direction at the first bending mode. The frequency range of the measured signal in this pass band was shifted to a frequency range of equal width centred at the equivalent mode of the substitute tool holder at $2050\ Hz$. A shift in the frequency domain was done on frequency components of respectively a $100\ Hz$ frequency range for the one and $200\ Hz$ for the other signal. The frequency ranges outside these bands were filled with low amplitude system noise from high frequency ranges.

With the data acquisition at sampling rate $F_s = 100kHz$ these signals were applied to the driving amplifier of the shaker, PA 100 E, for two separate test runs. Their power spectral densities are shown in Figure 4.7. The selection of this sampling rate had the same basis than that for model identification. The choice for a higher sampling rate came at negligible additional cost only.

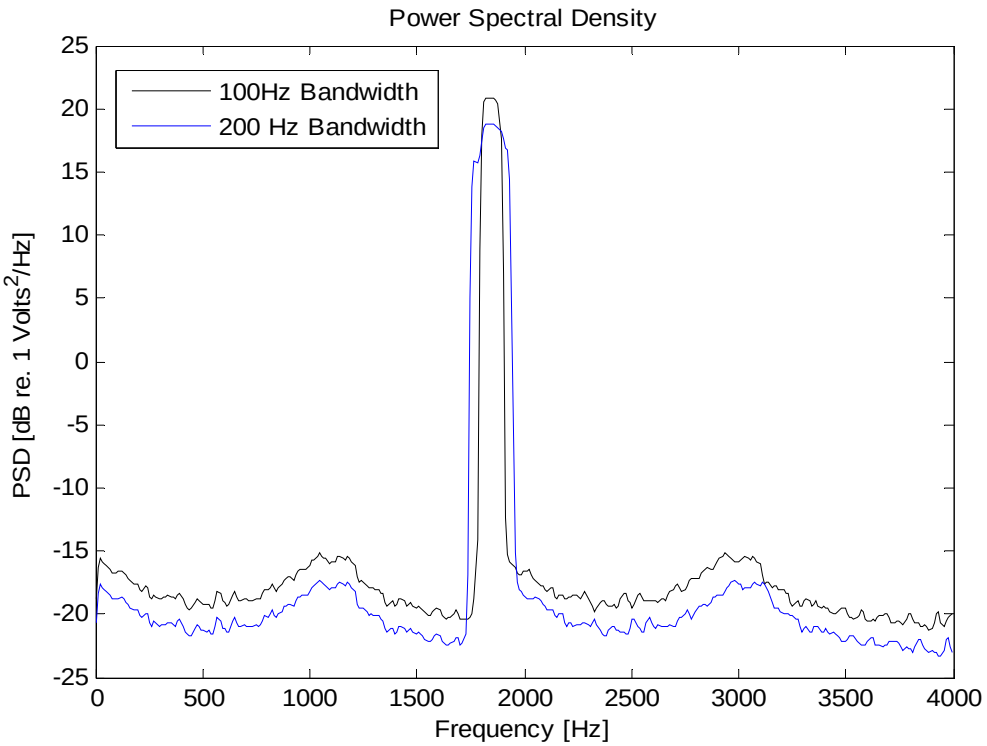

Figure 4.7: Power spectral densities (PSDs) of 100 Hz and 200 Hz bandwidth test signals respectively.

4.2.5. Experiment

As part of the experiment, the impedance bridge had to be balanced and impedances matched before the actual vibration control of the tool holder substitute could be tested.

First passive ceramic capacitors of XR7 material were used in the place of the impedances of Z_p and Z_{rp} and their capacitances matched to one another. These capacitors had capacitances in the order of the PSt 500/10/15 VS18 actuator, Z_p , and its reference capacitor, Z_{rp}. A signal V_{i1} was applied to the open-loop set-up. The bridge was then balanced by reducing the sensed output signal, V_{sens}, to a minimum in root-mean-square value via the potentiometer in the sensing branch of the bridge circuit. An adjustable polystyrene capacitor was used as additional capacitance to complement the mismatches.

The next step was to match the actuator, Z_p, and a passive capacitor of XR7 material, Z_{rp}, respectively. They were matched with respect to both their capacitances and dissipation factors such that they would have equal effect on phase of each, V_2 and V_1. Here too an adjustable polystyrene capacitor was used as additional capacitance to complement the mismatches.

The two test signals had bandwidths of $100\,Hz$ and $200\,Hz$ respectively around a centre frequency of $2050\,Hz$. They were applied to the shaker amplifier PA 100E (volume dial set to 95% of its range) and subsequently to the shaker. The shaker converted the signals to forces that were exerted on the substitute tool holder.

The signal that was then acquired was the voltage, V_{sens}, which is proportional to the deflection at the point of contact of the SSA with the substitute tool holder. The data acquisition was performed open loop and closed loop, i.e. without and with control, respectively and can be seen in the graphs of Figures 4.14 and 4.15.

4.3. THEORY AND CALCULATIONS

4.3.1. Sensing circuit

This section provides a look into the theoretical basis of the sensing circuit output, i.e. the hardware building block. The sensor equation therefore assists in this as a starting point and is formulated in Anderson et al. (1994) as

$$\theta_p \, r + C_p v = q_p \tag{4.3}$$

where $\theta_p = n \, d_{33} \, K_a$ with n, the number of layers in the stack, d_{33}, a piezoelectric constant and K_a the actuator stiffness. C_p is the actuator's capacitance, while r, q_p and v are the piezo actuator tip displacement, the charge on the piezo stack, and the voltage across its electrodes respectively.

If no charge from the stack actuator is lost, e.g. the piezo SSA is an open circuit, then the voltage, v, that appears across the piezo stack electrodes becomes

$$v = -\theta_p \, r / C_p \, . \tag{4.4}$$

The charge, q_p, that appears on the electrodes of the piezo stack is generated when the stack actuator is compressed by a displacement, r. In the literature (Roddeck, 2003:11) this is called the piezoelectric effect and Dosch et al. (1992) represent this effect as a voltage source in circuit diagrams.

In the derivation of an expression for the voltage sensed by the impedance bridge, V_o, as it was done in Anderson et al.(1994) the piezoelectric effect was taken into account. Here it appears in the second term of the expression for the voltage across the actuator and shunt, V_{act}, as

$$V_{act} = V_{in} - V_2 = \frac{(Z_p + Z_{shunt})}{(Z_p + Z_{shunt} + Z_2)} V_{in} - \frac{Z_2 \theta_p \, r}{(Z_p + Z_{shunt} + Z_2) C_p} \, . \tag{4.5}$$

Based on Anderson et al. (1994), V_2 is obtained from the rearranged (4.5),

$$V_2 = \frac{Z_2 Z_p}{(Z_2+Z_p+Z_{shunt})} s \left(\frac{V_{in}}{sZ_p} + \theta_p r\right) \tag{4.6}$$

and V_1 is

$$V_1 = \frac{Z_1}{(Z_1+Z_{rp}+Z_{r\,shunt})} V_{in} \,. \tag{4.7}$$

From (4.6) and (4.7) the output of the impedance bridge, V_o, can be obtained as

$$\begin{aligned} V_o = \left(g_1 Z_1/\left(Z_1 + Z_{r\,p} + Z_{r\,shunt}\right) - g_2 Z_2/\left(Z_2 + Z_p + Z_{shunt}\right)\right) V_{in} \\ -s g_2 \left(Z_2 Z_p/\left(Z_2 + Z_p + Z_{shunt}\right)\right) \theta_p r. \end{aligned} \tag{4.8}$$

The gains for V_1 and V_2 are represented by g_1 and g_2 respectively. If the bridge is perfectly balanced and $g_1 = g_2$, V_o is represented by the second term of (4.8) only as

$$V_o = -Z_m(s)\theta_p r \,. \tag{4.9}$$

V_o can therefore be used as the feedback signal in a control system, which counteracts disturbances in order to keep the displacement at the particular node of contact as small as

possible. This is node 2 in Figure 4.1 between the actuator and the tool holder. The impedance bridge contains voltage dividers in each of its legs, which provide the voltages V_1 and V_2, that are differenced. It also contains a current divider with two capacitive bridge legs and a purely resistive third leg. The resistive leg allows dc current to pass through and thus has a low pass filter function to fulfil. The $0Hz$ offset current is associated with the voltage V_{in} which has an offset due to uni-polar operation of the amplifier. This insight is put forward in Moheimani et al. (2006:126) to justify the additional by-pass path in the bridge circuit. As a result of the current divider low pass filter, the current through the resistive leg becomes

$$I_R = \frac{(R_P C_B s+1)}{R_P C_B s} I_{in} \tag{4.10}$$

where C_B is the total equivalent capacitance of the two capacitive bridge legs and I_{in} is the total current delivered to the impedance bridge.

4.3.2. Linearization measures

4.3.2.1. Input voltage tracking by current in piezo SSA

A controlled output voltage amplifier was available to drive the SSA. It is however generally known, amongst others from Moheimani et al. (2006:214), that when a controlled output voltage amplifier drives piezoelectric actuators the latter exhibit non-linear hysteresis. However non-linearity is negligible when a controlled current amplifier drives the actuators. The necessity to convert the available controlled voltage amplifier into a controlled current amplifier was therefore evaluated.

In addition to linearization, the controlled current amplifier offers the benefit of enhanced stiffness of the actuator. Pickelmann (2010) explains the reason behind this. It is generally known that for a controlled output voltage amplifier its output voltage tends to follow the input voltage independent of load and delivers current correspondingly (Millman and Halkias, 1967:480). When exhibiting the aforementioned piezoelectric effect, the piezo actuator will generate charge on its electrodes while subjected to compression. Associated with this an electric field in the piezoelectric actuator is caused which however is opposed by the driving amplifier's voltage output (Dosch et al., 1992). This leads to loss of the electric field in the stack, which in turn is responsible for the piezo actuator's loss of stiffness. Heimann et al. (2001:56) give a proportional relationship between electric field strength and stiffness. This restricts the actuator to react with less force. If however the piezo actuator current is controlled instead, the amplifier output voltage is free to increase when a force is exerted on the piezo actuator. Via the driving amplifier one therefore has control over the charge content on the piezo actuator, the electric field and consequently its stiffness. Two equations from Anderson et al. (1994) illustrate this by means of the rewritten sensor equation (4.3)

$$\theta_p \, r = q_p - C_p v \, , \tag{4.11}$$

A situation of no charge leakage from the piezo stack occurs when the charge to the SSA (i.e. the current) is controlled and thus the charge content on the actuator and leakage disturbances are compensated by the control, which is the situation described by (4.4).

For this part of the work a current controlled drive amplifier would mean that an inner feedback loop as shown in Appendix G in Figure G.1 be implemented such that the current in

the piezo actuator would track V_{i1}. According to Bayerle (2015) this can be done by measuring the voltage difference across the shunt, ΔV_{shunt} , e.g. on the high voltage side of the piezo actuator and performing a $+90^{\circ}$phase shift on it before feeding it back, if ΔV_{shunt} is in phase with the piezo amplifier input voltage.

However it was found that the phase of ΔV_{shunt} at $2050\ Hz$ is already about 76° relative to the piezo amplifier input voltage, V_{i1} as shown in Figure 4.8. Therefore the phase of the current in the piezo actuator would be -14° , i.e. it is lagging V_{i1} by only 14° . For the purposes of this study this lag was assumed to be sufficiently close to 0°. For a more accurate tracking of V_{i1} by the piezo current the phase of ΔV_{shunt} would have to be 90° across the entire bandwidth of the control system.

4.3.2.2. Imposing of pseudo random noise

As a further measure to achieve linearization of the hysteresis found on piezoelectric actuators pseudo random noise was imposed on the control algorithm output, $\boldsymbol{u}_k$.

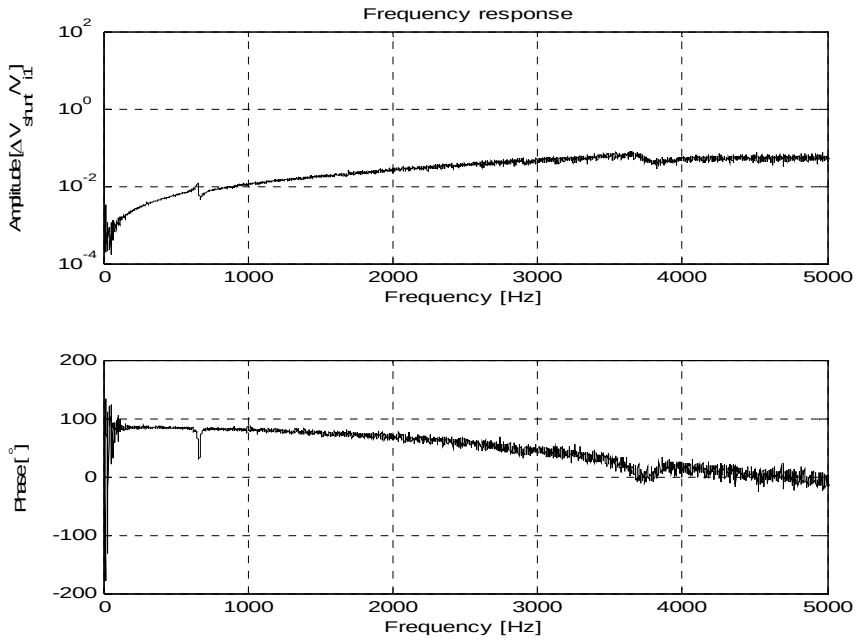

Figure 4.8: FRF with V_{i1} as input and ΔV_{shunt} as output signal indicating phase of shunt current relative to V_{i1}.

This was performed on each control algorithm output sample u_k as follows:

a. Generate a random number $n_{r\,k}$:

$$n_{r\,k} \in [-10, 10] \tag{4.12}$$

b. Obtain modified running mean m'_k :

$$m'_k = \left|\frac{K}{N}\sum_{j=k+1-L}^{k} u_j\right| \tag{4.13}$$

where $K = 5 \times 10^{-7}$ is a signal-to-noise-ratio (SNR) tuning factor and $N = 25$ is the window length over which the mean is calculated.

c. Obtain random signal m_k proportional to m'_k:

$$m_k = n_{r\,k} \cdot m'_k \tag{4.14}$$

d. Filter $\boldsymbol{m}_k = [m_k, \ldots m_{k-L}]$ through a series of two identical second order band pass filters, $G_{bp}(z)$, with centre frequency at $f_n = 110\,kHz$ and under-damped with damping ratio $\zeta = 0.1$. This type of band pass filter was selected because only a narrow band was needed to let random noise pass through. The centre frequency was chosen sufficiently high but safely below the Nyquist frequency of the DSP sampling rate. This series of filters is in the form of program code just after the control algorithm. The noise used was thus amplitude specific and also frequency specific $\boldsymbol{n}_k$:

$$\boldsymbol{n}_k = G_{bp}(z) \cdot G_{bp}(z) \cdot \boldsymbol{m}_k \tag{4.15}$$

where $G_{bp}(z)$ is the z-transform with the zero-order-hold method at sampling time $T_s = 1/250000$ seconds of

$$G_{bp}(s) = \frac{(2\pi f_n)^2}{s^2 + (4\zeta\pi f_n)s + (2\pi f_n)^2} \tag{4.16}$$

e. The pseudo random noise, n_k was then imposed on controller output value u_k:

$$v_k = u_k + n_k \tag{4.17}$$

where $V_{i1} = v_k$.

With the manipulation on a random signal as described above, a linearizing effect was visible on the hysteresis of strain versus applied voltage of the piezo actuator at 2050 Hz.

Imposing of pseudo-random noise to the voltage applied to the piezoelectric actuator has an overall linearizing effect and is shown in Figures 4.9 and 4.10. In the left graph of Figure 4.9 however the loop that can be seen is mainly a result of lag since low voltages were applied. If higher voltages were applied the extreme points of the loop would become sharper as in Figure 4.10 and effects of hysteresis would become visible (Moheimani et al., 2006:204). Pseudo random noise causes the more inflated hysteresis loop to collapse.

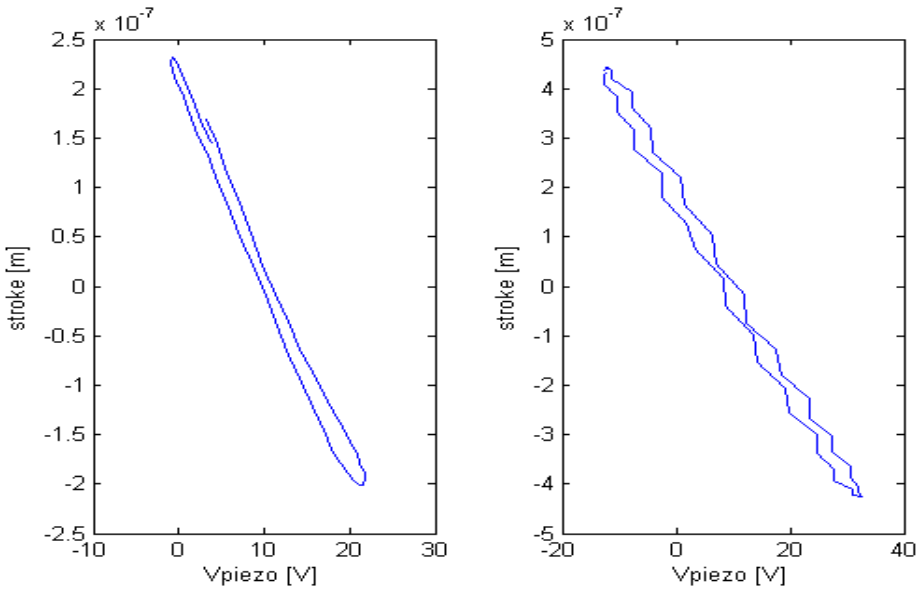

Figure 4.9: Piezo stack actuator stroke vs. applied voltage, without pseudo-random applied to V_{piezo} (left graph) and with pseudo-random applied to V_{piezo} (right graph).

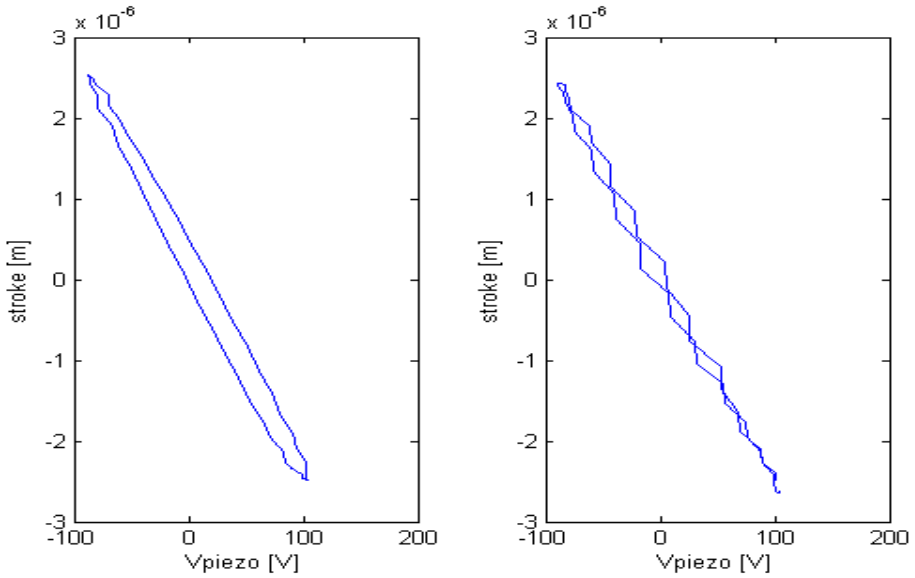

Figure 4.10: Piezo stack actuator stroke vs. applied voltage, without pseudo-random applied to V_{piezo} (left graph) and with pseudo-random applied to V_{piezo} (right graph).

This linearization measure is therefore most effective for longer stroke lengths such as in real turning processes and may be used in combination with the assurance that piezo current is sufficiently tracking piezo amplifier input voltage.

4.3.3. DSP information

A theoretical basis for the software building block, viz. DSP information, will follow in this section regarding system identification and the control algorithm.

4.3.3.1. System identification

Since the forward path is made up of a number of units, a higher order model for it was expected. The state space representation is known to be a reliable linear time invariant (LTI) type of model and allow for stable computer analysis algorithms (MATLAB, 2003a). A 6th order model was recommended by the order selection option if the model was to be of state space form. The forward path was therefore identified as a narrow band 6th order state space

model with focus on stability. The prediction error method (PEM) from Ljung (1987:171) was selected for identification of the model parameters. Findings from the use of the control algorithm, discussed later, were that it showed improved performance if the model of the forward path was a model of lower order. Model order reduction which removes those states that hardly change over time compared to the remaining states of the process (Föllinger, 1990:585; MATLAB, 2003a) was then performed. The state space system was reduced to second order and converted to a z-domain transfer function. Its parameters were accommodated in the discrete transfer function of the form

$$T_f(z,\theta) = \frac{B(z)}{A(z)} \quad \text{and} \quad H(z,\theta) = \frac{1}{A(z)} \ . \tag{4.18}$$

with the model parameters,

$$\theta = [a_1 \cdots a_{na} \quad b_1 \cdots b_{nb}]^T, \tag{4.19}$$

where $H(z,\theta)$ is the noise model in the relationship

$$y(t) = T_f(z,\theta)u(t) + H(z,\theta)e(t) \ . \tag{4.20}$$

The role of the parameters in (4.19) can be illustrated with the equation error model (Ljung , 1987:71) in terms of the output $y(t)$ and input $u(t)$ as

$$y(t) + a_1 y(t-1) + \cdots a_{na} y(t-na) = b_1 u(t-nk) + b_2 u(t-nk-1) + \cdots + b_{nb} u(t-nk-nb+1) + e(t). \tag{4.21}$$

with $e(t)$ being a white noise term entering directly. The integer nk is relating sampling period T_s to dead-time t_d in the model as

$$t_d = nk\, T_s \ . \tag{4.22}$$

The second order system in the z-domain was obtained as the transfer function

$$T_f(z) = \frac{-0.03887\, z^2 - 0.1654\, z + 0.2036}{z^2 - 1.993\, z + 0.9956} \ . \tag{4.23}$$

The fit of the estimated model versus a FRF of the measured data is shown in Figure 4.11 for a narrow band. An idea of the accuracy of this transfer function model is given by its percentage fit as

$$fit = 100\,(1 - \bar{\sigma}(\boldsymbol{y}_{m\,k} - \boldsymbol{y}_k)/\bar{\sigma}(\boldsymbol{y}_k - \bar{\boldsymbol{y}}_k)), \tag{4.24}$$

according to MATLAB (2007). In (4.24) $\boldsymbol{y}_{m\,k}$ is the simulated output of the model, $\boldsymbol{y}_k$ the measured output, $\bar{\boldsymbol{y}}_k$ its mean and the operator $\bar{\sigma}$ denotes the maximum singular value of the operand. A fit of 86 % was obtained with the model in (4.23). The presence of autocorrelation of the residuals, also referred to as error, $\boldsymbol{y}_k - \boldsymbol{y}_{mk}$, means that the autocorrelation function plotted in the upper graph in Figure 4.12 lies outside the 99% confidence region. This in turn means that the error can be described by a model, i.e. it results from a discrepancy between the model output, $\boldsymbol{y}_{mk}$ and $\boldsymbol{y}_k$ and is not white noise. Due to its tightness the 99% confidence region presents in the upper graph in Figure 4.12 close to zero autocorrelation as wide black line. A model of the error appears in an additional second term such as the noise model in (4.20). For a reliable estimate of a model, referring to the forward path model, one would however expect the error to be white noise (Ljung , 1987:428).

The measured input, which is the same as that for the model, in cross-correlation with the residual, indicates that the residual is not independent from the input due to the presence of cross-correlation outside the 99% confidence. Incorrect estimation of time-delays corresponds to positive values for the cross-correlation. When the cross-correlation would be lying in the yellow region in Figure 4.12, a 99% confidence of independence could be guaranteed.

A time domain comparison of the simulated model output and the measured output for the same input is shown in Figure 4.13. It is the model in (4.23) with 86% fit, according to (4.24). Due to time constraints in this work the decision to use this model was based on the percentage fit only, while note was taken of the model deficiencies as indicated by the residual plots in Figure 4.12.

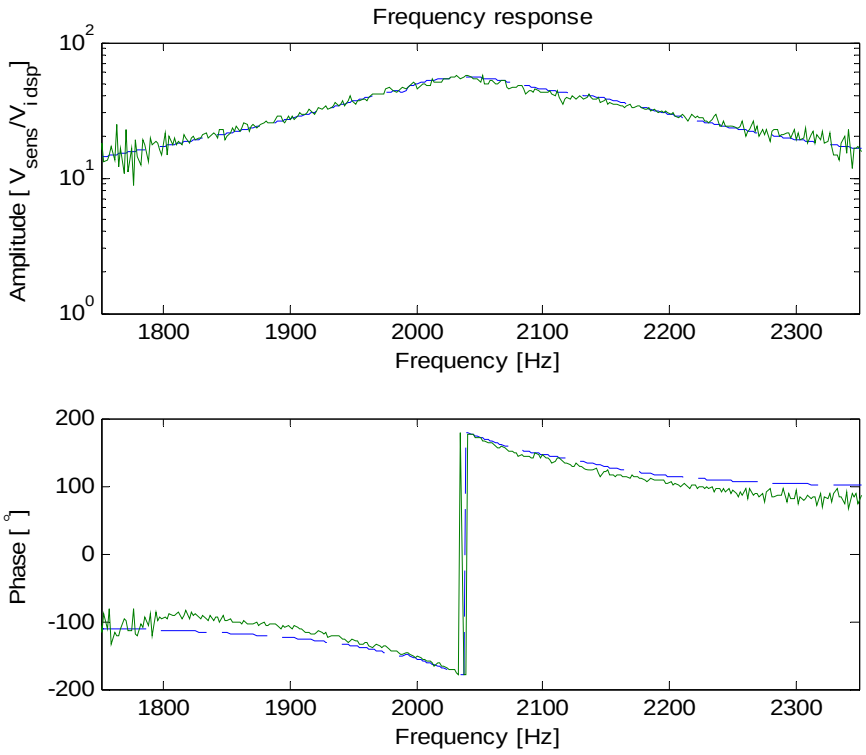

Figure 4.11: FRFs for the narrow band SISO model of the open loop forward path (dashed) and input-output measurements of the same path (solid) respectively, the input and output data being $V_{i\ dsp}$ and V_{sens} respectively.

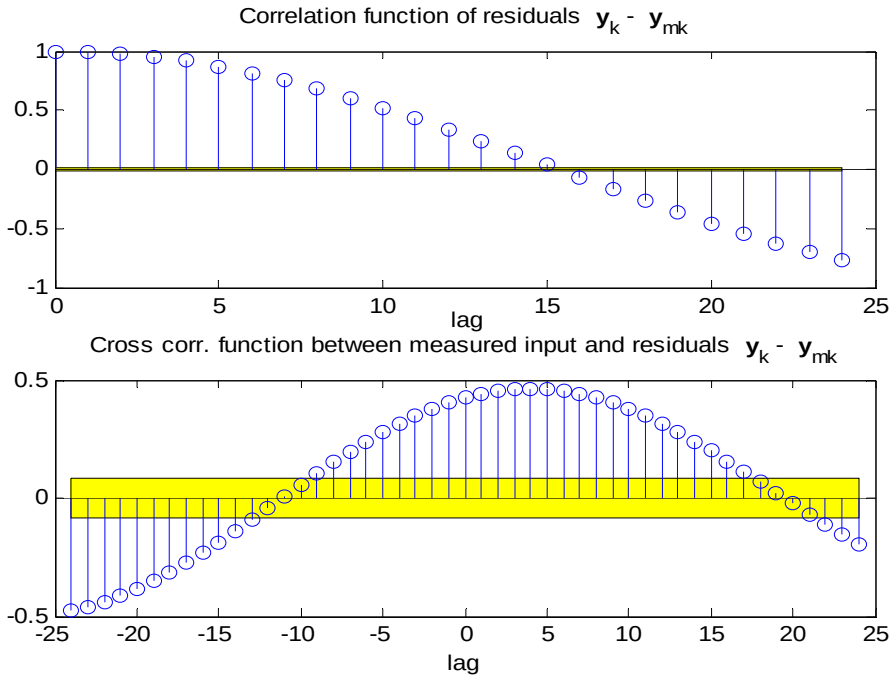

Figure 4.12: Auto correlation (upper graph) of residuals and cross correlation (lower graph) of input and residuals of measured data and forward path model.

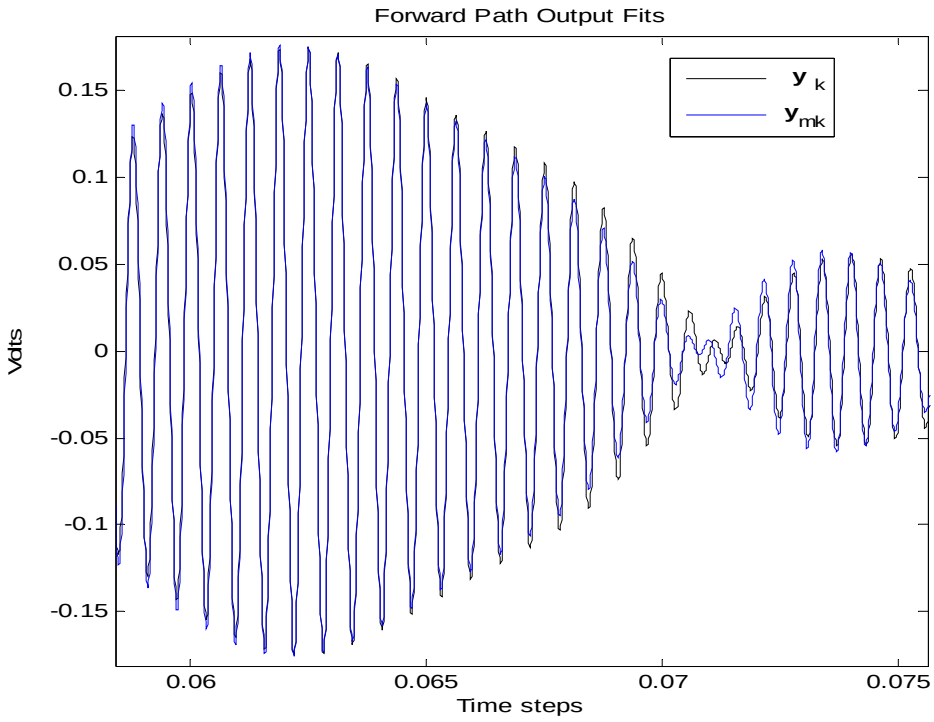

Figure 4.13: Comparison of measured data and time domain simulation of forward path model with 86% fit.

4.3.3.2. Control algorithm

During the implementation of the control algorithm on the DSP the relationship of the DSP input and output signals to the equivalent ones in Figure 4.6 are $V_{sens} = e_k$ and $V_{i1} = u_k + n_k$. An adaptive FIR-filter, $W(z)$, determines the control action in the system as shown in Figure 4.6. The filtered-x LMS algorithm indicated in the diagram as the LMS-block in turn determines its coefficients. The algorithm is derived from the minimization of the expected value of the squared error, i.e. of the cost function

$$J(w_i) = E\left[\boldsymbol{e}'_k \boldsymbol{e}'^{\boldsymbol{T}}_k\right], \tag{4.25}$$

by searching for appropriate w_i which are the coefficients for the adaptive filter $W(z)$. This minimization of $\boldsymbol{e}'_k$ means a minimization of $\boldsymbol{e}_k$. Physically this means that the resultant displacement at node 2 (see Figure 4.1) caused by the cutting force acting at node 1 and the force exerted by the actuator on the tool holder structure, is reduced. This is due to the

minimized SSA tip displacement proportional to $\boldsymbol{e}_k$**.** The choice of $\boldsymbol{d}'_{k-1}$ as the reference signal instead of $\boldsymbol{e}_{k-1}$ is due to the fact that the reference signal should provide advance information about the primary noise, before it appears at the point of cancellation, which is the actuator/tool holder point of contact, node 2. In the case of a turning process the primary noise is the tool holder deflection due to the cutting process. A delayed disturbance as reference signal more effectively provides advance information than a delayed error signal. It is for this reason that the adaptive feedback noise control (AFANC) algorithm suggested in Kuo et al. (2003) was preferred above the delayed error active noise algorithm as used by Andren et al. (2003). Here $\boldsymbol{e}_k$ was first pre-filtered by the denominator dynamics of the forward path, $1 - G^*(z)$ to cancel its poles and prevent them from participating in the calculation of the coefficients, w_i. This technique originates from Vipperman et al. (1993). The pre-filtered error signal $\boldsymbol{e}_k$ is denoted as $\boldsymbol{e}'_k$, where

$$\boldsymbol{e}_k = \boldsymbol{d}_k + T_f(z)(\boldsymbol{u}_k + \boldsymbol{n}_k)\ . \tag{4.26}$$

Then, with $\boldsymbol{n}_k$ neglected, $\boldsymbol{e}'_k$, is constructed as

$$\boldsymbol{e}'_k = \boldsymbol{d}'_k + (1 - G^*(z))T_f^*(z)W(z)\boldsymbol{x}_k = \boldsymbol{d}'_k + C^*(z)W(z)\boldsymbol{d}'_{k-1} \tag{4.27}$$

where $G^*(z)$, $T_f^*(z)$ and $C^*(z)$ are estimates of $G(z)$, $T_f(z)$ and $C(z)$respectively.

In this work the objective was to directly keep the plant output zero. According to (4.27) the error $\boldsymbol{e}'_k$ then becomes

$$\boldsymbol{e}'_k = \boldsymbol{d}'_k\ . \tag{4.28}$$

A gradient descent algorithm is then used to update all the adaptive filter coefficients for the next time step, which is

$$\boldsymbol{w}_{k+1} = \boldsymbol{w}_k - \mu\frac{\partial J}{\partial \boldsymbol{w}_k} \tag{4.29}$$

where

$$\frac{\partial J}{\partial \boldsymbol{w}_k} = 2\boldsymbol{e}'_k\frac{\partial \boldsymbol{e}'_k}{\partial \boldsymbol{w}_k}\ . \tag{4.30}$$

The final updating equation for the coefficients w_i , with $i = 1,2 \ldots L$ and L the length of filter $W(z)$, becomes

$$\boldsymbol{w}_{k+1} = \gamma\, \boldsymbol{w}_k - \alpha\, \boldsymbol{e}'_k C^*(z) \boldsymbol{d}'_{k-1}. \tag{4.31}$$

(4.30) is also known as the filtered-x LMS algorithm because the feedback type reference signal, $\boldsymbol{x}_k = \boldsymbol{d}'_{k-1}$, is filtered by the FIR filter $C^*(z)$ and becomes the gradient of the algorithm. The leakage coefficient γ is here assigned the value 0.99. In Andren et al. (2003) it is said to improve the systems robustness. The coefficient $\alpha = 2\mu$ is a convergence coefficient as found in Elliott (2001:78,82). It is determined by

$$\alpha = \frac{\tilde{\alpha}}{L\overline{\boldsymbol{x}'^{\,2}_k}} \tag{4.32}$$

where $\overline{\boldsymbol{x}'^{\,2}_k}$ is the mean-square of the filtered reference signal, $\boldsymbol{x}_k$. According to Elliott (2001:82), $\tilde{\alpha}$ should be

$$0 < \tilde{\alpha} < 2\,. \tag{4.33}$$

It was chosen as $\tilde{\alpha} = 0.02$ in this work, since lower values for a convergence coefficient are recommended for models that do not have an exact fit.

4.4. RESULTS AND DISCUSSION

4.4.1. Results

V_{sens} has a frequency dependent proportionality to mechanical strain of the SSA. The power spectral densities of V_{sens} with and without control for the 100 Hz and 200 Hz test signal cases are shown in Figures 4.14 and 4.15 respectively. Table 4.3 also includes the percentage attenuation of the maximum magnitude of V_{sens}. This reduction is achieved at the first bending mode at 2050 Hz. The forces measured by the force transducer remained constant for the tests whether with or without controller. For the 100 Hz- and 200 Hz-bandwidth cases the measured forces at the first bending mode frequency were 1.03 and 0.97 N respectively.

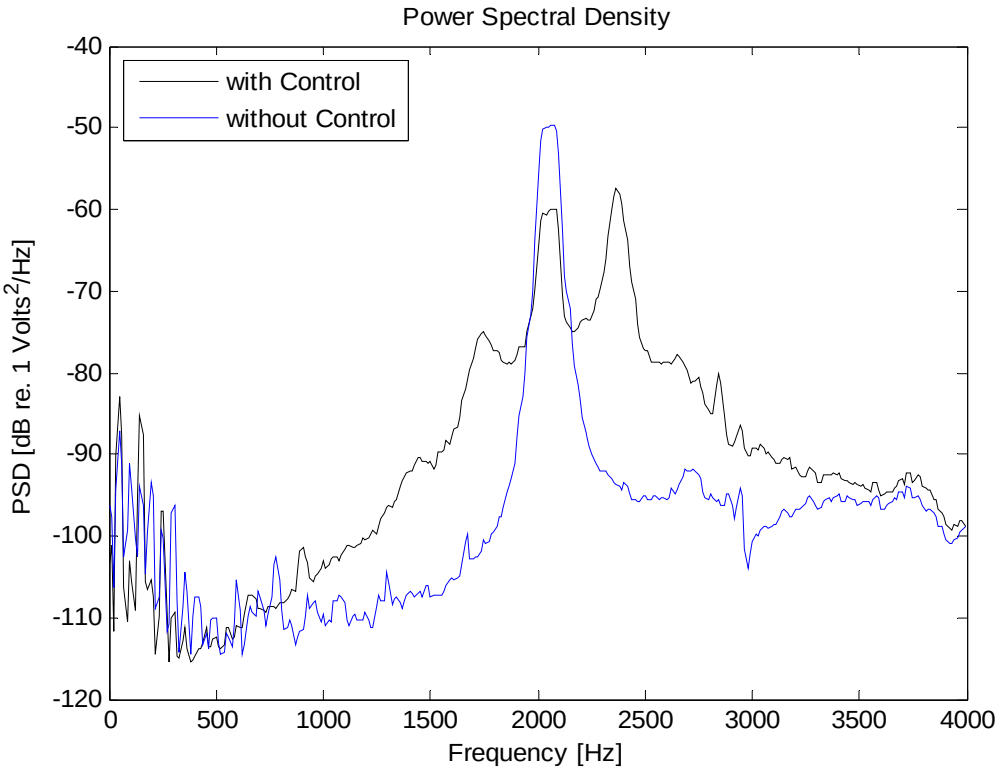

Figure 4.14: PSD of V_{sens} with and without control respectively for a 100 Hz bandwidth signal with 2050 Hz centre frequency to shaker.

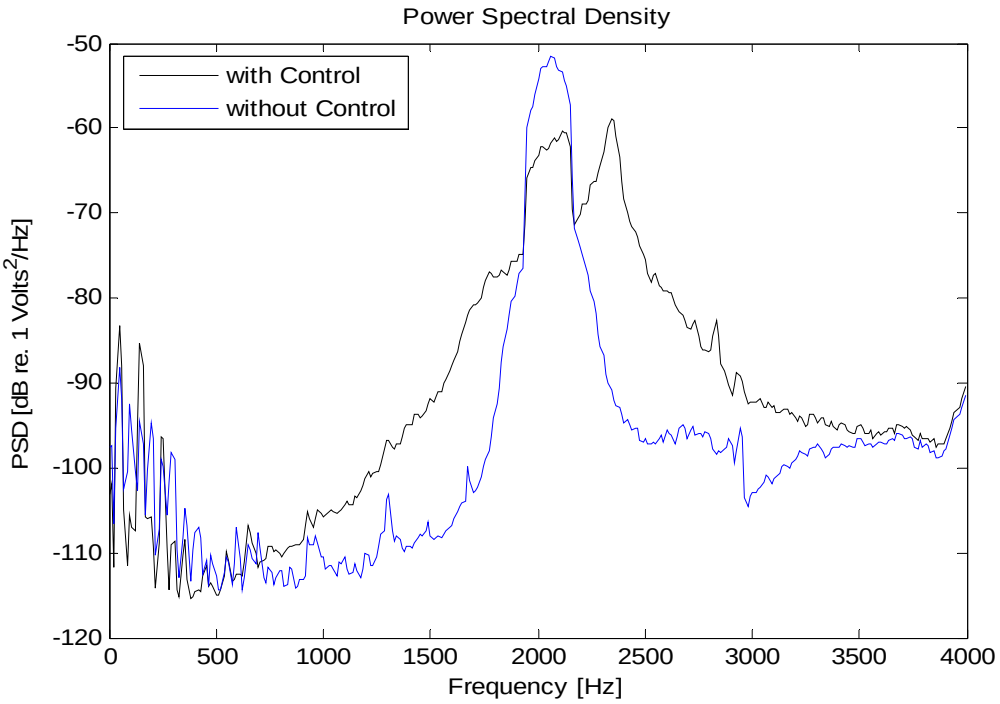

Figure 4.15: PSD of V_{sens} with and without control respectively for a 200 Hz bandwidth signal with 2050 Hz centre frequency to shaker.

Table 4.3: Results: Effects of control for two test signals to shaker

Bandwidth of representative force signal to shaker	Strain proportional amplitude of signal sensed by SSA at modal frequency	Amplitude in [N] of force applied to tip of representative tool holder at node 1	
	Maximum amplitude attenuation [%]	Without control	With control
100 Hz	70	1.03	1.03
200 Hz	65	0.97	0.97

For an input signal amplitude of $2V$ peak-to-peak applied to the shaker amplifier PA 100E (volume dial set to 95% of its range) a signal-to-noise-ratio (SNR) of roughly $20\,dB$ was obtained for the sensed signal, V_{sens}. Figure 4.16 shows a time domain segment of a $2050\,Hz$ sinusoid input signal to the shaker amplifier PA 100E and the signal V_{sens} then sensed by the sensing circuit. From this graph one can measure that the SNR of the feedback path of the vibration control system is approximately $20\,dB$ as mentioned above. Table 4.4 provides values from literature as reference for the SNR measured with the sensing circuit of this work.

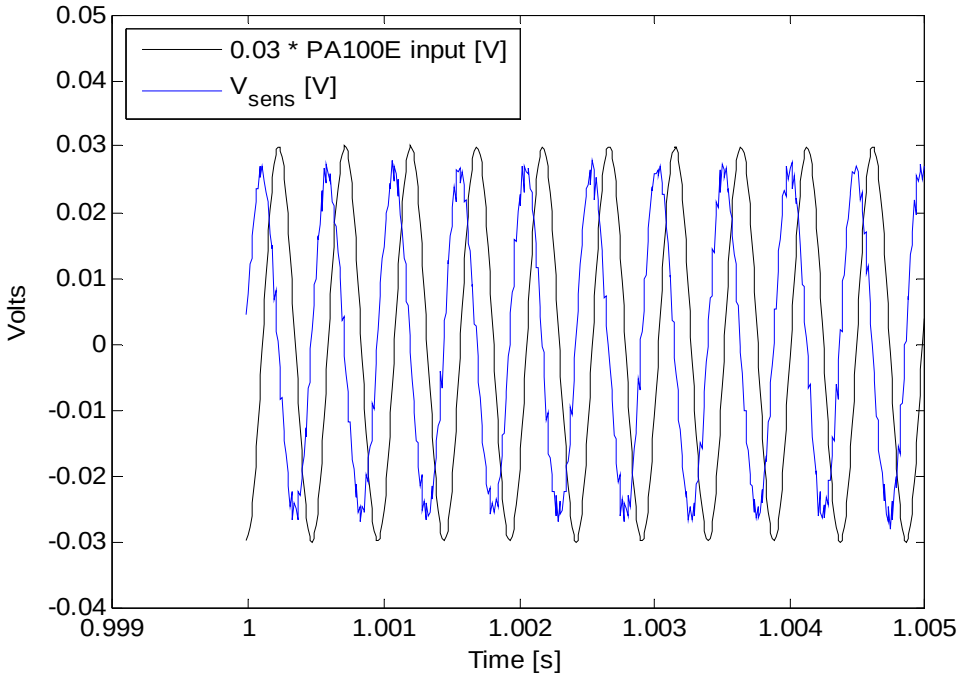

Figure 4.16: Time domain measurements of PA 100E amplifier input signal, and SSA sensed signal, V_{sens}.

Table 4.4: Feedback path SNR values in comparison with literature

	Measured SNR: SSA integrated in SC	Sufficient lower bound SNR for stabilization: Marginally stable feedback control system with output variance ranging from 0.3 to 0.8 by graphs in Rojas (2015:1131)	Minimum required SNR: Feedback path consisting of communication channels between plant and master station from Jović (1986:367)
SNR [dB]	≥ 20	10 to 0	4.0

4.4.2. Discussion

An indication of the performance of the control system in this work can also be obtained by comparing it to results from a desktop PC simulation under ideal conditions. This means that the fit of the forward path model was 100% and bidirectional positive form locking was assumed for the connection between the actuator and the tool holder. Bidirectional positive form locking means that the actuator could exert a force on the tool holder by both extension and contraction due to its interlocking with the tool holder. With this simulation an attenuation of 93 % was achieved.

This shows the need for bidirectional positive form locking at the actuator-tool holder connection and also for model accuracy. The results in section 4.4.1 indicate that a control system performance, not much lower than the abovementioned simulation results was however achievable. This was possible even with limited model accuracy and only unidirectional positive form locking.

Three more points need to be made respectively to the role of the sensing circuit SNR, the reaction of the SSA and bandwidth outlook. These add further meaning to the results.

It should be taken into consideration that the input signal in Figure 4.16 is the shaker amplifier input signal and not the output signal, i.e. force signal directly applied to the tool holder substitute. This means that one may regard this SNR value as a minimum if some of the noise imposed by the shaker amplifier would be deducted from the noise seen in V_{sens} in Figure 4.16. The SNR range obtained by Rojas (2015:1131) in Table 4.4 can be given in comparison to the SNR obtained. In his work a prediction of the sufficient lower SNR bound for stabilizing an unstable plant through feedback control via communication channel was

given. For the feedback path (i.e. between plant and controller) from marginally stable plants such SNR bound ranged from 10 to 0 dB for the variance values of the plant output ranging from 0.3 to 8. Also listed in Table 4.4 is the SNR that Jović (1986:367) suggests. According to that literature source, the minimum required SNR be 4 dB in process control, inclusive of the feedback path for communication channels between a plant and master station.

The sensed forces for each bandwidth case remained at the same level with or without control. As a result of control however the displacement of the node of contact between the SSA and the tool holder substitute was attenuated. This means that the SSA has reacted with increased stiffness variations to the variations of the input disturbance force. The latter was found to be downscaled to approximately 25% of the tangential force's dynamic component in a hard turning example in Scheffer et al. (2003).

The achieved attenuation is for a narrow band model of the tool holder substitute. This was done to get a first picture of using an SSA for a situation representative to a turning process. If the band pass filter at the exit of the sensing circuit is omitted, phase loss will be less and identification of a model for a wider bandwidth which is minimum phase is more likely.

4.5. CONCLUSION

A simple and stable system is needed to curb tool vibration in turning processes. Both requirements are met by using a self-sensing actuator (SSA). It offers the simplicity of sensing and actuation combined in a single system. The proof of concept of this part of the work is the control of tool vibrations by means of a SSA and active control algorithm. The control system was implemented as a hardware building block with an integrated SSA and software building block.

The suggested method has shown with success that these building blocks could function in a complete system. It includes all the modules that would be needed for active control of tool vibrations in a real turning process in which the narrow band model could be extended to a broad band model. The signal-to-noise-ratio that was achieved for the sensing circuit allowed the SSA strain proportional signal to be used as control system feedback signal. Form locking at the contact of the SSA with the representative tool holder was such that the actuator was restricted to counteract vibrations mainly by extension. This was due to the

shaker's capability to provide a force input around zero mean but not non-zero mean, which would be the case during turning. The objective of active tool vibration control was however reached with a performance of 65% and 70% attenuation. It was measured for downscaled force excitation to the structure within $200Hz$ and $100Hz$ bandwidths around the representative tool holders bending mode. Regarding the linearization of the hysteretic actuator it was found that the current in the actuator is lagging the voltage input to the driving amplifier by little such that sufficient support of linearity could be assumed. Pseudorandom noise however was imposed on the actuation signal to further enhance linearity of the SSA.

CHAPTER 5

CONCLUSIONS AND RECOMMENDATIONS

This chapter compares the research objectives that were aimed at in chapter 1 to the stages that this work reached and the gains that it brought forth. It also points out the limitations and briefly discusses recommendations for further research.

5.1 CONCLUSIONS

The conclusions are encompassing the research of utilization of a self-sensing actuator for tool vibration control and tool condition monitoring. These are therefore looked at from the following perspectives:

i. the control algorithm
ii. the tool condition monitoring aspect
iii. proof of concept
iv. concept generality
v. stage of prototype system

5.1.1 Control algorithm

It was clear from the start of this work that a piezoelectric element would be used as an actuator. The basis for that choice was its ability to function as actuator and sensor at the same time, an idea that was obtained from Dosch et al. (1992). In their work the sensing ability of the piezoelectric element was used to provide the feedback signal in an active vibration control system. The control system that was therefore opted for in this work was based on the filtered-x least mean square (FXLMS) algorithm used by Andren et al. (2003). With methods on infinite impulse response (IIR) filter to finite impulse response (FIR) filter conversion not included in the scope of this study, it was decided instead to use a pre-filtering technique suggested by Vipperman et al. (1993). This would enable the use of IIR filters to represent the transfer behaviour between the controller output variable and the strain proportional signal from the sensing circuit as output of the control system. This option was accepted for the first part of the work which was a simulation of the control system in the case of

using a self-sensing actuator. A 93 % reduction of the r.m.s. value from turning process extracted tool vibrations was achieved.

5.1.2 The tool condition monitoring (TCM) aspect

A long term goal of this project is simultaneous tool vibration control and TCM. This would be realized using a self-sensing actuator (SSA). Since a piezoelectric stack actuator was looked at in the active control part of this work, the objective was to find out how well would a SSA perform in TCM. It was compared to a reference TCM method from existing literature (Scheffer et al., 2003). The hypothesis tested therefore was whether the difference between the investigated case of using a SSA and a reference TCM case would lie outside a pre-determined interval. If it would lie outside the interval, the difference would have been too significant. The test showed that the difference was insignificant with a probability of 95 % and that a unidirectional sensing SSA can be used for this purpose.

5.1.3 Proof of concept

The industrial situation that was envisaged when testing the principle of a SSA was that of a turning process. The force that was applied to a substitute tool holder was a downscaled narrowband representation of a previously measured cutting force that results from the tool-work-piece-interaction. In this test the complete system including the DSP-embedded control algorithm and sensing circuit was involved as it could be applied to a practical turning process with some modifications. This distinguishes this particular proof-of-concept from that shown in Anderson et al. (1994) and also in Dosch et al. (1992) as it is an extension of the latter and more application specific. The results show that tool vibrations captured in the form of a strain proportional signal by means of the SSA were attenuated by up to 70 % at the bending mode frequency when the substitute tool holder was excited by a downscaled 100 Hz bandwidth force signal. Attached to these results were limitations. The first limitation was that a test of only a narrow band force signal was conducted, since the forward path model was identified for narrowband accuracy only. Secondly the force signal was downscaled to $2\,N$ peak-to-peak bipolar to zero mean from typically $8\,N$ peak-to-peak for the dynamic component of the tangential cutting force which is bipolar with respect to the non-zero mean. Downscaling poses a limitation and was dictated by the capacity of the shaker and also the inability of the shaker to exert forces with non-zero mean, which would put a constant pressure on the SSA. It would then allow the SSA to respond with pushing forces only in the absence of positive form locking between the SSA and the tool holder substitute.

5.1.4 Concept generality

First steps were taken to apply a self-sensing actuator (SSA) in the field of machining. This has value for the manufacturing industry where active vibration control is needed. As piezoelectric actuators are already used in active control of structures (Preumont, 2002:282), the SSA also finds application in their control as Anderson et al. (1994) showed. The concept of a SSA and an appropriate control algorithm combined therefore has a value of generality in applications. Such they have since they allow simpler control system design in every application that requires structural stiffness without adding excessive structural weight to achieve this stiffness.

5.1.5 Prototype system

As mentioned in section 5.1.3 the control system using a SSA has been taken to a stage where it includes all the modules that would be used in a tool vibration control system for a turning process. The doubt that noise would inhibit the sensing function of the SSA is cleared. This can be said since a significant signal-to-noise ratio (SNR) of 20 dB was registered at the SSA's sensing of strain resulting even from downscaled forces to which a substitute tool holder was exposed. Practical and simulation based evidence was collected that this system could perform simultaneous the two functions of active tool vibration control and tool condition monitoring. It must be stated that the TCM function of the SSA was so far based on simulation with a reconstructed dynamic cutting force exerted on a finite element model of a SSA equipped tool holder.

The main modules belonging to the prototype stage of this work are the digital signal processor (DSP) with its embedded control algorithm, the driving amplifier and the sensing circuit including the SSA. The difference to a final product is that the actuator was positioned in contact with the tool holder yet external instead of being embedded as in the work of Andren et al. (2003). Further research on improving the prototype and exposing it to forces from a type of shaker that is capable of exerting forces around a non-zero mean can be conducted based on the prototype platform now available.

5.2 RECOMMENDATIONS

Based on the studies that this report comprises not only did it become clear what potential it holds for industrial application but also what current limitations there are to solve before this can happen. As a

result of what was encountered as limitations the following recommendations can be made for further projects. Several recommendations can be combined to constitute a project.

i. For bringing the proof of concept experiment another step closer to a real turning process situation one should apply a unipolar pressure force to the substitute tool holder. This means that it should vary around a non-zero mean and not change sign. A way to do this was not available at first glance neither was a shaker capable to do this. Simply applying a pre-stress between the substitute tool holder and the SSA will not be the answer because the shaker will just add its bipolar force to the force already exerted to bend the tool holder. This however will still allow loss of contact between the tool holder and the SSA.

ii. In the current proof of concept setup the contact of the SSA with the substitute tool holder is a spherical against a flat surface. This contact prevents damage to the SSA which may be caused by canter if the surfaces of contact were both flat and not mating properly. With either of such contacts however only pushing forces can be exerted in the absence of positive form locking. It is thus recommended that a connection be designed that would enable the SSA to also exert pulling forces onto the substitute tool holder but does not allow moments to be transferred to the SSA.

iii. The existing identified model for the forward path is a narrowband model. This was decided on after system identification (SID) attempts to estimate over a wide bandwidth, e.g. 0 to $3000\,Hz$ resulted in models having zeros outside the discrete z-domain unit circle. These non-minimum phase zeros are presumably a result of the band pass filter at the output side of the sensing circuit. This filter and the gain adjustment just before the band pass filter introduce considerable phase loss. It is therefore recommended that in order to identify a wide band model one should omit these last two stages at the sensing circuit output. The exact link between non-minimum phase zeros and excessive phase loss, i.e. lag, was not investigated in this work. So far it was only found that there is a possibility that excessive lag may result in the estimated model having non-minimum-phase zeros. Since the adaptive feedback active noise control (AFANC) algorithm has the ability to control broadband vibrations another incentive exists to consider a wideband SID model for the forward path.

iv. In this study no effort was made to look into the use of finite impulse response (FIR) instead of infinite impulse response (IIR) as filter structure for the forward path. Researchers such as Andren et al. (2003:869) make use of up to 16 tap FIR filters to represent the forward path. It is therefore recommended to search for a numerical method which can convert IIR to FIR filters. One of the methods presented in Dehkordi & Aghdam (2005) may be of assistance to do such conversion.

v. In order to improve the linearization of the hysteretic nature of the piezoelectric actuator it is recommended that more attention be given to one of the considerations for linearization in chapter 4. Moheimani et al. (2006:214) suggests that voltage tracking of the current through the piezoelectric actuator improves linearization. The available setup should therefore be complemented with a phase shifter. This will cause the voltage difference over the shunt on the high voltage side of the piezoelectric actuator to lead the amplifier input voltage. It should lead by 90° over the entire bandwidth of the vibration control system.

BIBLIOGRAPHY

Abouletta, O.B. & Mádl, J. (2001). Surface roughness prediction based on cutting parameters and tool vibrations in turning operations. *Journal of Materials Processing Technology*, 118(1-3), 269-277.

Anderson, E.H. & Hagood, N.W. (1994). Simultaneous piezoelectric sensing/actuation: analysis and application to controlled structures. *Journal of Sound and Vibration,* 174(5):617-639.

Andrén, L., Håkansson, L. & Claesson, I. (2003). Active control of machine tool vibrations in external turning operations. *Proceedings of the Institution of Mechanical Engineers, Part B: Journal of Engineering Manufacture*, 217(6), 869-872.

Andrén, L., Håkansson, L., Brandt, A. & Claesson, I. (2004a). Identification of dynamic properties of boring bar vibrations in a continuous boring operation. *Mechanical Systems and Signal Processing*, 18, 869–901.

Andrén, L., Håkansson, L., Brandt, A. & Claesson, I. (2004b). Identification of motion of cutting tool vibration in a continuous boring operation—correlation to structural properties. *Mechanical Systems and Signal Processing*, 18, 903–927.

Audy, J. (2006), An appraisal of techniques and equipment for cutting force measurement. *Journal of Zhejiang University – Science* A 7 (11), 1781-1789.

Balmès, E. & Leclère, J.-M. (2003), *Structure dynamics toolbox, for use with MATLAB®*, SDTools, User's Guide Version 5.1

Bahre, D., Rosenberger, U. & Warnecke, G. (1992). Monitoring of cutting processes by vibration analysis: exemplary applications in grinding and turning processes. *Sensors and Signal Processing for Manufacturing; ASME, Production Engineering Division (Publication)* PED 55:65-80.

Bayerle, K.-H. http://www.bay-hv-plasma-piezo.de/kontakt/ . Personal communication; 19.01.2015.

Berman, H. (2016). *Stat Trek*, http://stattrek.com/Tables/t.aspx

Bonifacio, M.E.R. & Diniz, A.E. (1994), Correlating tool wear, tool life, surface roughness and tool vibration in finish turning with coated carbide tools. *Wear*, 173(1-2): 137-144.

Bukkapatnam, S. & Fofana, M.S. (2001). Analysis of degenerate bifurcation in machining using a nonlinear model. *Proceedings of the ASME Design Engineering Technical Conference*, 6C:2371-2388.

Bukkapatnam, S.T., Lakhtakia, A. & Kumara, S.R. (1995). The concept of chaos theory based optimal cutting tool chatter control. *Proceedings of SPIE, The International Society for Optical Engineering*, 2595:2-10.

Chassaing, R. (2005). *Digital signal processing and applications with the C6713 and C6416 DSK*, John Wiley & Sons, Inc.

Chen, S.-G., Ulsoy, A.G. & Koren, Y. (1993). Computational stability analysis of chatter in turning. *ASME Dynamic System Control Division Publications*, 50:107-111.

Cheung, C.F. & Lee, W.B. (2000). Theoretical and experimental investigation of surface roughness formation in ultra-precision diamond turning. *International Journal of Machine Tools &Manufacture*, 40(7), 979-1002.

Chiou, R.Y.S. & Liang, S.Y. (1999). Chatter frequency in turning considering tool compliance and wearland. *Journal of Manufacturing Science and Engineering, Transactions of the ASME*. 121(2):307-311.

Chiou, R.Y. & Liang, S.Y. (2000). Analysis of acoustic emission in chatter vibration with tool wear effect in turning. *International Journal of Machine Tools and Manufacture*, 40(7), 927-941.

Choudhury, S.K. & Bartarya, G. (2003). Role of temperature and surface finish in predicting tool wear using neural network and design of experiments. *International Journal of Machine Tools & Manufacture*, 43, 747-753.

Cho, D.-W., Lee, S.J. & Chu, C. N. (1999). The state of machining process monitoring research in Korea. *International Journal of Machine Tools & Manufacture*, 39:1697-1715.

Dehkordi, V.R. & Aghdam, A.G. (2005). A computationally efficient algorithm for order-reduction of IIR-filters using control techniques. *Proceedings of the 2005 IEEE Conference on Control Applications Toronto, Canada, August 28-31, 2005.*

Del Pino, S. & Pironneau, O. (2008). FreeFEM3D Documentation, Version 1.0pre11, http://www.freefem.org , 3.5.2012.

Deshpande, N. & Fofana, M.S. (2001). Nonlinear regenerative chatter in turning. *Robotics and Computer-Integrated Manufacturing*, 17(1-2):107-112.

Dimla Snr., D.E. (2000). Sensor signals for tool-wear monitoring in metal cutting operations- a review of methods. *International Journal of Machine Tools & Manufacture*, 40:1073-1098.

Doi, S. & Kato, S. (1956). Chatter vibration of lathe tools. *Transactions of the ASME*, 78:1127-1134.

Dorf, R.C. & Bishop, R.H. (2005). *Modern control systems*, 10th Edition, Pearson Education, Inc., Upper Saddle River, New Jersey.

Dosch, J.J. & Inman, D.J. (1992). A self-sensing piezoelectric actuator for collocated control. *Journal of Intelligent Material Systems and Structures*, 3:166-185.

Elliott, S.J. (2001). *Signal processing for active control*. London: Academic Press Limited.

Fabris, N.S. & D'Souza, A.F. (1974). Nonlinear stability analysis of chatter in metal cutting. *Journal of Engineering for Industry, Transactions of the ASME*. 96:670:675.

Fawcett, S.C. (1990). Small amplitude vibration compensation for precision diamond turning. *Precision Engineering*, 12(2):91-96.

Föllinger, O. (1990). *Regelungstechnik*. Hüthig Buch Verlag GmbH, Heidelberg.

Frey, P.J. (2001). MEDIT: An interactive visualization software, *Institut National de Recherche en Informatique et en Automatique*, Rapport Technique No 0253, Thème 4.

Freyer, B.H., Theron, N.J. & Heyns, P.S. (2008). Simulation of tool vibration control in turning, using a self-sensing actuator, *Journal of Vibration and Control*, 14(7), 999-1019.

Freyer, B.H., Heyns, P.S. & Theron N.J. (2014). Comparing orthogonal force and unidirectional strain component processing for tool condition monitoring, *Journal of Intelligent Manufacturing*, 25:473-487.

Freyer, B.H., Theron, N.J., Heyns, P.S. & Pickelmann, L. (2016). Active control of tool vibrations using a self-sensing actuator, *Mechatronics*, submitted 18.12.2015.

Fuller, C.R., Elliott, S.J. & Nelson, P.A. (1996). *Active control of vibration*. London: Academic Press Limited.

Gajate, A. , Haber, R., del Toro, R., Vega, & Bustillo, A. (2012). Tool wear monitoring using neuro-fuzzy techniques a comparative study in a turning process, *Journal of Intelligent Manufacturing*, 23:869–882.

Gasparetto, A. (1998). System theory approach to mode coupling chatter in machining. *Journal of Dynamic Systems, Measurement and Control, Transactions of the ASME*, 120(4):545-547.

Geuzaine, C. & Remacle, J.-F. (2009). Gmsh: a three-dimensional finite element mesh generator with built-in pre- and post-processing facilities. *International Journal for Numerical Methods in Engineering*, 79, (11), 1309-1331, http://geuz.org/gmsh/ , 3.5.2012.

Heimann, B., Gerth, W. & Popp, K. (2001). *Mechatronik*. Munich: Fachbuchverlag Leipzig im Carl Hanser Verlag.

Horowitz, P. & Winfield, H. (1989). *The art of electronics*. Second edition. Cambridge: University Press. (pg 277)

Isermann, R. (1996). Towards intelligent mechatronic systems. *Research in Engineering Design.*8(3):139:150.

Jackson, J.E. (1991). *A user's guide to principal components*, John Wiley & Sons Ltd, New York.

Jemielniak, K. & Widota, A. (1989). Numerical simulation of non-linear chatter vibration in turning. *International Journal of Machine Tools and Manufacture*, 29(2):239-247.

Jović, F. (1986). *Process control systems: principles of design and operation*. London: Kogan Page Ltd.

Kaneko, T., Sato, H., Tani, Y. & O-hori, M. (1984). Self-excited chatter and its marks in turning. *Journal of Engineering for Industry, Transactions of the ASME*. 106:222-228.

Koenigsberger, F. (1964). *Design principles of metal - cutting machine tools*, New York: Pergamon Press Limited.

Kuo, S.M., Kong, X. and Gan, W.S. (2003). Applications of adaptive feedback active noise control system, *IEEE Transactions on Control System Technology*, 11(2):216–220.

Kuo, S.M. & Morgan, D.R. (1996). *Active noise control systems.* New York: John Wiley & Sons, Inc.

Lai, H.-Y. (1987). Nonlinear adaptive modelling for machining chatter identification and monitoring. *ASME, Design and Engineering Division (Publication) DE*, 7:181-187.

Landers, R.G. & Ulsoy, A.G. (1996). Machining force control including static, nonlinear effects. *Proceedings of the Japan/USA Symposium on Flexible Automation*, 2:983-990.

Lee, E.C., Nian, C.Y. & Tarng, Y.S. (2001). Design of a dynamic vibration absorber against vibrations in turning operations. *Journal of Materials Processing Technology*, 108(3):278-285.

Li, C.-J. & Ulsoy, A.G. (1999). Precision measurement of tool-tip displacement using strain gages in precision flexible line boring. *American Society of Mechanical Engineers*, Dynamic Systems and Control Division (Publication) DSC 67 743-751.

Li, X.Q., Wong, Y.S. & Nee, A.Y.C. (1997). Tool wear and chatter detection using the coherence function of two crossed accelerations. *International Journal of Machine Tools and Manufacture*, 37(4):425-435.

Liu, Q. & Altintas, Y. (1998). On-line monitoring of flank wear in turning with multi-layered feed-forward neural network. *International Journal of Machine Tools & Manufacture*, 39:1945-1959.

Ljung, L. (1987). *System identification – Theory for the user*. Prentice-Hall Inc., Englewood Cliffs, New Jersey.

Lundholm, T., Yngen, M. & Lindström, B. (1988). Advanced process monitoring – a major step towards adaptive control. *Robotics and Computer- Integrated Manufacturing*, 4(3-4), 413-421.

Lutz, H. & Wendt, W. (2002). Taschenbuch der Regelungstechnik. Verlag Harri Deutsch, Frankfurt am Main.

Marui, E., Ema, S. & Kato, S. (1983). Chatter vibration of lathe tools. Part 2: On the mechanism of exciting energy supply. *Transactions of the ASME, Journal of Engineering for Industry*. 105:107:113.

MATLAB Version 6.5.1 (2003a), computer software, The Mathworks Inc., Natick Massachusetts. Control System Toolbox. Version 5.2.1.

MATLAB Version 6.5.1 (2003b), computer software, The Mathworks Inc., Natick Massachusetts. Matlab. Version 6.5.1.

MATLAB Version 6.5.1 (2003c), computer software, The Mathworks Inc., Natick Massachusetts. Neural Network Toolbox. Version 4.0.2.

MATLAB Version 6.5.1 (2003d), computer software, The Mathworks Inc., Natick Massachusetts. Statistics Toolbox. Version 4.1.

MATLAB Version 7.3 (2006a), computer software, The Mathworks Inc., Natick Massachusetts. Wavelet Toolbox. Version 3.1.

MATLAB Version 7.3 (2006b), computer software, The Mathworks Inc., Natick Massachusetts. Matlab. Version 7.3.

MATLAB Version 7.3 (2006c), computer software, The Mathworks Inc., Natick Massachusetts. Simulink. Version 6.5.

MATLAB Version 7.3 (2006d), computer software, The Mathworks Inc., Natick Massachusetts. Embedded Target for TI C6000 DSP(tm). Version 3.1.

MATLAB Version 7.3 (2006e), computer software, The Mathworks Inc., Natick Massachusetts. Link for Code Composer Studio. Version 2.1.

MATLAB Version 7.3 (2006f), computer software, The Mathworks Inc., Natick Massachusetts. Real-Time Workshop. Version 6.5.

MATLAB Version 7.3 (2006g), computer software, The Mathworks Inc., Natick Massachusetts. Signal Processing Blockset. Version 6.4.

MATLAB Version 7.3 (2006h), computer software, The Mathworks Inc., Natick Massachusetts. Signal Processing Toolbox. Version 6.6.

MATLAB Version 7.5 (2007), computer software, The Mathworks Inc., Natick Massachusetts. System Identification Toolbox. Version 7.1.

Meirovitch, L. (2001). *Fundamentals of Vibrations*. Waveland Press, Inc., Long Grove, Illinois.

Millman, J. & Halkias, C.C. (1967). *Electronic devices and circuits*. New York: McGraw-Hill, Inc.

Mitsubishi (2007). General Catalogue 2007-2008. Mitsubishi Materials, C003B.

Murata, R. & Kokubo, K. (1994). Correlation between flank wear and tool vibration excited by a diagnostic impulse in machining process. *Journal of the Japan Society for Precision Engineering*. 60(2):250-254.

Moheimani, S.O.R. & Fleming, A.J. (2006). *Piezoelectric transducers for vibration control and damping*. London Limited: Springer-Verlag.

Pal, S., Heyns, P.S., Freyer, B. H., Theron, N.J. & Pal, S.K. (2011). Tool wear monitoring and selection of optimal cutting conditions with progressive tool wear effect and input uncertainties. *Journal of Intelligent Manufacturing*, 22(4), 491-504.

Pan, J. & Su, C.-Y. (2001). Modeling and chatter suppression with ultra-precision in dynamic turning metal cutting process.*Proceedings of the ASME Design Engineering Technical Conference*, Vol. 6 B, 1125-1132.

Pickelmann, L. (2010). *Piezomechanik GmbH*, http://www.piezomechanik.com/en/introduction .

Pisoni, A.C., Santolini, C., Hauf, D.E. & Dubowsky, S. (1995). Displacements in a vibrating body by strain gauge measurements. *Proceedings of the 13th International Modal Analysis Conference*, Nashville, TN, February.

Pratt, J.R. & Nayfeh, A.H. (1997). Boring-bar chatter control using a two-axes active vibration absorber scheme. *Proceedings – National Conference on Noise Control Engineering*, Vol. 2, 313-324.

Pratt, J.R. & Nayfeh, A.H. (1999). Design and modelling for chatter control. *Nonlinear Dynamics*, 19(1):49-69.

Preumont, A. (2002). *Vibration Control of Active Structures, an Introduction, 2nd Edition*. Dordrecht, The Netherlands: Kluwer Academic Publishers.

Purushothaman, S. (2010), Tool wear monitoring using artificial neural network based on extended Kalman filter weight updation with transformed input patterns. *Journal of Intelligent Manufacturing*, 21:717–730.
Rahman, M. & Ito, Y. (1985). Stability analysis of chatter vibration in turning processes. *Journal of Sound and Vibration*, 102(4):515-525.

Roddeck, W. (2003). *Einführung in die Mechatronik*. Stuttgart: B.G. Teubner GmbH.

Rojas, A.J. (2015). Step reference tracking in signal-to-noise ratio constrained feedback control. *International Journal of Control, Automation and Systems*,13(5):1131-1139.

Seah, K.H.W., Li, X. & Lee, K.S. (1995). The effect of applying coolant on tool wear in metal machining. *Journal of Materials Processing Technology,* 48, 495-501.

Scheffer, C., Kratz, H., Heyns, P.S., & Klocke, F. (2003). Development of a tool wear-monitoring system for hard turning. *International Journal of Machine Tools & Manufacture,* 43: 973-985.

Scheffer, C. & Heyns, P.S. (2004). An industrial tool wear-monitoring system for interrupted turning. *Mechanical Systems and Signal Processing,* 18, 1219-1242.

Sharma,V.S., Sharma, S.K. & Sharma, A.K. (2008). Cutting tool wear estimation for turning. *Journal of Intelligent Manufacturing*, 19:99–108.

Sick, B. (2002). On-line and indirect tool wear monitoring in turning with artificial neural networks: a review of more than a decade of research. *Mechanical Systems and Signal Processing*, 16(4):487-546.

Silva, R.G., Reuben, R.L., Baker, K.J. & Wilcox, S.J. (1998). Tool wear monitoring of turning operations by neural network and expert system classification of a feature set generated from multiple sensors. *Mechanical Systems and Signal Processing*, 12(2):319-332.

Skogestad, S. & Postlethwaite, I. (2001). *Multivariable Feedback Control: Analysis and Design*, John Wiley & Sons Ltd, Chichester, England.

Sturesson, P.-O.H., Hakansson, L. and Claesson, I. (1997). Identification of statistical properties of cutting tool vibrations in a continuous turning operation- correlation to structural properties. *Mechanical Systems and Signal Processing*, 11(3):459-489.

Swantek, S.D., Wicks, A.L. & Wilson, L.T. (2001). An optical method of strain measurement in the split Hopkinson pressure bar. *SEM Proceedings of the 19th International Modal Analysis Conference (IMAC XIX)*, Orlando, FL, USA, February 5-9.

Tarng, Y.S., Kao, J.Y. & Lee, E.C. (2000). Chatter suppression in turning operations with a tuned vibration absorber. *Journal of Materials Processing Technology*, 105(1-2), 55-60.

Texas Instruments (2006a). *16-bit, quad-channel ultra-low glitch, voltage output digital-to-analog converter* (Brochure). SLAS431B.

Texas Instruments (2006b). *DAC8554 EVM user's guide* (Brochure). SBAU121.

Texas Instruments (2007). *Dual, 500kSPS, 16-bit, 2+2 channel, simultaneous sampling analog-to-digital converter* (Brochure). SBAS230E.

Texas Instruments (2009). *5-6K interface board user's guide* (Brochure). SLAU104c.

Texas Instruments (2011). *ADS7861/8361/7863EVM user's guide* (Brochure). SLAU094a.

Tlusty, J. & Ismail, F. (1981). Basic non-linearity in machining chatter. *Annals of the CIRP*, 30(1).

Uchino, K. (1997). *Piezoelectric actuators and ultrasonic motors.* Boston/Dordrecht/London: Kluwer Academic Publishers.

Vipperman, J.S., Burdisso, R.A. & Fuller, C.R. (1993). Active control of broadband structural vibration using the LMS algorithm. *Journal of Sound and Vibration*, 166(2):283-299.

Wang, X., Wang, W., Huang,Y., Nguyen, N. & Krishnakumar, K. (2008). Design of neural network-based estimator for tool wear modeling in hard turning. *Journal of Intelligent Manufacturing*, 19:383–396.

Wickerhauser, M.V. (1994). *Adapted wavelet analysis from theory to software*. IEEE Press, Piscataway, New Jersey.

Widrow, B. & Stearns, S.D. (1985). *Adaptive signal processing*, Prentice Hall New York.

Wu, Y. & Du, R. (1996). Feature extraction and assessment using wavelet packets for monitoring of machining processes. *Mechanical Systems and Signal Processing*, 10(1), 29-53.

Xu, W.L. & Han, L. (1999). Piezoelectric actuator based active error compensation of precision machining. *Measurement Science and Technology*. 10: 106-111.

Yeh, L.-J. & Lai, G.-J. (1995). Study of the monitoring and suppression system for turning slender work pieces. *Proceedings of the Institution of Mechanical Engineers, Part B: Journal of Engineering Manufacture*, 209(B3), 227-236.

Appendix A

Sensitivity matrices

The sensitivity matrix A contains values that reflect the measured voltage of each of 3 strain gauge bridges in units of $[V/N]$.

$$\boldsymbol{v} = \boldsymbol{A}\,\boldsymbol{f} \tag{A.1}$$

where $\boldsymbol{f} = [F_x \quad F_y \quad F_z]^T$ is a vector of the tangential, feed and thrust forces respectively and $\boldsymbol{v}_k = [v_{1k} \quad v_{2k} \quad v_{3k}]^T$ is a vector of two half-bridges and a full-bridge measurement at time instant k for the x - , y- and z-directions respectively.

Three different load applications in each direction i resulted in three different voltages sensed by the strain gauge instrumented tool holder for each of j sensing bridges. From these $3 \times j$ measurements for every position in matrix $\boldsymbol{A}$, a sensitivity a_{ij} [V/N] was determined by averaging the three measurements.

The inverse of the sensitivity matrix is given in equations A.2 end A.3 for two different cases.

Case 1:

$$\boldsymbol{A}^{-1} = \begin{bmatrix} 1384.4 & -75.9 & 2200.8 \\ 22.7 & 815.5 & 3246.3 \\ -7.5 & -270.4 & 11180.0 \end{bmatrix} \tag{A.2}$$

Case 2:

$$\boldsymbol{A}^{-1} = \begin{bmatrix} 2.2490 & -0.4869 & 5.7344 \\ -0.0757 & 4.8532 & 8.6221 \\ -0.4578 & -1.8142 & 29.8754 \end{bmatrix} \tag{A.3}$$

Appendix B

Instrumented Tool Holder

Figure B.1 is showing the positions of strain gauges on the tool holder which was instrumented and mentioned in chapters 2 to 4. Type 1 and 2 were 1-XY31-6/120 and 1-LY41-3/120A types respectively from Hottinger Baldwin Messtechnik GmbH (HBM).

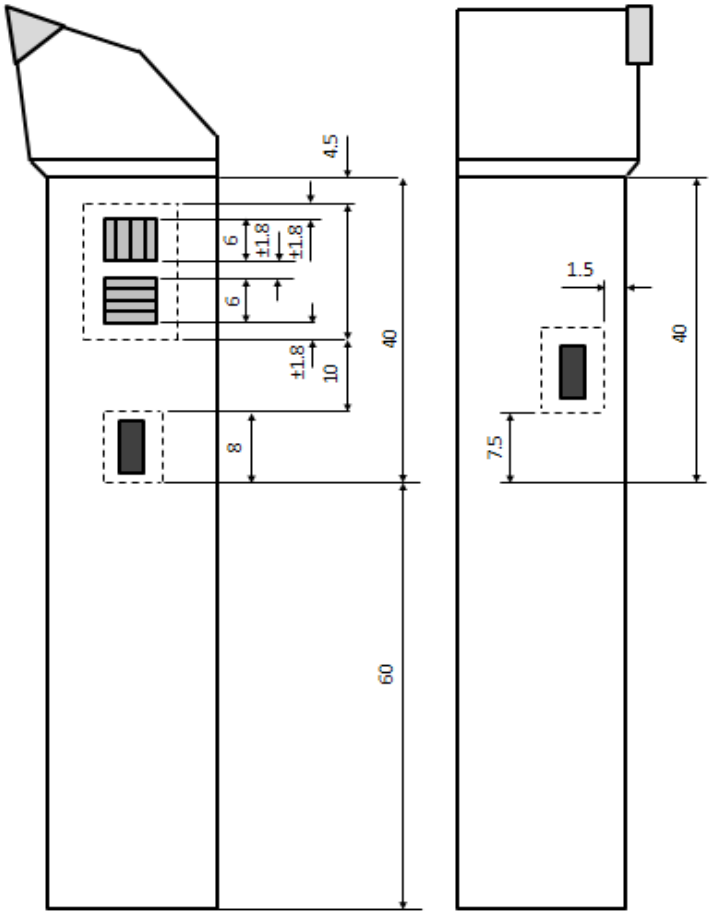

Figure B.1: Tool insert (light grey), type 1 (grey) and type 2 (dark grey) strain gauge positions on Seco PTJNR-2020-16A tool holder.

Figure B.2 shows how the strain gauges as labelled in Figure 2.2 were connected in bridge circuits. R_1 to R_8 in Figure B.2 correspond to strain gauges numbered 1 to 8 in Figure 2.2, while the R's in Figure B.2 are passive resistors or strain gauges of equal nominal value as each strain gauge when passive. The full-bridge was used to measure the thrust force onto the tool holder. The two half-bridges in Figure B.2.b and Figure B.2.c were used to measure the bending force in the direction

tangential to work piece and the bending force in feed direction respectively. V_o and V_s are the output and supply voltages respectively.

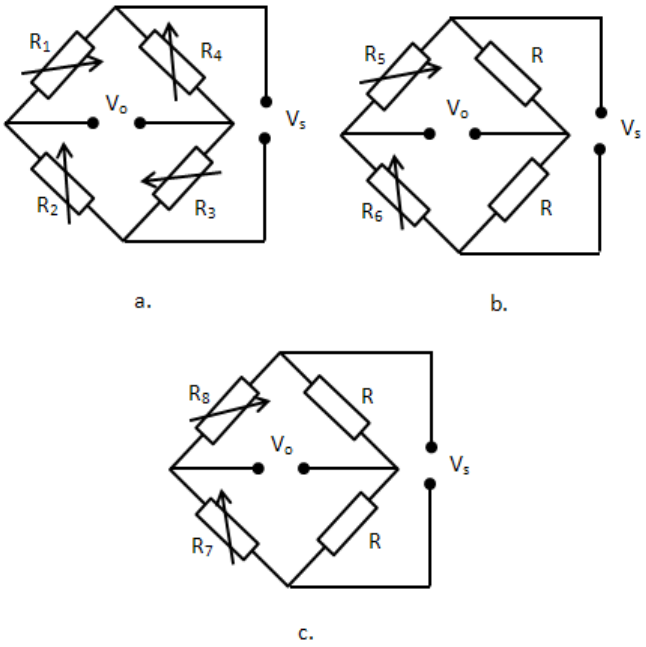

Figure B.2: Bridge circuits with strain gauges: a. full-bridge (thrust measurement) b. half-bridge (bending in direction of feed) c. half-bridge (bending in direction tangential to work piece).

For sensing of thrust with the full bridge in Figure B.2 a. the ratio of the sensed voltage V_o to V_s is

$$\frac{V_o}{V_s} = \frac{k}{4}(\varepsilon_1 - \varepsilon_2 + \varepsilon_3 - \varepsilon_4) \tag{B.1}$$

where k is the gauge factor and with the individual strain gauges sensing,

$$\left.\begin{aligned} \varepsilon_1 &= -\varepsilon_x \\ \varepsilon_2 &= \nu\varepsilon_x \\ \varepsilon_3 &= -\varepsilon_x \\ \varepsilon_4 &= \nu\varepsilon_x \end{aligned}\right\} \tag{B.2}$$

where ε_x is the strain sensed due to thrust and ν is Poisson's ratio, (B.1) becomes,

$$\varepsilon_x = -\frac{1}{2(1+\nu)}\left(\frac{4V_o}{kV_s}\right) \tag{B.3}$$

For sensing of tool holder shank bending with the half-bridge in Figure B.2 b. and c. the ratio of the sensed voltage V_o to V_s is as in (B.1) becomes,

$$\frac{V_o}{V_s} = \frac{k}{4}\left(\varepsilon_i - \varepsilon_j + \varepsilon_d - \varepsilon_d\right) \tag{B.4}$$

where k is the gauge factor, the subscript d refers to the passive half-bridge resistors/gauges and subscript $i = 5, 8$ and $j = 6, 7$ respectively for half-bridges in Figures B.2. b. and c.,

$$\left.\begin{aligned} \varepsilon_i &= \varepsilon_x \\ \varepsilon_j &= -\varepsilon_x \\ \varepsilon_d &= 0 \\ \varepsilon_d &= 0 \end{aligned}\right\} \tag{B.5}$$

and ε_x the strain sensed by the half-bridge gauges due to bending becomes

$$\varepsilon_x = \frac{1}{2}\left(\frac{4V_o}{kV_s}\right) \quad . \tag{B.6}$$

Appendix C

Quadratic regression models

Statistical models can be determined from a fully quadratic regression to represent flank wear, VB, as a function of the following cutting parameters: cutting speed, v, depth of cut, d, and feed rate, f. The resulting coefficients can be determined using the statistics toolbox of MATLAB (2003d) at a given time instant of the tool life.

The fully quadratic equation is,

$$VB = \beta_1 + \beta_2 v - \beta_3 d - \beta_4 f - \beta_5 vd - \beta_6 vf + \beta_7 df + \beta_8 v^2 - \beta_9 d^2 - \beta_{10} f^2 \qquad \text{(C.1)}$$

Table C.1: Coefficients from a fully quadratic regression of

Time instant [sec]	300	499.2	698.4	897.6	1096.8	1296
Model	1	2	3	4	5	6
β_1	0.1132	0.1548	0.1773	0.2159	0.2583	0.2886
β_2	0.3593	0.2357	0.1590	0.2908	0.3757	0.4284
β_3	-0.0299	-0.0431	-0.0791	-0.1149	-0.1002	-0.1129
β_4	0.0007	0.0074	0.0070	0.0023	0.0044	0.0069
β_5	-0.8695	-0.7143	-0.1628	0.1065	-0.0143	-0.0198
β_6	-0.0077	-0.1458	-0.1915	0.1308	0.0314	-0.2718
β_7	0.0278	0.0236	0.0775	0.1337	0.0688	0.0081
β_8	-2.0255	-0.8594	1.1769	-0.4472	-1.4491	-1.5794
β_9	-0.3058	-0.1596	0.4459	0.2108	-0.3059	-0.4243
β_{10}	-0.0343	-0.0924	-0.0830	-0.0440	-0.0898	-0.0997

Appendix D

Circuit diagrams

This appendix depicts the circuit detail of the sensing circuit in Figure D.1 including the band-pass filter in Figure D.2 and current control in Figure D.4, which was however not implemented. It also depicts circuit detail of gain (Figure D.5) and level shifters at the frontend (Figure D.6) and exit (Figure D.7) of the analogue-to-digital and digital-to-analogue converters respectively. Figure D.3 shows the circuit detail for the voltage regulator applications. The end of this appendix list the types of semiconductors as well as the values of passive components used in Tables D.1 to D.2 respectively.

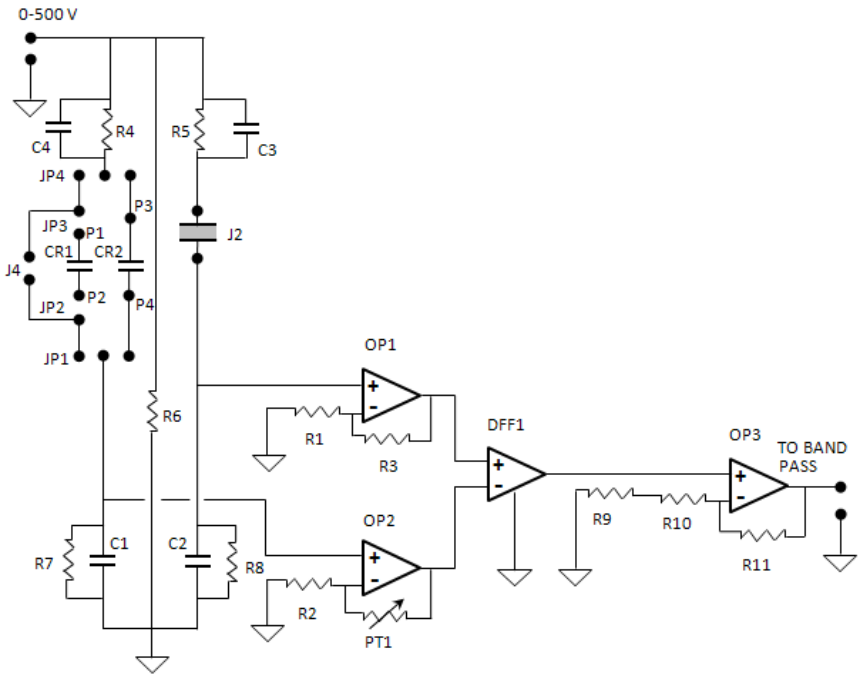

Figure D.1: Sensing circuit detail diagram

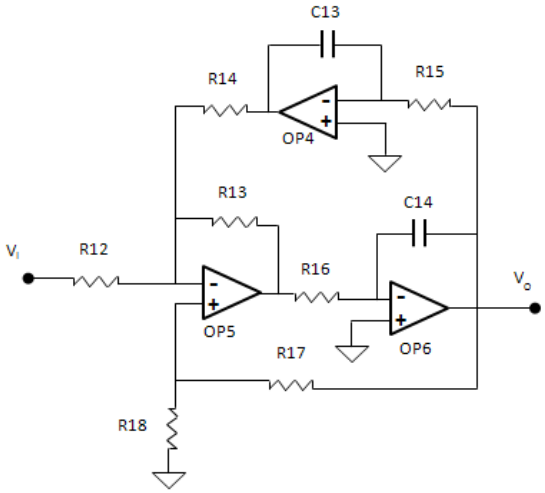

Figure D.2: Band pass circuit detail diagram according to Horowitz & Winfield (1989:277)

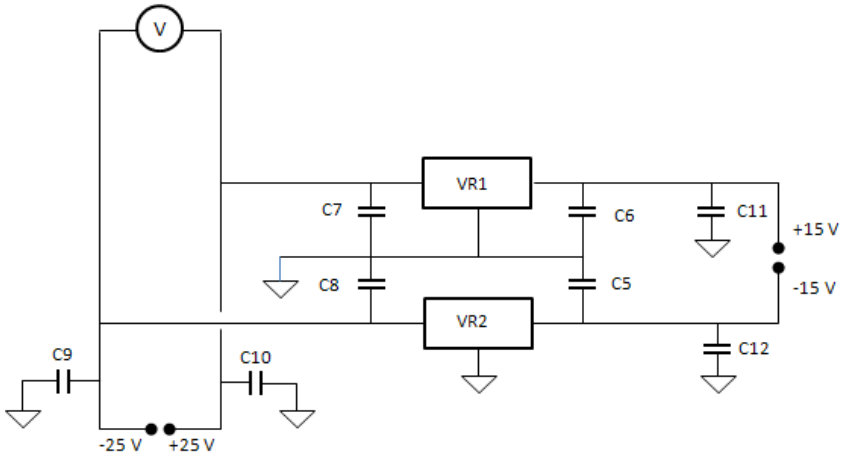

Figure D.3: Voltage regulator circuit detail diagram

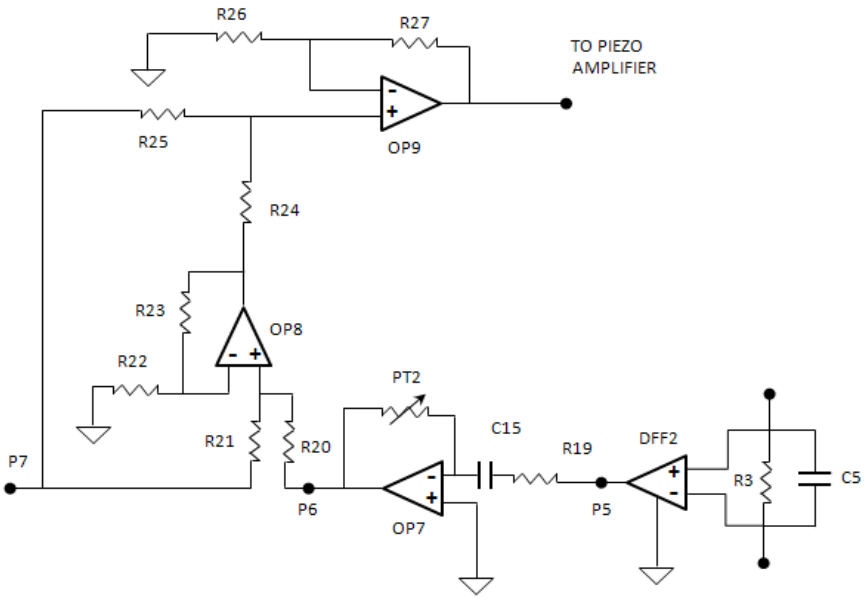

Figure D.4: Current control feedback loop circuit detail diagram: differentiator instead of phase shifter between P5 and P6 and output of gain connected at P7.

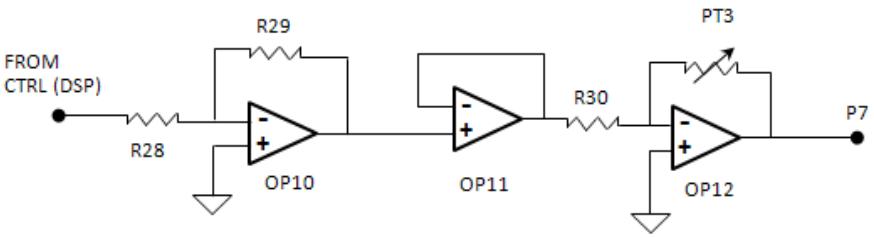

Figure D.5: Gain circuit detail diagram connected to output of DSP and at P7 to current control feedback.

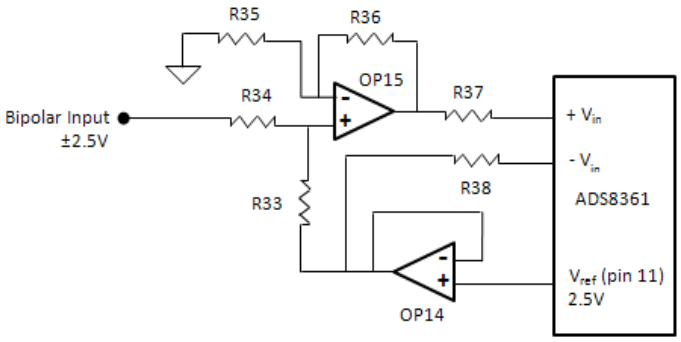

Figure D.6: Level shift circuit detail diagram according to Texas Instruments (2007:12) on input side of the ADS8361.

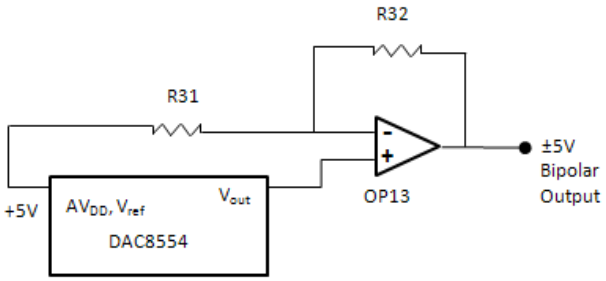

Figure D.7: Level shift circuit detail diagram according to Texas Instruments (2006a:24) on output side of the DAC8554.

Table D.1: Circuit of semiconductors used and corresponding types

Semiconductors: Differential amplifiers (DFF), Operational amplifiers (OP), Voltage regulators (VR)			
Component	Type	Component	Type
DFF1	AD629	OP9	OPA551
DFF2	AD629	OP10	OP07
OP1	OPA551	OP11	OP07
OP2	OPA551	OP12	OPA551
OP3	OPA551	OP13	OP07
OP4	OP07	OP14	OPA227
OP5	OP07	OP15	OPA227
OP6	OP07	VR1	MC78L15AC
OP7	OPA551	VR2	MC79L15AC
OP8	OPA551		

Table D.2: Circuit of passive components and corresponding values

Passive components: Capacitors (C and CR [F]), Potentiometers (PT [Ω]), Resistors (R [Ω])			
Component	Value	Component	Value
C1	2.2×10^{-6}	R10	30×10^{3}
C2	2.2×10^{-6}	R11	50×10^{3}
C3	6.0×10^{-6}	R12	316×10^{3}
C4	6.0×10^{-6}	R13	10×10^{3}
C5	0.1×10^{-6}	R14	100×10^{3}
C6	0.1×10^{-6}	R15	24.54×10^{3}
C7	0.3×10^{-6}	R16	24.54×10^{3}
C8	0.3×10^{-6}	R17	100×10^{3}
C9	0.2×10^{-6}	R18	2.87×10^{3}
C10	0.2×10^{-6}	R19	2.2×10^{3}
C11	0.1×10^{-6}	R20	10×10^{3}
C12	0.1×10^{-6}	R21	10×10^{3}
C13	1.0×10^{-9}	R22	10×10^{3}
C14	1.0×10^{-9}	R23	10×10^{3}
C15	4.0×10^{-9}	R24	12×10^{3}
CR1	107×10^{-9}	R25	12×10^{3}
CR2	173×10^{-9}	R26	12×10^{3}
PT1	20.0×10^{3}	R27	12×10^{3}
PT2	1.0×10^{3}	R28	8×10^{3}
PT3	1.0×10^{3}	R29	8×10^{3}
R1	220×10^{3}	R30	10×10^{3}
R2	220×10^{3}	R31	10×10^{3}
R3	8×10^{3}	R32	10×10^{3}
R4	2.9	R33	20×10^{3}
R5	2.9	R34	20×10^{3}
R6	220×10^{3}	R35	4×10^{3}
R7	100	R36	4×10^{3}
R8	100	R37	600
R9	30×10^{3}	R38	600

Appendix E

Sensing circuit modes of operation

In the connecting instruction for the sensing circuit during three modes of operation the convention is to look at a top view of the sensing circuit with the front panel facing to the left as in Figure E.1.

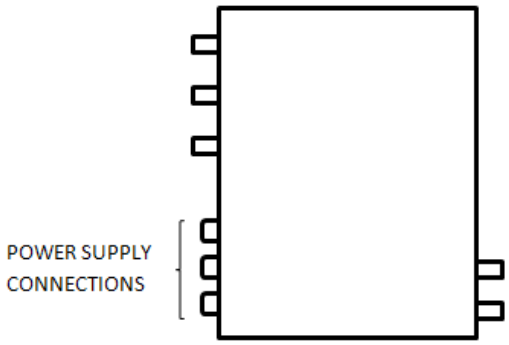

Figure E.1: Top view of sensing circuit with front panel facing left.

All three capacitors, $C_1 = 53.6\,nF$, $C_2 = 174.5\,nF$ and $C_3 = 155\,nF$ each used for a particular mode are all passive ceramic capacitors. Capacitors C_{R1} and C_{R2} refer to the correspondingly marked capacitors in Figure D.1 in Appendix D

Mode 1: Stack actuator PSt 500/10/15 is used as actuator (C_{R2} in use, C_{R1} not in use)

i. JP2 is left open
ii. JP3 is left open
iii. JP1 and JP4: 1st, 2nd and 3rd pins are all connected
iv. Connect C_1 to "Dummy J4" connector on front panel
v. Connect adjustable polystyrene capacitor in parallel with C_1 and match total capacitance across "Dummy J4" to capacitance of stack actuator PSt 500/10/15 (use LCR meter to measure capacitances)
vi. Adjust potentiometer in parallel with C_1 until dissipation factor measured across "Dummy J4" matches that of PSt 500/10/15 (use LCR meter to measure dissipation factors)

Mode 2: Stack actuator PSt 1000/16/20 is used as actuator (C_{R1} in use, C_{R2} not in use)

i. JP2 is closed
ii. JP3 is closed

iii. JP1 and JP4: only 1st and 2nd pins from left are connected

iv. Connect C_3 to "Dummy J4" connector on front panel

v. Connect adjustable polystyrene capacitor in parallel with C_3 and match total capacitance across "Dummy J4" to capacitance of stack actuator PSt 1000/16/20 (use LCR meter to measure capacitances)

vi. Adjust potentiometer in parallel with C_3 until dissipation factor measured across "Dummy J4" matches that of PSt 1000/16/20 (use LCR meter to measure dissipation factors)

Mode 3: Bridge balancing without stack actuators connected (C_{R2} in use, C_{R1} not in use)

i. JP2 is left open

ii. JP3 is left open

iii. JP1 and JP4: 2nd and 3rd pins from left are connected

iv. "Actuator J2" connector on front panel is connected to C_2

v. r.m.s. value of the sensing circuit output voltage, V_{sens} (see Figures 4.1 and 4.2), is measured with a multimeter, while potentiometer in the left half of the image in Figure H.4 is adjusted to minimize measured value.

Appendix F

Data converter pin settings

The tables of this appendix list the settings for the pins on the ADS8361, the DAC8554 and the 5-6K Interface Board in Table F.1 to Table F.3 respectively. The pins embraced by the brackets are connected. Pins that are not embraced by brackets are left open.

Table F.1: Settings for analogue-to-digital converter pin sets in Texas Instruments (2011).

Settings for Pin Sets: ADS8361– Top to Bottom (T to B), Left to Right (L to R)	
Pin Set	Setting
W1 (L to R)	[. .]
W2 (T to B)	[. .].
W3 (L to R)	[. .].
W4 (L to R)	[.].
W5 (L to R)	[.].
J5 (L to R)	[.]. [. .] [.]. . .

Table F.2: Settings for digital-to-analogue converter pin sets in Texas Instruments (2006b).

Settings for Pin Sets: DAC8554 – Top to Bottom (T to B), Left to Right (L to R)	
Pin Set	Setting
JMP1 (T to B)	[. .]
JMP2 (T to B)	[. .]
JMP3 (T to B)	[. .]
JMP4 (T to B)	[. .]
JMP5 (L to R)	.[.]
JMP6 (T to B)	.[.]
JMP7 (L to R)	[. .].
JMP8 (T to B)	.[. .]
JMP9 (L to R)	[. .].
JMP10 (L to R)	[. .].
JMP11 , OUT A (L to R)	[. .].
JMP12 , OUT B (L to R)	[. .].
JMP13 , OUT C (L to R)	[. .].
JMP14 , OUT D (L to R)	[. .].
JMP15 (L to R)	[. .].
JMP16 (L to R)	.[. .]

Table F.3: Settings for pin sets of Interface Board 5-6K in Texas Instruments (2009).

Settings for Pin Sets: Interface Board 5-6K – Top to Bottom (T to B), Left to Right (L to R)	
Pin Set	Setting
W1 (L to R)	[. .]
W2 (L to R)	.[. .]
W3 (L to R)	.[. .]
W4 (L to R)	.[. .]
W5 (L to R)	.[. .]
W6 (L to R)	[. .].
W7 (L to R)	[. .].
W8 (L to R)	[. .].
W9 (L to R)	[. .].
W10 (L to R)	[. .].
W11 (L to R)	[. .].
W12 (L to R)	.[. .]
W13 (L to R)	.[. .]

Appendix G

Controlled current drive of piezo actuator

In this section the option of an inner control loop is described with feedback signal, V_I. The purpose of the feedback via a phase shift in Figure G.1 is to accomplish tracking of input voltage V_{i1} by the current in the piezo actuator shown as I_p in Figure 4.2. The inner control loop is an option and measure to linearize the hysteresis exhibited by the piezoelectric actuator.

This configuration was suggested by Bayerle (2015). Instead of directly sensing the current in the piezoelectric actuator, I_p, an indication of its magnitude is obtained via the voltage difference over the shunt in Figure 4.2, ΔV_{shunt} . An indication of the phase of I_p , is obtained not from measurement but from a-priori knowledge that the phase of current in the piezo element is 90° relative to the phase of ΔV_{shunt}. The phase shift block in Figure G.1 indicates that if the phase of ΔV_{shunt} relative to V_{i1} is φ° then a $-(\varphi - 90)°$ shift of phase would be needed on ΔV_{shunt} . This is needed to ascertain that the phase of the feedback signal is that of the current in the piezo actuator. In Figure G.1 the signal V_I in Volt is equal to I_p in Ampere if the magnitude of the open loop path G_{ip} is set to

$$\left|G_{ip}\right| = \frac{|I_p|}{|V_{i1}|} \approx 1 \tag{G.1}$$

by selection of R_{shunt} with

$$\left|I_p\right| = \frac{|\Delta V_{shunt}|}{R_{shunt}} \ . \tag{G.2}$$

If the inner loop feedback system in Figure G.1 is denoted as T_{ip}, then it can be derived as

$$T_{ip} = \frac{2G_{ip}}{1+G_{ip}} \tag{G.3}$$

with V_{i1} as input and V_I as output.

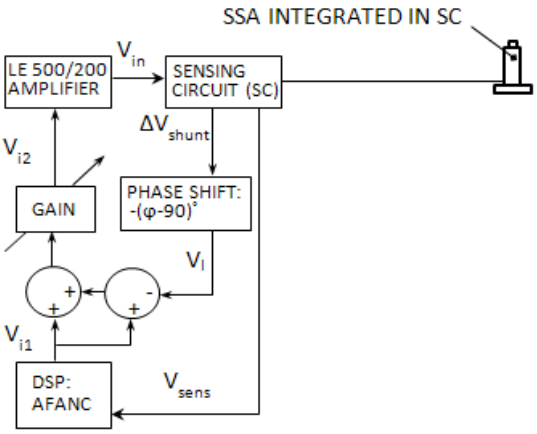

Figure G.1: Current control system: Inner current control loop

Appendix H

Photos of set-up for active tool vibration control

Figure H.1: Set-up: Shaker with self-sensing actuator (copper casing) and representative tool post and holder left and instrumentation bench right.

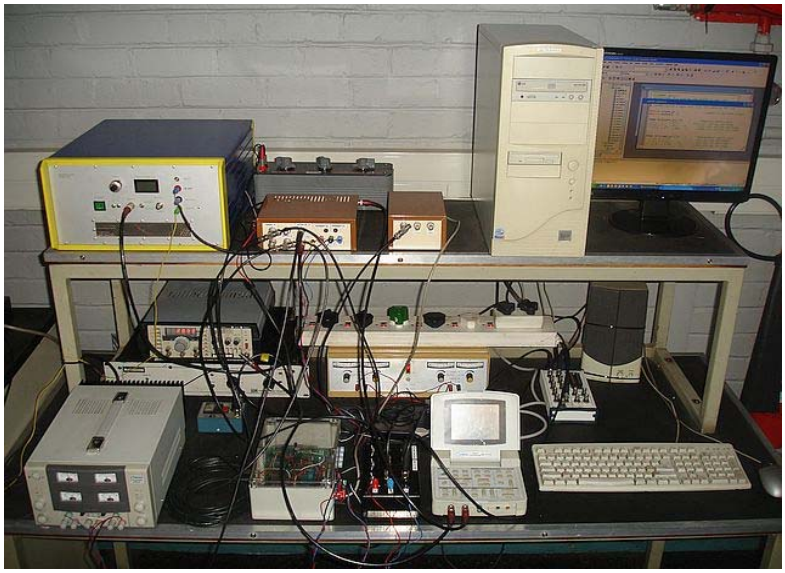

Figure H.2.: Instrumentation bench: Lower surface front left to right: ± 15 V Dual power supply, DSP, 8 kHz anti-alias filter, digital oscilloscope. Lower surface middle: Piezotronics power unit (blue). Lower surface back left to right: Function generator (top left) shaker drive amplifier (bottom left), ± 25 V dual power supply, connector block. Top surface left to right: Piezo drive amplifier, sensing circuit (front), adjustable polystyrene capacitor (back), reference capacitors.

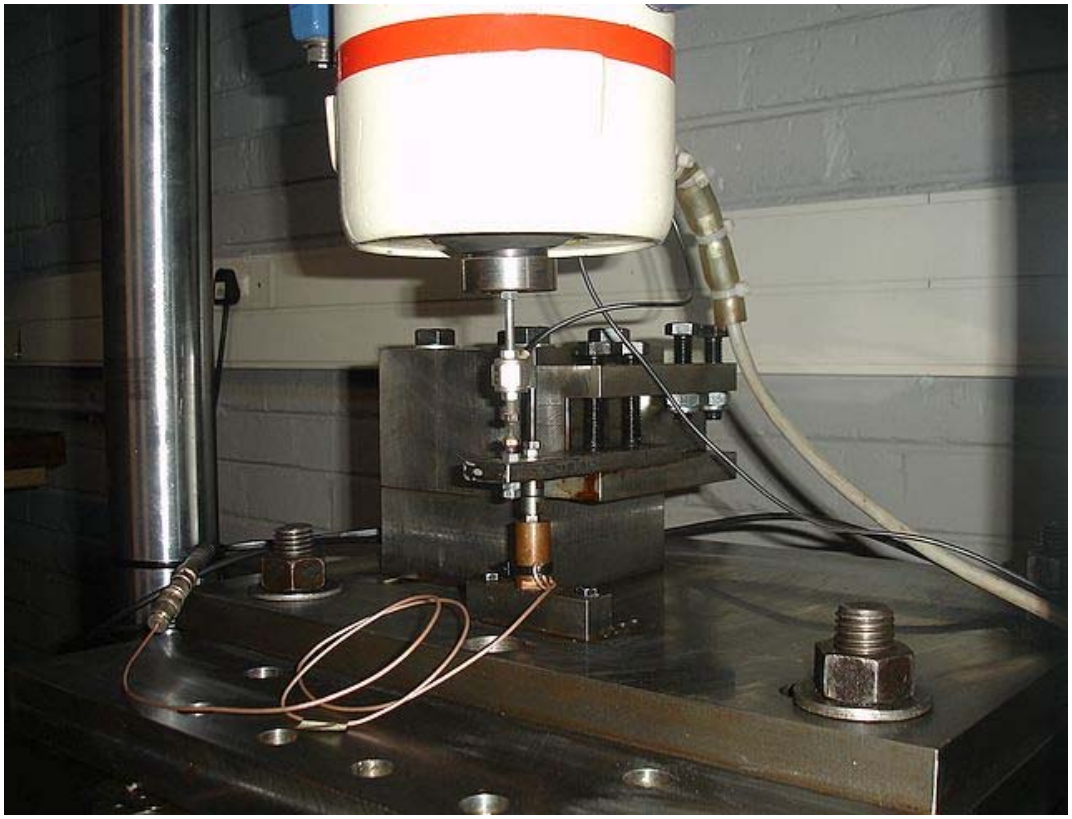

Figure H.3: Connection of shaker via load cell and stinger to representative tool holder supported by self-sensing actuator and clamped in representative tool post

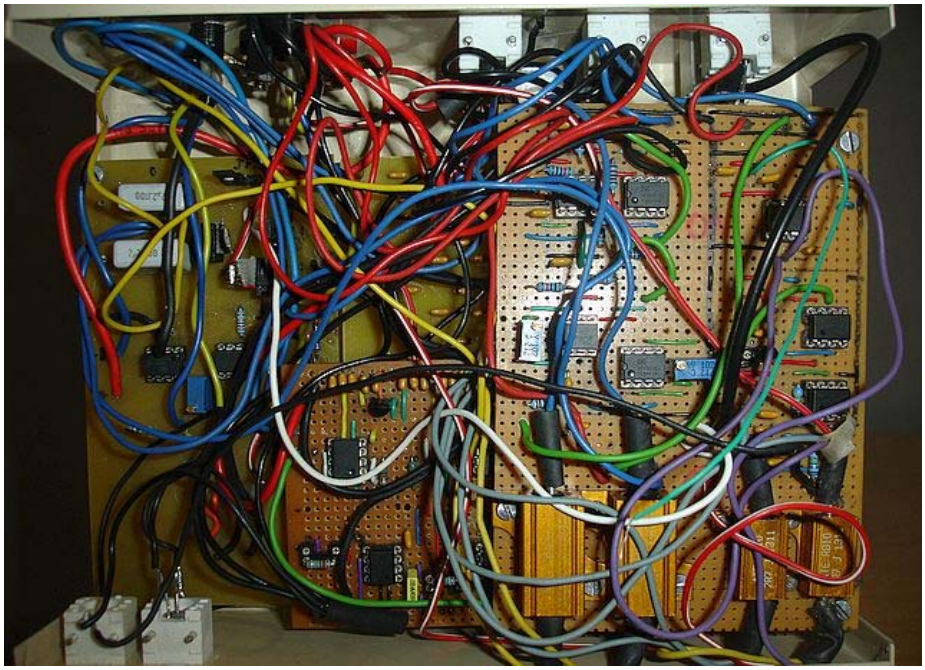

Figure H.4: Sensing circuit: Middle right half of image: potentiometer for amplifier input gain adjustment. Bottom right to left: Four high-power resistors: two shunt and two 100 Ω resistors

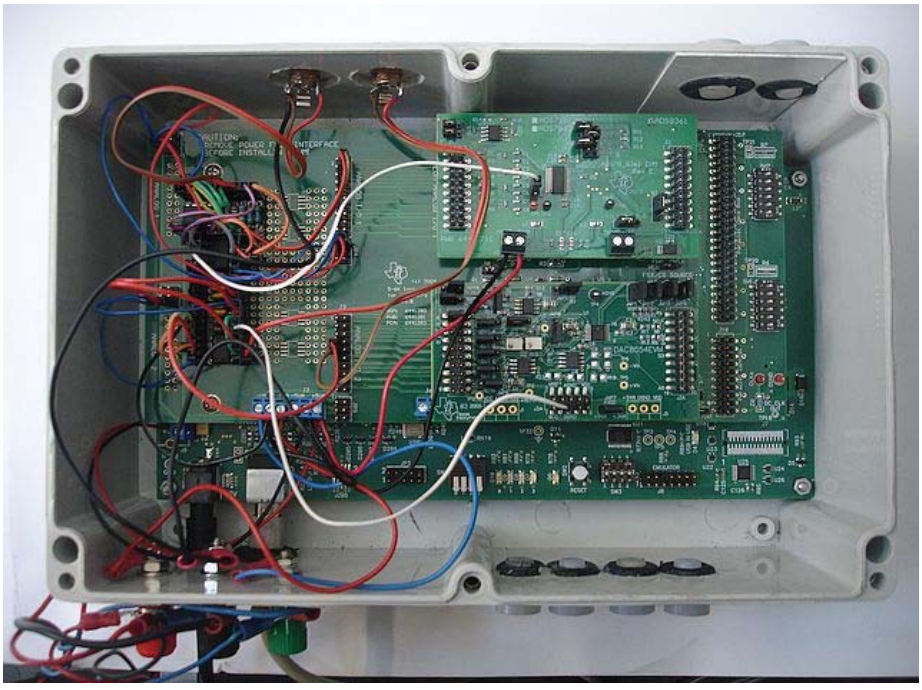

Figure H.5: TMS320C6713 DSP (lower level), level shifter circuits (left), analog-to-digital converter, ADS 8361 (upper level top right), digital-to-analog converter, DAC 8554 (upper level bottom right).